KAUNAS UNIVERSITY OF TECHNOLOGY

ERIKA ELIJOŠIUTĖ

SPECTROSCOPIC STUDIES AND THEORETICAL MODELING OF IRON(III) AND MERCURY(II) THIOCYANATE COMPLEXES

Dissertation
Physical Sciences, Chemistry (03P)

2014, Kaunas

KAUNO TECHNOLOGIJOS UNIVERSITETAS

ERIKA ELIJOŠIUTĖ

GELEŽIES(III) IR GYVSIDABRIO(II) TIOCIANATŲ SPEKTROSKOPINIAI TYRIMAI IR TEORINIS MODELIAVIMAS

Daktaro disertacija
Fiziniai mokslai, Chemija (03P)

2014, Kaunas

Mokslinis vadovas:

Doc. dr. Dalia Jankūnaitė (Kauno technologijos universitetas, fiziniai mokslai, chemija, 03P).

Moksliniai konsultantai:

Dr. Olegas Eicher-Lorka (Fizinių ir technologijos mokslų centras, fiziniai mokslai, chemija, 03P);

Doc. dr. Egidijus Griškonis (Kauno technologijos universitetas, technologijos mokslai, chemijos inžinerija, 05T).

CONTENTS

LIST OF TABLES

LIST OF FIGURES

9

LIST OF ABBREVIATIONS

B3LYP – Becke three-parameter hybrid functional combined with Lee–Yang–Parr correlation functional

CAM-B3LYP – Coulomb-attenuated B3LYP functional

CCD – charge-coupled device

CN – coordination number

CT – charge transfer

DFT – density-functional theory

DMF – dimethylformamide

DMSO – dimethylsulphoxide

ECP – effective core potential

ES – excited state

FTIR – Fourier transform infrared

FT-Raman – Fourier transform Raman

GS – ground state

HOMO – highest occupied molecular orbital

HSAB – hard soft acid base theory

IEF – integral equation formalism

IEFPCM – integral equation formalism polarizable continuum model

IR – infrared

LLCT – ligand-to-ligand charge transfer

LMCT – ligand-to-metal charge transfer

LUMO – lowest occupied molecular orbital

MLCT – metal-to-ligand charge transfer

MC – metal-centered

MOCN – metal-organic coordination network

MOF – metal-organic framework

MO – molecular orbital

NIR – near-infrared

NIST – National Institute of Standards and Technology

NLO – nonlinear optics

NMR – nuclear magnetic resonance

NTO – natural transition orbitals

PBEPBE – the gradient-corrected correlation functional of Perdew, Burke and Ernzerhof

PBE1PBE – hybrid functional of Perdew, Burke and Ernzerhof

PCM – polarizable continuum model

PED – potential energy distribution

SERS – surface-enhanced Raman spectroscopy

SOD – superoxide dismutation

TD-DFT – time-dependent density-functional theory

UV – ultraviolet

UV-Vis – ultraviolet-visible

XRD – X-ray diffraction

a.u. – arbitrary units

1. INTRODUCTION

In the current studies thiocyanate-containing metal complexes are considered to be the most investigated systems because of their diverse structures and applications in the field of materials science [1–6]. In agreement with the hard soft acid base (HSAB) theory, the pseudohalide thiocyanate (SCN^-) ion is a versatile ligand that shows a propensity to coordinate either to hard or soft transition metal ions by the nitrogen or/and the sulfur donor-atom, respectively [7–10]. Various binding modes of the SCN^- ligand are expected to afford a number of homo- and heterometallic discrete one-, two- and three-dimensional structural assemblies with specific structural features and optical and magnetic properties. Simultaneous presence of two different metal centers can potentially give rise to useful physico-chemical properties and lead to attractive novel topologies and intriguing frameworks [11, 12].

The complexes of mercury(II) and iron(III) ions are of interest since they are involved in many analytical processes. Thiocyanate-based mercury(II) and iron(III) complexes are widely found in the aqueous solutions employed for the determination of chloride ions in clinical and industrial laboratories [13] or obtained during mercury determination procedures in laboratories using titrimetric analysis [14]. Moreover, due to characteristic features of the iron(III)-thiocyanate complex, it is applicable to a range of quantitative analysis of lipid containing materials which are important for biomedicine (determination of pharmaceuticals), food and other industry (e.g. solvent extraction of gold from thiocyanate solutions) [15–19].

Dealing with the intrinsic view of certain molecule in the solution, it is well known that the changes of spectroscopic and structure properties are the issues of the coordination chemistry. The coordination mode of SCN^- ligand is influenced by the nature of the central atom, steric factors, symbiosis of 'hard and soft' ligands in the coordination sphere [10, 20], solvent effects [21–23], metal charge, and other coordinated ligands, especially when metal ion belongs to the group of transition metal [10]. Most of transition metal ions form complex ions with water molecules which behave as a ligand set [24]. The knowledge of the number of water molecules occupying the first coordination sphere of a metal ion is of paramount importance in understanding the nature and reactivity of metal complexes in solution [25]. Hereby, the powerful analytical tool commonly used to characterize transition metal complexes is vibrational spectroscopy. This technique provides an insight on frequency variations, leading to the detailed information on the structure of complexes [26, 27]. However, the interpretation of the vibrational spectrum is not straightforward, and in general cannot be accomplished without the high level of computational modeling. The employment of the modern density functional theory (DFT) methods for the molecular systems has revolutionized computational chemistry, especially for the transition metals [28, 29]. Moreover, the time-dependent density-functional theory (TD-DFT) theory emerges as one of the most practical tools that can be used to predict the electronic properties of transition metal complexes [30].

12

With all these data in mind and due to missing studies on iron(III) and mercury(II) thiocyanate systems, the detailed molecular level knowledge on the structure, electronic properties and vibrational characteristics of $[Fe(NCS)_n]^{3-n}$ (where n = 1–6) and $[Hg(SCN)_n]^{2-n}$ (where n = 2–4) complexes are required. In this work the thorough experimental analysis of vibrational and electronic spectra of all $[Fe(NCS)_n]^{3-n}$ and $[Hg(SCN)_n]^{2-n}$ complexes in the acidic aqueous media, supplemented by the extensive DFT calculations on the particular complexes, were carried out. The calculations are based on the evaluation of effects of different solvation models and different arrangement of SO_4^{2-} *vs.* NCS⁻ ligand in the case of iron(III) monoisothiocyanate complex.

The aim of this research was to improve knowledge on the molecular structure and interactions of iron(III) and/or mercury(II) ions with the thiocyanate ion in the aqueous solution at the pH ~ 2 ± 0.1 and to select the most appropriate method and functional for geometry optimizations, electronic and vibrational spectra calculations.

The main tasks of this research were as follows:
1. to characterize and make assignments of the iron(III) monoisothiocyanate in aqueous acidic solution using Raman spectroscopy, isotopic substitution, and quantum chemistry calculations;
2. to evaluate the influence of different solvation models and different position of SO_4^{2-} ligand *vs.* NCS⁻ ligand upon iron(III) monoisothiocyanate's vibrational frequencies and electronic spectra using DFT calculations;
3. to perform excited state analysis of iron(III) monoisothiocyanate using DFT calculations and to establish the influence of different calculation methods and functionals used on the geometry optimizations and electronic spectra calculations, respectively;
4. to characterize and make assignments of the mercury(II) thiocyanates in aqueous acidic solution using Raman spectroscopy, isotopic substitution and quantum chemistry calculations;
5. to determine the effect of different solvation models on the molecular structure, vibrational and electronic spectra of mercury(II) thiocyanates by means of theoretical modeling;
6. to investigate peculiarities of simultaneous complex formation in the acidic aqueous media in the presence of iron(III), mercury(II), and thiocyanate ions.

The novelty and significance of the work. A combined experimental and theoretical study on the molecular structure, vibrational and electronic spectra of $[Fe(NCS)]^{2+}$ and $[Hg(SCN)_n]^{2-n}$ (where n = 2–4) complexes in the aqueous solution at the pH ~ 2 ± 0.1 have been performed. Molecular modeling of the complexes was accomplished by the density functional theory (DFT) method. The influence of different solvation models upon geometry, vibrational frequencies and UV spectrum

of titled complexes have been estimated. In case of iron(III) monoisothiocyanate the effect of different position of SO_4^{2-} ligand *vs*. NCS^- ligand for structure, vibrational and electronic properties have been evaluated. The effect of H_2O/D_2O isotopic substitution on the experimental and calculated Raman spectra of iron(III) isothiocyanates and mercury(II) thiocyanates has been examined. It has been demonstrated that at the pH value ~ 2, the NCS^-, SO_4^{2-} ions and H_2O molecules are found as ligands in the first coordination sphere of the six-coordinated Fe(III) ion as well as four-coordinated Hg(II) complexes with SCN^- and (or) H_2O ligands were formed. Detailed vibrational assignments for the investigated metal-thiocyanates were proposed here for the first time. It was found that the νHg–S vibrational mode of the all analyzed mercury complexes and νC≡N mode of $[Hg(SCN)_3H_2O]^-$ complex has the double-peak character. Based on the excited state analysis of iron(III) monoisothiocyanate, the vast majority of electronic transitions were characterized as ligand-to-metal (LMCT) charge transfers.

2. LITERATURE REVIEW

2.1. Chemistry of transition metals

The chemical elements in the periodic table are arranged together in the blocks according to their outer electronic configurations. The elements with a half-filled or fully-filled outer s orbital or p orbital comprise the s-block or p-block elements. Together the s- and p-block elements comprise the **main group** elements. Between these two blocks of elements are two further blocks (that is between the groups 3 and 12 in the periodic table) containing **transition elements** (Table 2.1). Strictly speaking, the term "transition element" applies that elements have at most two electrons in the outermost s orbital, and incompletely filled d and f subshell next to outermost orbital. These elements, which form a group of elements ten-wide and four-deep in the Periodic Table, are associated with filling the d orbitals and called as d-block elements [31–34]. A transition element may be defined as element which possesses partially filled d-orbitals in its penultimate shell. This definition is used to recognize a transition element merely by looking at its electronic configuration. However, this definition excludes zinc, cadmium and mercury from the transition elements as they do not have a partially filled d-orbital. Even so, they are also considered as transition elements, because of the similar properties to transition elements [31]. The d-block elements are generally referred to as the **transition metals**. The elements from scandium to copper are often refered to as the first transition series or first-row transition metals, those from yttrium to silver form the second transition series or second-row and those from lanthanum to gold form the third series or row within the d-block. The f-block elements are commonly known as **inner transition elements** which appear, firstly after lanthanum and secondly after actinium, in the Periodic Table. The elements from cerium to lutetium are known as the lanthanides and, because of its chemical similarity to these elements, lanthanum is usually included with them. The second series of f-block elements, from thorium to lawrencium, is known as the actinide series and again it is usual to consider actinium together with this series [32–35].

Table 2.1. The Periodic Table emphasizing the transition series d-block and inner transition series f-block elements [35]

USA[b]	IA	IIA	IIIB	IVB	VB	VIB	VIIB		VIIIB		IB	IIB	IIIA	IVA	VA	VIA	VIIA	VIIIA
EU[c]	IA	IIA	IIIA	IVA	VA	VIA	VIIA		VIII		IB	IIB	IIIB	IVB	VB	VIB	VIIB	0
IUPAC[d]	1	2	3	4	5	6	7	8	9	10	11	12	13	14	15	16	17	18
	H	He																
	Li	Be											B	C	N	O	F	Ne
	Na	Mg											Al	Si	P	S	Cl	Ar
4s 3d	K	Ca	Sc	Ti	V	Cr	Mn	Fe	Co	Ni	Cu	Zn	Ga	Ge	As	Se	Br	Kr
4p			21	22	23	24	25	26	27	28	29	30						
5s 4d	Rb	Sr	Y	Zr	Nb	Mo	Tc	Ru	Rh	Pd	Ag	Cd	In	Sn	Sb	Te	I	Xe
5p			39	40	41	42	43	44	45	46	47	48						
6s 5d 4f	Cs	Ba	La	Hf	Ta	W	Re	Os	Ir	Pt	Au	Hg	Tl	Pb	Bi	Po	As	Rn
6p			57	72	73	74	75	76	77	78	79	80						
7s 6d 5f	Fr	Ra	Ac	Rf	Db	Sg	Bh	Hs	Mt									
7p			89	104	105	106	107	108	109	110	111	112						
				(Unq)	(Unp)	(Unh)	(Uns)	(Uno)	(Une)	(Uun)	(Uuu)	(Uub)						

Ce	Pr	Nd	Pm	Sm	Eu	Gd	Tb	Dy	Ho	Er	Tm	Yb	Lu
58	59	60	61	62	63	64	65	66	67	68	69	70	71
Th	Pa	U	Np	Pu	Am	Cm	Bk	Cf	Es	Fm	Md	No	Lr
90	91	92	93	94	95	96	97	98	99	100	101	102	103

[a] Atomic numbers Z are shown beneath the element symbol for the d- and f-block elements; International Union of Pure and Applied Chemistry (IUPAC) symbols are shown in parantheses for the fourth row of the d-block
[b] This numbering system for groups has traditionally been used in the USA
[c] This numbering system for groups has traditionally been used in Europe
[d] This numbering system for groups has been aproved by IUPAC and is one used throughout this text [35]

The certain features of complexes (formed from metal ions having incomplete filling of the d and f orbitals) that are not observed in other complexes, are exploited in a remarkable variety of applications [35, 36]. Some metals are used in very large quantities, particularly iron in structural materials, while others are used in only small quantities for specialized applications such as the synthesis of fine chemicals [35].

The first and most obvious feature is the great variety of colors observed in these complexes – even in the simplest complex ions, the hydrated ones [36]. The colours associated with some transition metal compounds make them useful as pigments. In some cases it is the absence of colour which is important. In other cases it is the ability of an excited metal ion to emit light of a particular frequency which is useful. The lanthanide elements in particular show strong luminescence of the type needed in the cathode ray tubes of colour television sets [35]. Additionally, the recent surge of interest is the use of d-block complexes as sensitisers for lanthanide-based near-infrared (NIR) region luminescence [37].

A second unique feature is the magnetic properties of transition metal ions – they may have unpaired electrons, which result in the magnetic property called paramagnetism [36]. A common place example is provided by magnetic recording media such as hard discs and magnetic recording tapes, the coating of which contains metal oxides. Small high-intensity permanent magnets are important in the construction of compact powerful electric motors, such as those used to power

windows in cars. A quite different exploitation of the magnetic properties of metal ions is provided by the use of lanthanide ions [35].

A third important feature is the large number of possible oxidation states which (in contrast with elements in the p-block) may differ by only one electron therefore zero or negative oxidation states are possible.

A fourth feature is that the d-block metal ions may bond well with certain types of ligands such as carbonyl ligand, that very seldom bond to p-block elements [36]. The special chemical reactivity of the transition metals can be exploited in a variety of catalytic processes. As well as having electrical conductivity, the transition elements can be used in the production of electrical energy through their chemical reactivity. Perhaps the most immediately familiar example is the 'dry cell' battery. Any of a number of chemical reactions may be exploited in this context. As a consequence, manganese, nickel, zinc, silver, cadmium or mercury may be found in dry cells [35]. Some d- or f-block elements are also applicable in organic synthesis [35, 38, 39]. Lastly, transition elements also tend to be used in diagnostic medicine [35].

2.2. Thiocyanate-based transition metal systems

Design and synthesis of transition metal complexes with structural diversities as far as dimensionality and topology of the species have become a fascinating area of contemporary research in the field of supramolecular chemistry and crystal engineering [40–42]. Pseudohalides, especially thiocyanate ions, have attracted much attention because of their versatile coordination binding modes, which results in the formation of complexes with various dimensionalities. Scientists are interested in the possible applications of hybrid inorganic-organic materials in various fields such as catalysis [40, 42, 43], synthesis of light emitting materials [42], and photochemical sensing [44], biochemistry and pharmacology [41, 45–47], molecular magnetism [43, 48–50].

2.2.1. Coordination chemistry of the thiocyanate group

The chalcogenocyanate ion, SCN^-, is a linear triatomic anion, usually classified as pseudohalide. SCN^- is a highly versatile ambidentate ligand with two donor atoms. It can coordinate through either the nitrogen or the sulphur atom, or both, giving rise to linkage isomers or polymers [45, 51, 52]. Hence, linkage isomerism has been one of the most interesting and significant phenomena observed in coordination chemistry [44]. The first example of thiocyanate linkage isomers was reported in 1961 [53]. The resonance structures of SCN^- ligand are:

$$^-S–C\equiv N \text{ (A)} \leftrightarrow S=C=N^- \text{ (B)} \leftrightarrow {}^+S\equiv C–N^{2-} \text{ (C)}$$

The relative importance of the resonance structures follows the trend A > B >> C [51]. According to Kawaguchi [54], the π-electron structure of the thiocyanate ion may be represented as shown in Figure 2.1. The numbers written over the atoms

shows electron densities on the atoms, and the numbers written under the bonds are the π-bond orders.

$$-0.4826 \qquad +0.1934 \qquad -0.7108$$

$$N \equiv\!\!=\!\!=\!\!= C \text{------} S$$

$$1.8243 \qquad\qquad 0.7964$$
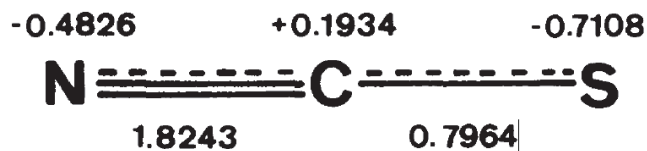
Figure 2.1. π-electron structure of the thiocyanate ion [54]

The difference in the charge densities on the N and S atoms is not very large. This may be the reason why the thiocyanate anion exhibits a variety of coordination modes [53] as will be discussed in more detailed in the following 2.2.2 section. The coordination modes of the SCN^- ligand can be classified as terminal or bridging (Fig. 2.2).

Type	Terminal	Type	Bridging
Ia	S-coordination $S-C\equiv N$ $|$ M (thiocyanate)	IIa IIb IIc	$M-SCN-M$ $M\diagdown{}_{SCN}$ $M\diagup$ $SCN\diagup{}^{M}$ $\diagdown_{M}$
Ib	N-coordination $S-C\equiv N-M$ (isothiocyanate)	IIIa IIIb IIIc IIId	$M\diagdown{}_{SCN-M}$ $M\diagup$ $M-SCN\diagup{}^{M}$ $\diagdown_{M}$ $M\diagdown$ $M-SCN$ $M\diagup$ $SCN-M$ with three M
		IVa IVb IVc	$M\diagdown{}_{SCN}\diagup{}^{M}$ $M\diagup{}\diagdown{}_{M}$ $M\diagdown$ $M-SCN-M$ $M\diagup$ $M-SCN$ with three M
		Va Vb	$M\diagdown$ $M-SCN\diagup{}^{M}$ $M\diagup{}\diagdown{}_{M}$ $M\diagdown{}_{SCN}$ with three M
		VI	$M\diagdown$ $M-SCN$ with M's $M\diagup$

Figure 2.2. Coordination modes of an ambidentate ligand [51]

19

2.2.1.1. Terminal modes

There are two types of terminal coordination of SCN⁻ ligand: S-coordinated SCN⁻ (M–SCN) which is termed thiocyanate (type Ia, Figure 2.2) and N-coordinated SCN⁻ (M–NCS) which is called isothiocyanate (type Ib, Figure 2.2). Metal thiocyanates, M–S–C≡N, are usually bent with M–S–C angle of 100° (in the range of 80–110°) whereas in metal isothiocyanates, M–N≡C–S, the M–N–C angles are variable, though commonly with a M–N–C angle of around 150° (in the range of 110–180°) [49, 51, 55]. Thiocyanate typically bonds terminally via the nitrogen with the first row transition metals and M–S bonds are formed with the metals of second and third row [45, 49, 56].

2.2.1.2. Bridging modes

According to the three possible resonance structures of SCN⁻ discussed above, there are theoretically thirteen multidentate bridging modes, ranging from bi- to hexadentate, of the ambidentate SCN⁻ ligand, as is shown in Figure 2.2. Here the highly unfavorable quadruple bridging modes of four atoms by either the S or the N atom are eliminated. Moreover, not all of these bridging modes have been observed in scientific researches. The most commonly observed bridging modes are the bidentate and the tridentate coordinations presented in the Figure 2.2 as II a–c and III a, b, respectively. Combinations of these coordination modes give rise to a variety of interesting metal thiocyanate structures with different properties [51]. The coordination modes such as IIa, IIIa, IIIb and IIb, IIc, IIIc, IIId, and etc. are called end-to-end and end-on fashion, respectively [45].

2.2.2. Metal thiocyanate coordination

The modes of metal thiocyanate coordination are best understood in terms of the HSAB theory. In agreement with the HSAB concept, the SCN⁻ ion coordinates to hard acids (i.e. Mn^{2+}, Co^{2+}, Ni^{2+}, Mg^{2+}, Fe^{3+}, Na^+) through nitrogen atom, which is described as a hard base. The uncoordinated sulphur atom is involved in hydrogen bonds and sometimes involved in S-S interactions. If the transition metal center is soft acid (i.e. Cd^{2+}, Cu^+, Hg^{2+}), then SCN⁻ ligand binds to central ion through sulphur atom which is described as a soft base [7–9, 51, 53, 57]. The examples of hard and soft metal ions and ligands (Lewis acid/base), respectively, are given in the Table 2.2.

Table 2.2. Classification of ions and ligands under hard/soft formalism [58, 59]

Ligands or bases	
Hard	H_2O, ROH, R_2O, OH^-, OR^-, NO_3^-, RCO_2^-, SO_4^{2-}, CO_3^{2-}, $C_2O_4^{2-}$, PO_4^{2-} (donors through O) NH_3, NR_3, NHR_2, NH_2R, Cl^-, F^-
Soft	R_2S, RSH, RS^-, SCN^-, $S_2O_3^{2-}$, (S donors) R_3P, R_3As, I^-, CN^-, H^-, R^-, C_2H_4
Borderline	$C_6H_5NH_2$, C_5H_5N, Br^-, N_3^-, SO_3^{2-}, NO_2^-
Metal ions or acids	*(charges are formal only)*
Hard	Mn^{2+}, Cr^{3+}, Fe^{3+}, Co^{3+}, Ti^{4+}, VO_2^+, VO^{2+}, Zr^{4+}, MoO^{3+}, H^+, all s element ions, M^{3+} for M=Al, Ga, In, Sc, Y, Ln
Soft	Cu^+, Cd^{2+}, Ag^+, Au^+, Hg_2^{2+}, Hg^{2+}, Pd^{2+}, $Pt^{2+,}$ Pt^{4+}, Ti^+, Ti^{3+}
Borderline	Fe^{2+}, Co^{2+}, Ni^{2+}, Cu^{2+}, Zn^{2+}, Ru^{2+}, Os^{2+}, Rh^{3+}, Ir^{3+}, Sn^{2+}, Pb^{2+}, Sb^{3+}, Bi^{3+}

Here it should be noted that, the N-bonded thiocyanate ligand is harder and is most usually found in thiocyanate complexes of the first row transition metals [59]. However, sometimes HSAB concept has exceptions. As an example is soft acid Cd^{2+} ion, which tends to link the SCN^- ligand exhibiting both S and N bonding modes as well as a variety of coordination numbers [51, 60–62]. Generally, it is agreed that interactions between hard acids and hard bases are based on ionic bonds, whereas those between soft acids and soft bases involve covalent bonds [57]. Furthermore, it has already been identified that for the bonding properties of thiocyanate ligand the whole system of three atoms is responsible. This feature is not characteristic in the cases of other ligands containing S- and N-donor atoms [63]. Speaking about stabilities of the metal thiocyanate complexes, the same tendency remains. Soft ligands form stable complexes with soft metal ions, as well as hard ligand–hard ion complexes are also stable. Mixtures of hard ion–soft ligand or soft ion–hard ligand are less stable [59]. When considering reactions in aqueous solution, it should be taken in to account that the solvent itself is both a powerful Lewis acid and Lewis base. Water molecules mask many effects in solution and the mistakes in interpretion of the thermodynamics of complex in aqueous solution only in terms of factors related to M–L bond formation could occur [58].

Since the ambidentate thiocyanate ligand displays a great variety of its coordination modes, the coordination numbers (CN) can range from 1 up to 12. The most common coordination numbers for transition metal thiocyanate complexes are 6 and 4, while coordination numbers such as 5, 3, 2 (low coordination) or 7, 8, 9, 10, 11, 12 (high coordination) are less common, but also prominent [35, 51, 64]. Some most common coordination numbers for several transition metal ions and the geometric arrangement of the ligands for each coordination number are shown in Table 2.3.
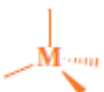
Table 2.3. The geometry of some transition metal complexes [64]

Coordination number	Geometric arrangement of ligands	Transition metal ions
2	Linear	Cu^+, Ag^+, Au^+
4	Tetrahedral	Co^{2+}, Ni^{2+}, Mn^{2+}
4	Square planar	Cu^{2+}, Ni^{2+}, Pt^{2+}, Au^{3+}
6	Octahedral	Fe^{2+}, Fe^{3+}, Cr^{3+}, Co^{2+}, Co^{3+}, Ni^{3+}, Mn^{2+}, Mn^{3+}, Ti^{3+}, Pt^{4+}

The regular coordination geometries of transition metal complexes visually are shown in Figures 2.3, 2.4, and 2.5. Generally, the most common CN for d-block transition metal ions is 6, usually with octahedral geometry. Additionally, d^6 metal ions tend to form 6-coordinated octahedral complexes where the formation of either N-bonded or S-bonded complexes is possible (Fig. 2.3) [35, 51]. Complexes with CN of 4 are fairly common for certain d-block metals. There are two types of 4-coordination as listed in Table 2.3. The square-planar and tetrahedral shapes (Fig. 2.3) are generally found in d^8 and d^{10} metal complexes, respectively. The 2-coordinated metal thiocyanate complexes are generally linear, not bent (Fig. 2.3) [35, 51, 64]. A CN of 1 is very unusual, although not unknown. Its formation depends upon the presence of a very bulky ligand which prevents the binding of additional ligands [35].

Less common metal complexes with CN of 5 can adopt either the trigonal bipyramidal or the square pyramidal structure (Fig. 2.3). This 5-coordinated structure is unusual among transition element complexes and, in complexes which are purely ionically bonded, would be unstable with respect to disproportionation into CN 4 and 6 species. The 3-coordinated metal complexes exhibit distorted trigonal planar structure (Fig. 2.3). Metal complexes with higher CNs such as 7-coordinated (pentagonal bipyramidal), the 8-coordinated (cubic) and 9-coordinated (tricapped trigonal prism) are unusual for d-block metals, although some examples exist among the complexes of the early second- and third-row metals (Fig. 2.4 and 2.5). The higher CNs of ≥ 9 are generally adopted by the f-block elements (rare-earth) [35, 51].

In general, the d-block metal complexes have a trigonal planar coordination geometry rather than the T-shaped or pyramidal structures encountered with p-block elements [35]. Moreover, sometimes the same transition metal ion can exhibit two or more coordination numbers or arrangements in different compounds (Table 2.2) [64].

Coordination			Comments
Number	Geometry	Polyhedron	
1	M—	—	Unimportant
2 Linear	—M—	—	Uncommon: found mainly with d^{10} metal ions
3 Trigonal plane	—M	◁	Rare; can be induced by use of sterically bulky ligands
4 Square plane	M	▢	Common for d^8 metal ions otherwise unusual;
4 Tetrahedron	M	△	Fairly common, especially for d^{10} and some d^5 ions
5 Trigonal bipyramid	M	◇	Rare ⎤ Examples are often similar in structure and energy so may easily Rare ⎦ interconvert
5 Square pyramid	M	◇	
6 Octahedron	M	◇	Very common; usually the most favoured energeticaly and gives the lowest ligand–ligand repulsions
(Octahedron = trigonal antiprism)	M	◇	An alternative view of an octahedron down a three-fold rotation axis
6 Trigonal prismatic	M	◇	Rare, and requires some extra steric or electronic benefit to be favoured over octahedral

Figure 2.3. The structures for coordination numbers 1–6 [35]

Coordination			Comments
Number	Geometry	Polyhedron	
7 Pentagonal bipyramid			Uncommon
7 Monocapped octahedron			Uncommon
8 Dodecahedron			Most sterically efficient geometric arrangement for eight equivalent ligands
8 Square antiprism			Uncommon
8 Cube			Rare; found only with the largest metal ions
8 Hexagonal bipyramid			Quite common for eight-coordinate complexes of metals with *trans*-dioxo ligands

Figure 2.4. The structures for coordination numbers 7–8 [35]

Most regular coordination polyhedra			
C.N. 9	10	11	12
Tricapped trigonal prism	Bicapped square antiprism	Octadecahedron	Icosahedron

Figure 2.5. The structures for coordination numbers 9–12 [35]

Based on literature data there is a number of studies which confirm that the coordination mode of transition metal thiocyanate complexes is strongly influenced by the surrounding environment. Firstly, according to Shurdha *et. al.* [49] and Homanen *et. al.* [65], the electronic structure and the steric hindrance (the main one from steric effects) are being most important on the final bonding mode. When a thiocyanate anion is N-bonded to a metal atom, the M–NCS arrangement is essentially linear, whereas the M–S–C angle is bent for the M–SCN bonding. Thus, the S-bonding has a higher steric demand than the N-bonding, and is disfavored by adjacent bulky ligands. In case of the square-planar complexes, both the electronic and steric effects are important for the determination of the coordination geometry and thiocyanate bonding mode. Electronic effect comes from the competition for π-bonding orbitals on the metal and it favors the S-bonding mode unless steric effects are large. When steric effects become larger, the N-coordinated bonding mode of thiocyanate group becomes favored rather than the electronically favored S-bonding [51, 54]. Additional important factor on the bonding mode of thiocyanate group is the nature of central metal ion [10, 20, 66, 67]. It was found the mutual relations between the bonding properties of SCN^- ion and the number of the positive charge on central atom, e. g. copper atom. In this case, the decrease of the effective positive charge increases the tendency of the formation of S-coordinated thiocyanate group and vice versa. The size of the effective positive charge itself could be influenced by the basicity of the N-donor ligands due to the varying π-bonding properties, inductive effect of substituents, different number of ligands and thiocyanate groups in the coordination sphere of the central atom [66].

Other relevant factors for coordination modes are the nature of other coordinated ligands (especially if they refer to the organic molecules) [49, 68, 69] as well as the presence of counter ions [69, 70]. According to Lawrance *et. al.* [24], dealing with ionic salts that are water-soluble, most of transition metal ions form complex ions with water molecules which behave as a ligand set. This is a common starting point for initiating other coordination chemistry. Most first row transition metals in the two commonest oxidation states form a stable complex ion with water as a ligand. However, water is a weak-field ligand and such complexes are prone to substitution reactions, when water molecules are successively replaced with other ligands. Due to the fundamental role of substitution reactions in many chemical, biological, and catalytic processes, they were investigated in many coordination chemistry mechanistic studies [28]. According to Supkowski *et. al.* [25], the knowledge of the number of water molecules occupying the first coordination sphere of a metal ion is of paramount importance in understanding the nature and reactivity of metal complexes in solution. They provided the example with proteins or nucleic acids which contain metal ion binding sites. In that case, the information about the number of coordinated water molecules allows one to deduce how many macromolecule-supplied ligating groups are present at the binding site.

Dealing with the intrinsic view of transition metal complexes in the solution an equally important aspect on the complex formation is the strong influence of solvent effects (or, more precisely, the solvation effects) [21, 23, 49]. Solvation effects have

the influence on the chemical reactivity [71] or equilibria in the solution [23], thus the behavior of transition metal complexes in solution is of great importance in coordination chemistry. Specific solvent interactions result in solvent molecules being placed at specific locations relative to the solute and can even evoke possible chemical effects such as charge transfer with the solvent. This is a reason why specific solvation effects are very important for inorganic complexes and, generally, for any system involving significant charge transfer [71]. Metal ions are solvated in the aqueous media and if the system contains any other molecules, such as bulky functional groups, those molecules that are simultaneously bound to the metal ion will be the subject to consequential steric interactions (already discussed above) through space. The molecular structure of a solvent, particularly, that of any functional groups in the vicinity of the coordinating atom to the metal ion, plays a key role in the solvation steric effects [72]. According to Ishiguro *et. al.* [72] in the case of six-coordinated transition metal(II) ions, the weak solvation steric effects induce a distorted octahedral structure, while the strong solvation steric effects decrease the solvation number (the number of solvent molecules simultaneously bound to a metal ion). The solvation steric effect itself is a decisive factor in reaction thermodynamics and kinetics of the metal ion. Additionally, it is well known that the solvation effect has influence on spectroscopic properties of molecules in solution [73, 74]. The solute-solvent interaction affects the solute's Raman spectrum [75, 76] and electronic absorption spectrum (this phenomenon is reffered to as solvatochromism) [74]. The onset of intramolecular interactions often leads to gross changes in band positions, intensity and shape, which can be explained in terms of changes in force constants, normal coordinates and electron redistribution due to the interaction [75, 76]. The influence of solvent effects in terms of changes of spectroscopic properties are discussed in more detail in following 2.2.4 section.

Recent study on metal thiocyanate complexes [77] has revealed that the position of the substituents in N-donor ligands dramatically influence the stability of Cd-based thiocyanate complex. Moreover, researches observed that for Cd as metal cation the compounds with a bridging coordination are more stable than those in which the anionic ligand is only terminal bonded. They assumed that this finding might be responsible for the former observation [77].

In spite of the possible influence of all factors (discussed above) on the final transition metal thiocyanate coordination chemistry, C.-H. Hsieh *et. al.* [78] highlighted that a search in the Cambridge Crystal Structure Data Base from 1990 to current indicates the M–NCS form greatly predominating in almost 500 deposited structures. The M–SCN bonding mode is typical for the extremely thiophilic metals such as Hg or Cd [78].

In general, the coordination chemistry of the thiocyanate group has been exploited extensively. Considerable interest involves not only the studies on interesting architectures and topologies which transition metal thiocyanate complexes could exhibit, but also the development of novel materials with useful chemical and physical properties.

2.2.3. Selected transition metal-thiocyanate complexes

2.2.3.1. Iron(III) thiocyanate as inorganic bridge

The atomic number of iron is 26 and its electronic configuration is $[Ar]4s^2 3d^6$. Iron has 14 isotopes. Among them, the mass of iron varies from 52 to 60. Pure iron is chemically reactive and corrodes rapidly, especially in moist air or at elevated temperatures. The most common oxidation states of iron are +2 and +3. Iron(III) complexes are generally in octahedral in shape, and a very few are in tetrahedral also [79]. The ionic radius of Fe^{3+} ($[Ar]3d^5$) of 74 pm is smallest compared with Fe^{2+} ($[Ar]3d^6$) of 84 pm or Fe atom of 126 pm. The cation is considerably smaller in size because the electrons in the n = 4 level have been removed from the iron atom. Removing another electron to form Fe^{3+} produces a small but noticeable decrease in radius. Generally, the trend is as follows: the greater the positive charge on the cation of the same element, the smaller the ionic radius [64]. Iron(III) ion with electronic configuration of 3d5 which corresponds to a half-filled d- sub-shell is particularly most stable [79].

First investigation into the aspects of the iron(III) thiocyanate complexation reaction appeared in 1931, when a spectral study (light absorption) of three different iron(III) thiocyanate complexes was made. It was concluded that the same species in each sample were responsible for the color [80]. Later investigations made by other researchers supplemented that assumption and proved that in the aqueous media iron(III) reacts with thiocyanate to give a red color complex. The appearance of red color is related to the formation of the $[Fe(NCS)_n]^{(3-n)}$ (n = 1–6) complexes and is interpreted in terms of the presence of the colored $[Fe(NCS)]^{2+}$ complex as the main species at low thiocyanate concentration. At very high thiocyanate concentration the $[Fe(NCS)_6]^{3-}$ tends to be formed. It was established that iron(III) ion is 6-coordinated in aqueous solution and has an octahedral structure. Additionally, iron(III) ion, as a hard acceptor, prefers to bond with the hard nitrogen donor [80, 81]. Literature data indicate that early studies on the iron(III) thiocyanate as inorganic compound were mainly focused on the determination of kinetics [82], formation constants [83, 84], solvent effects [85, 86]. The follow-up studies gained interest in developing new molecular-based magnetic materials. In this point of view a promising approach for the purpose is based on a bimetallic network. Skorupa *et. al.* [87] and others [88] made a characterization of heteronuclear thiocyanate-bridged compounds where the iron(III) thiocyanate is bound to certain metal ions having an organic ligand. In order to visualize what does the iron(III) thiocyanate as inorganic part in complex refers, the molecular structure of $(NiL)_3[Fe(NCS)_6]_2$ (where L = 5,6,12,13-Me$_4$-[14]-4,11-dieneN$_4$) is shown in Figure 2.6. In this case the complex $[Fe(NCS)_6]^{3-}$ anion binds through S atom of NCS ligand with Ni atom and not with organic ligand. In other cases, the metal-metal bonding mode could be observed.
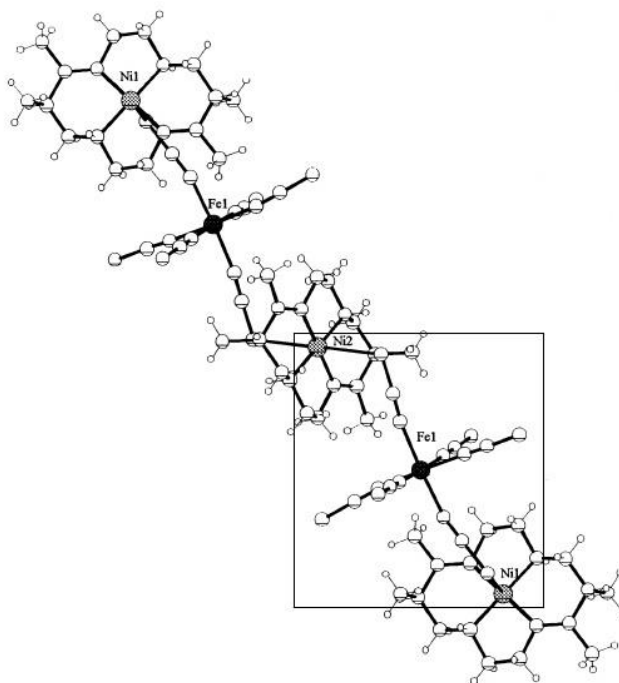
Figure 2.6. Molecular structure of $(NiL)_3[Fe(NCS)_6]_2$ with labeled metal atoms [87]

Since iron is widely used in industry, several studies on the inhibition of metallic corrosion in aqueous solutions by inorganic anions were performed [89, 90]. Researchers found out that thiocyanate can cause the passivation behavior of iron and steel in aqueous environment. The combination of cyclic voltammetry, Raman spectroscopy, surface-enhanced Raman spectroscopy (SERS), photoelectrochemical and electrochemical techniques provided informative results. The explored voltammograms, photoeffects, frequency shifts and coordination modes of SCN^- ion adsorbed on iron surface exhibited the electrode/electrolyte interface and confirmed the corrosion-passivation behavior of iron.

In the last two decades investigations were focused on the determination of optimum conditions for iron(III) extraction and separation procedures [91, 92]. Ivšić *et. al.* [91] established the optimum conditions for extraction of iron(III) from sulphuric and hydrochloric acid solutions containing the thiocyanate ions. Researchers found the method to be applicable for the determination of iron(III) in various soil samples and the amounts of tolerated foreign ions were defined [91]. At the same time other researchers proposed the simple, rapid, and economical method in terms of liquid-liquid extraction-separation of iron(III) by ammonium thiocyanate H_2O-n-propyl alcohol system in the presence of sodium chloride [92].

Moreover, the application of iron(III) thiocyanate system for the indirect determination of particular substances was one of the main interests discussed in that decade [15, 16]. It was revised that due to evaluated characteristic features of the formed iron(III)-thiocyanate complex, it is applicable to a range of quantitative

28

analysis of lipid containing materials which are interesting for biomedicine, food and industry [15]. Other works demonstrated a simple and sensitive method suitable and convenient for the determination of six phenothiazines (a group of drugs that are widely used as tranquillizers antihistamines and hypnotics) using potassium dichromate as an oxidant and iron–thiocyanate system for measuring the unreacted dichromate [16].

Despite of the fact that the effectiveness of thiocyanate for dissolving gold in the presence of suitable oxidizing agent was first demonstrated in 1905, the investigations on potential use of iron(III) thiocyanate (as leaching accelerator) system in the hydrometallurgy started before two decades and still continue [18, 19, 93]. Recent studies were based on the exploration of synergistic effects on the dissolution of gold by adding small amounts of iodine ions and/or pure iodine to iron(III) thiocyanate solutions [93]. Additionally, a number of uncertainties on the thermodynamics of the dissolution of gold in an acidic aqueous thiocyanate medium using iron(III) sulphate as an oxidant were investigated. Researchers tried to found out the fundamental chemistry aspects of chemically complicated gold/thiocyanate/sulphate/water system, containing a number of Lewis acids (gold(I), gold(II), iron(II), iron(III) and hydrogen ions) and Lewis bases (thiocyanate, sulphate, bisulphate and hydroxide ions). Thermodynamic studies also enabled to clarify the feasibility of the system, optimum experimental parameters, and the factors affecting the oxidative dissolution of gold [94]. On the basis of research results in 2003 the application to patent technology "Precious metal recovery using thiocyanate lixiviant" (No. US7285256 B2) [95] was submitted. Latest attempts of inventors refer to the series of papers with the purpose to explore and further understand the gold/iron/thiocyanate system through research involving thermodynamic analysis, leaching kinetics, thiocyanate stability, solvent extraction of gold and different strategies for the recovery of gold [18, 19, 96, 97].

According to all discussed studies, iron(III) thiocyanate as an inorganic compound demonstrates useful characteristic features that could be considered for variety of applications.

2.2.3.2. Iron(III) thiocyanate as inorganic-organic bridge

The design and synthesis of discrete iron(III) thiocyanate-based compounds, where the bonding between the iron(III) thiocyanate and organic ligand is presented, continue to be a research area of increasing importance. Based on found literature data, it seems that useful properties of iron(III) thiocyanate have a potential to be used largely in biochemistry sciences. Starting from nineties there was stemming interest on iron porphyrins found in proteins, peroxidases, cytochromes and etc. in order to find out physical properties of coordinated Fe(III) ion. H. Nasri *et. al.* [98] synthesized and characterized spectroscopically and structurally the isothiocyanate Fe(III) porphyrins complex displaying molecular structure and parameters [98]. Additionally, it was known that several metal complexes display anti-microbial activity which is due either to the metallic ion or ligands. Based on that knowledge, considerable interest in the field of series mixed-ligand dithiocarbamates-

thiocyanate with different transition 3^d metal ions was aroused. The explored complexes exhibited anti-bacterial action against several chosen bacteria [99]. Later the interest was paid in characterization of other biologically active iron(III) thiocyanate-based antipyrine [100], carboxamido and other [101, 102] compounds. Obtained results gave a better understanding of the kinetics and mechanisms of iron(III) chelation processes, functionality from the points of structural and catalytic activities. In the follow-up studies [103, 104] a particularly interesting aspect of research became seven-coordinated 3^d metal complexes. The molecular structure of one such type complex explored by Sarauli *et. al.* [104] is shown in Figure 2.7. Besides, this figure illustrates the case when Fe atom has the bonding mode not only with the NCS ligand, but also with organic molecule. The 7-coordinated iron(III) thiocyanate-based organic complexes are considered to be quite unstable and kinetically labile species, and their solution chemistry is largely undefined. Since a few years it was shown that these species exhibit extremely interesting chemical properties and catalytic activity. They are especially interesting as excellent low molecular weight and fast, even faster than natural enzymes, catalysts for superoxide $(O_2^{\bullet-})$ dismutation (SOD), providing important therapeutic applications. Moreover, they also show a general potential for being interesting redox active compounds. The results of performed studies showed that iron SOD mimetics are more desirable because of their higher kinetic and thermodynamic stability compared with the investigated manganese complexes. Furthermore, the works elucidated the behavior, reactivity, ligand substitution mechanism, binding modes of 7-coordinated iron(III) thiocyanate-based organic complexes [103, 104]. Additional class of considered compounds that has recently become of interest is nitrosyl iron complexes since it is of great significance to human physiology. In recent studies [78] thiocyanate iron nitrosyl species have been proposed in studies that mimicked conditions resulting from human consumption of iron supplements. Authors have studied the molecular and electronic structure, bonding modes, effect of ancillary ligands by means of modern DFT analysis, X-ray diffraction (XRD), infrared (IR) spectroscopy and Mössbauer spectroscopy.
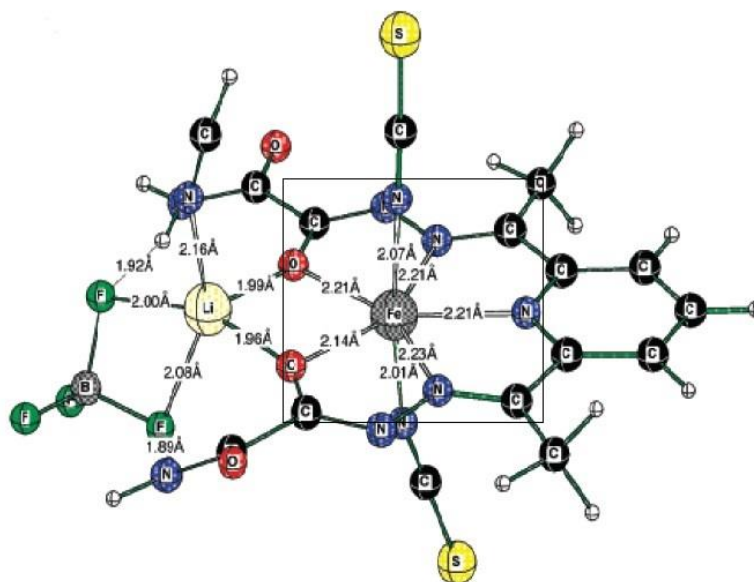
Figure 2.7. Molecular structure of $\{[Fe(dapsox)(NCS)_2]\cdot LiBF_4\}^-$ complex ion [104]

Due to characteristic features and chemistry of the iron(III)-thiocyanate complex, it finds an application in pharmaceutical sciences, especially in the field of tranquillizer studies. Kojlo *et. al.* [105] reviewed the results of studies related with the aspects of analytical application of the reaction of phenothiazines (substituted in the 2 and 10 positions) with oxidants, some metal ions and their ternary and binary complexes. They summarized that aforesaid compound exhibit many valuable analytical properties. They are easily oxidized in acidic medium with a number of oxidants. This property enables them to be used as redox indicators for the determination of some metals. Phenothiazines which are presented in aqueous solutions as large organic cations, react with thiocyanates of certain metals, and one of them is iron(III). The obtained compounds are insoluble in water and can be quantitatively extracted using organic solvents. These properties have been used for the extractive-spectrophotometric determination of some metals or phenothiazines itself [105]. Continuing studies [17] on psychotropic drugs have reported the simple, rapid, accurate, and precise method for determination of doxepin (antidepressant). The method is based on the formation of ion-association products of doxepin with iron(III) thiocyanate complexes quantitatively extracted into some organic solvents. The significant advantage of the proposed system is that it can be applied to the determination of individual components in a multicomponent mixture. This aspect is of major interest in analytical pharmacy, since it offers distinct possibilities in the assay of a particular component in complex dosage formulations.

The latest study has established a new area of application of iron(III) thiocyanate-based organic compounds. Bhattacharjee and co-workers [4] synthesized and characterized the anionic mixed-ligand complexes, $[FeLX_2]^{n-}$ (L =

$C_{12}H_{18}N_2O_2$, X = F, NCS, N_3) which may be used as stabilizing agents for the synthesis of metal nanoparticles.

2.2.3.3. Mercury(II) thiocyanate as inorganic bridge

The electronic configuration of mercury, Hg, with filled f and d orbitals ([Xe]$4f^{14}5d^{10}6s^2$), makes elemental Hg somewhat similar in stability to noble gas elements. Weak interatomic attraction yields its vapor to be monoatomic as well as the liquid state of the mercury at room temperature. It is quite soluble in water (60 µg/L at 25°C) and is oxidized to the metastable dimer Hg_2^{2+}, and to more stable Hg^{2+} forms. Because of the large size and stable electronic configuration ([Xe]$4f^{14}5d^{10}$), Hg^{2+} is easily polarized by interacting atoms. The strong covalent character of the C–Hg bond is the reason for the high stability of the methylmercury (MeHg) molecule [106]. Similarly, the Hg^{2+} ion forms very strong covalent bonds with soft Lewis bases (ligands) such as halides and sulphur compounds, but relatively weak bonds with hard Lewis bases such as fluorine. These properties make Hg the "softest" of all metals. Diverse bonding modes are the consequence of large Van der Waals radius and spherical d^{10} configuration of Hg. Acting as heavy metal with high biochemical toxicity, Hg^{2+} is a favorable and fashionable building block with flexible coordination environments, variable CN, usually 2, 3, or 4. The linear 2-coordination of Hg^{2+} is a very unusual structure for the metal [106, 107].

Currently, one of the most active fields in coordination chemistry, supramolecular and materials science is the research on the design and synthesis of crystalline coordination polymers. These compounds have gained attention as promising materials of the future with specifically tailored, useful properties, such as catalysis [108], ion-exchange [109], magnetism, electrical conductivity, non-linear optical (NLO) behavior, luminescence, porosity and gas storage, or drug delivery [11, 108–110]. The NLO materials have emerged as one of the most attractive fields of current research in view of its vital applications in areas like optical modulation, optical switching, optical logic, frequency shifting and optical data storage for developing technologies in telecommunications and signal processing [111]. In this connection it was established that organic materials possess good nonlinear properties whereas, lack in mechanical and thermal stability. On the other hand, inorganic materials are evident for their mechanical and thermal stability but shows low NLO properties. But the class of semiorganic materials found to show a good combination of NLO properties as well as mechanical and thermal stability [112, 113]. In this point of view metal ions received great attention because of fascinating properties in designing new metallorganic polymers known as coordination polymers, metal-organic coordination networks (MOCNs) or frameworks (MOFs) or organic-inorganic (semiorganic) hybrid coordination polymers in which metal-organic connectivities are combined by "inorganic bridges" [109]. The most frequently used bridging inorganic ligands are halide or pseudohalide ions, among which the SCN⁻ ligand plays a crucial role in combining the versatile ambidentate character with two donor atoms [11, 109].

Since the M[Hg(SCN)$_4$] containing M = Zn, Cd, Cu, Ni, Co, Fe, or Mn have been already investigated from 1901 [11], the very recent studies have shown that Hg^{2+} presented in the tetrahedral anion [Hg(SCN)$_4$]$^{2-}$ provides an interesting design possibility. In dependently on a structure of cationic building block it can form 2D or 3D structures. Furthermore, previously studied Hg(CN)$_2$-based coordination polymers represented unusual examples of mercury(II) mediating a magnetic interaction [114]. Based on those findings, the midst of various semiorganic NLO materials – bimetallic mercury thiocyanate complexes have attracted many researchers as will be presented in following sections.

Based on recently published papers [11, 110, 115] it is clear that heterometallic thiocyanate bridged Cu(II) and Hg(II) coordination complexes or Cu(II) doped MHg(SCN)$_4$ [112, 113] complexes are the main group used as potential building blocks for new coordination polymers. Researchers have characterized each synthesized complexes mainly by means of ultraviolet (UV), IR, Fourier transform infrared (FTIR), Raman spectroscopies, thermal and optical transmission analysis, XRD analysis and etc. Additionally, most of studies were supplemented by theoretical modeling mostly using DFT calculations. Investigations of heterometallic thiocyanato bridged Cu(II) and Hg(II) coordination complexes have contributed to the understanding that even small changes of steric and electronic properties in the ligand [110] as well as counter ions [11] can have a significant impact on the topology of coordination polymer. Generally, the type and topology of the coordination polymers depend on the metal element, valences and geometries needs of the metal ion and functionality of the ligand [115]. Based on results of research it was concluded that the analyzed Cu(II) and Hg(II) coordination complexes were found to be suitable for NLO applications as materials displaying good thermal stability, optical, and magnetic properties [112, 113]. The structure, bonding modes of explored heterometallic thiocyanate bridged Cu(II) and Hg(II) coordination complex are shown in Figure 2.8.
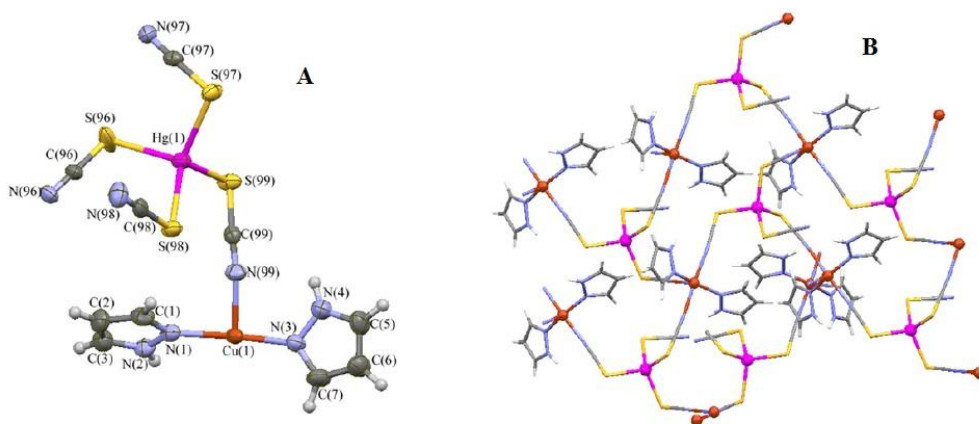
Figure 2.8. Molecular structure (A) and 2D structure (B) of [Cu(pzH)$_2$Hg(SCN)$_4$]$_n$ Color codes of (B): orange, Cu; pink, Hg; yellow, S; purple, N; grey, C [110]

The second group of currently investigated heterobimetallic coordination structures refer to the use of Mn(II) together with Hg(II) [108, 114, 116]. Authors have determined the structure, magnetic behavior, electronic and NLO properties using combined theoretical and experimental techniques [108, 114] or only detailed theoretical investigations [116].

The Fe(II) and previously described Fe(III) appear to have useful properties for the application in NLO materials of the bimetal-thiocyanate family together with Hg(II) too [117, 118]. It was recognized [117] that incorporation of Fe^{3+} ion in the mercury ferric chloride tetrathiocyanate ($Hg_2FeCl_3(SCN)_4$) makes this complex thermally stable up to ~ 234 °C. This is comparatively far better than the thermal stability of mercury cadmium chloride hexathiocyanate $Hg_3CdCl_2(SCN)_6$ and other analyzed metal-organic coordination complexes. Moreover, the dielectric studies revealed that the sample exhibits low dielectric constant and dielectric loss at higher frequencies. The incorporation of Fe^{2+} ions in the heterometallic thiocyanate complexes displays also attractive properties. Researchers concluded [118] that in the case of thermal decomposition of $FeHg(SCN)_4$ the feature of the formation of metal(II) sulfides can be used as the sources to obtain the low cost compound-semiconductor thin films consisting of metal sulfides.

2.2.3.4. Mercury(II) thiocyanate as inorganic-organic bridge

A number of hybrid MOF structures have been obtained due to the development in coordination chemistry. It is well documented that optimal matching of the coordination modes of organic ligands and metal ions facilitates generation of desired coordination polymers [119]. Up to now, a boost on the synthesis and studies of metal-based mixed-ligand inorganic-organic frameworks has been given by the discovery of a wide variety of multidimensional crystalline phases. This interest is based on their encouraging properties and exceptional potential applications [120].

Currently, the design and synthesis of mono-, di- and polynuclear complexes of Group 12 metal ions continue unabated for their application in electronic and optoelectronic devices [122]. In contrast to coordination polymers of transition metal ions, the formation of polymers with heavy metal ion such as Hg(II) seems to be surprisingly sparse. Until recently there have been very few reports on Hg(II) complexes with rigid or flexible organic nitrogen donor based ligands [121]. Hence, the need for knowledge of Hg(II) behavior has turned the attention of researchers towards the Hg(II) compounds having the inorganic and organic ligands. The essential prerequisites for above mentioned applications are the research based judicious choice of organic spacers and inorganic/organic bridges that may lead to directed properties [122]. In this point of view, due to advantageous properties [42, 123] Schiff bases as chelating agents have attracted great interest and are the major issue in the development of metal-based coordination polymers [42, 122–126]. Moreover, it was established that pseudohalides, such as SCN ligand with versatile bridging behavior, in combination with Schiff bases may afford different monomeric, dimeric, polymeric MOFs [124] (Fig. 2.9) with specific structural

features and optical and magnetic properties [120]. The main objective of studies was to understand how molecules can be organized and how functions can be achieved. In order to achieve the purpose, a variety of mercury-based complexes have been synthesized using different organic molecules. Their structures and properties have been physically and chemically determined. Performed investigations showed that for the physical characterization of prepared complexes, most frequently used spectroscopic techniques were XRD, ultraviolet-visible (UV-Vis), IR, FTIR, nuclear magnetic resonance (NMR) [122–125] or fluorescence [124] spectroscopies, as well as thermal analysis in each case. Besides, all of these studies were supplemented by theoretical modeling. Based on obtained data researchers have described molecular structures, bridging modes, thermal, magnetic, luminescence behavior of each synthesized material.
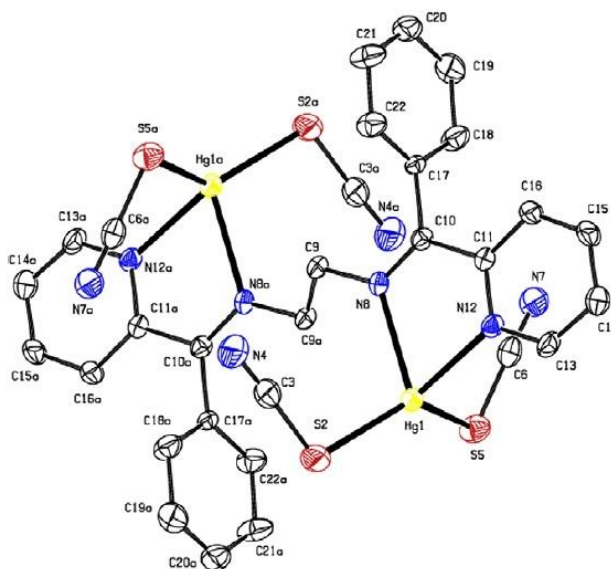
Figure 2.9. Molecular structure of $[Hg_2(L)(SCN)_4]$ (L = Schiff base) [124]

The second widely discussed chelating agent group in metal inorganic-organic supramolecular chemistry is pyridine based organic molecules [119, 127, 128]. It was observed that pyridine based complexes act as efficient competitive ligands toward halides for coordination sites of Hg center [127] and display the luminescence properties stemming from the conjugated aromatic cores of these molecules [128]. Moreover, there has been considerable interest in terpyridine based complexes because of their properties as intercalating metalloreagents to nucleic acids as well as their intriguing spectroscopic behavior and special functional properties such as optics, separation, and catalysis [128].

Owing to the potential of application of mixed-ligand metal materials, the interest in investigations of various organic molecules such as pyridyl [129], pyrazine [121] and other [8, 107, 120] with Hg is still ongoing. Previous works have

shown that the organic functional groups mentioned above are very important for molecular based photonic, electronic, and ionic devices. Nevertheless, dealing with such complex system as metal inorganic-organic networks, the multifariousness of possibilities causes a challenge to predict accurately the nature of the compounds which will be obtained after synthesis. For this reason researchers have analyzed how the replacement of certain group [121], modification of chelating agent [8], molar ratio of the mixed ligands [107, 120], may influence the structure and properties of the prepared mercury-based polymeric network. It was concluded that the main factors significantly influencing the overall framework of desired complex is a nature of metal centers and organic ligands (e.g. variable coordination of the metal ions, the multiple coordination sites, binding modes of the organic ligand, as well as their molecular structures) [107], and inorganic counter ions and the metal to ligand ratio, and solvent [129].

2.2.4. Solvent effects on molecular structure and spectroscopic properties of transition metal complexes in aqueous environment

The understanding of solvation phenomena is of great importance in order to rationalize experimental results obtained when a molecule interacts with a liquid environment. This is an every day need in chemistry laboratory where most molecular spectra are recorded in a specific solvent [130]. From the macroscopic point of view, it is well known that the photo-physical behavior of a dissolved substance depends on the nature of its environment. In this context, the intensity, shape, and maximum of the absorption band of substance in solution depends strongly on the solvent-solute interactions and solvent nature. The solvent dependant spectral shifts can arise either from non-specific (dielectric enrichment) or specific (e. g. hydrogen-bonding or bulk solvent properties) solute-solvent interactions [131, 132]. For the molecular systems without intramolecular hydrogen bond, the spectral shifts are sensitive to the solvent polarity [132] which is commonly used term related to the capacity of a solvent for solvating a dissolved charged or neutral species [131]. It is already confirmed that the positions, intensities and shapes of the absorption bands are usually modified when absorption spectra are recorded in solvents of different polarity. The band changes are a result of physical intermolecular solute-solvent interaction forces which tend to alter the energy difference between ground and excited state of the absorbing species containing chromophore. Attempts to express it quantitatively have mainly involved determination of physical properties of solvent such as relative permittivity, dipole moment, or refractive index, but these parameters cannot effectively account for the multitude and specific interactions of solute-solvent on the molecular-microscopic level [131, 132]. Apart from these interactions, there are several other factors that may influence the spectra such as acid-base chemistry or charge-transfer interactions [132]. Generally, it is accepted that the presence of specific and non-specific interaction between the solvent and solute molecules are responsible for the change in the molecular geometry, electronic structure and dipole moment of the solute [133].

36

From a microscopic point of view, solvation involves the formation of a set of interactions between a solute and a solvent as well as a change in the interactions of the solvent molecules in the vicinity of the solute. Thus, a key step in the understanding of solvation is the determination of the structure adopted by solvent molecules around the solute, since the nature and strength of the associated interactions is intimately connected to the macroscopic properties of the solvated system. Based on that, a large body of work focuses directly on elucidating the solvent shell structure around the solute. Particular attention should be paid to the structure of the hydration shell around ions and to the solvation of hydrophobic solutes [134]. With a reference to this approach the computation of properties of metal complexes by utilizing first-principles (ab initio) quantum theoretical methods has traditionally met with great challenges. According to Erras-Hanauer *et. al.* [28], the advent of modern DFT methods for molecular systems has revolutionized computational chemistry, especially for the transition metals. The accurate modeling of molecules in solution using quantum chemical calculations requires realistic models for the interaction of the solvent with the molecule.

Two main approaches exist to estimate solvent effects: implicit (or continuum) and explicit models. In the implicit model the solvent is considered implicitly and the effect of the polarizable environments on the electronic structure of the solute is characterized. This works very well for rigid molecules and allows to calculate solvation free energies or other properties very efficiently, which depend on the electrostatic solvent response only (e.g. electronic exited states). The implicit solvation model has been found to be successful in a large number of applications. Its major difficulty is that the implicit solvation lacks a description of the specific solute-solvent interactions (e.g. hydrogen bonds, ion pairing, π-interactions). Moreover, in the implicit solvation models, the solute-solvent border needs to be correctly polarised.

The extension of the implicit solvation model is the inclusion of solvent molecules explicitly in order to get a better grip on the specific interactions like hydrogen bonding. This model is more accurate, but also more demanding of computer resources [130, 135–138]. According to Wang *et. al.* [138] explicit solvent models have a far greater capacity to capture the physical details of the solvent. As an example, authors described the classical water model, which not only correctly reproduces the zero-frequency dielectric constant of water, but it also decribes the fine-grained structure of water and hydrogen bonding effects empirically using a combination of electrostatic point charges and van der Waals interactions. Finally, there are a number of studies which summarized that the inclusion of explicit water molecules is a key factor for obtaining reliable computational results in comparison with experimentally obtained [139–142]. Nevertheless, Autschbach [29] showed that in computational modeling of heavy metal NMR parameters a reasonable description of the experimental trends requires to include at least one explicit solvation shell in case the metal has open coordination sites, and at least the implicit solvation model to estimate the effects of a second, third and so on solvation shells. In complement, it was demonstrated [130] that both solvation models are important

for the evaluation of electronic excitations. Considering solvation effects on electronic properties, the solute-solvent interactions affect the internal (nuclear and electronic) degrees of freedom of a solute and as a consequence the changes of electron distribution may be expected. These changes alter the chemical properties of solute, such as lengthening in the dipole moment, the change in the molecular electrostatic potential, the variation in the molecular volume, and even the spin density. In general, the theoretical methods can provide insight into the effects of the solvent on the solute charge distribution. Herewith, the impact of a solvent on the spectroscopic characteristics of a solute is the subject of an intense research effort. The effect of solvation on electronic transitions in the ultraviolet or visible range can be explained by considering the differential solvation of the ground and excited states, which depends on the change in the solute charge distribution in these two states. Since electrons are expected to be less tightly held in the excited state, the solute's charge separation should decrease upon its transition from the ground to an excited state, and the solute-solvent electrostatic interactions are thus generally expected to cause a blue shift in the spectra. On the other hand, dispersion effects tend to favor the excited state, since it is usually more polarizable than the ground state, and this tends to produce red shifts upon solvation. Overall, the direction of solute's spectral shift upon solvation depends on relative polarity of the solute in both its ground and excited states as well as on the solvent's polarity and polarizability. The extreme velocity of photoexcitation precludes any large-scale solvent reorganization during this process. Therefore, for an absorption process, the excited state of the solute "fits" into the cage structure which the solvent molecules adopted to accommodate the ground-state charge distribution of the solute. Currently, in order to describe these processes theoretical modeling is a valuable tool.

There are also notable solvent effects on vibrational spectra which depend on the magnitude of both nonspecific and specific, i.e., hydrogen bond, solute-solvent interactions. Theoretical representation of these effects is especially difficult, since it is necessary to separate the inertial and non-inertial portions of the solvent response, and this requires a careful evaluation of both the nature of the solute vibrations and the properties of the surrounding medium [134].

2.2.5. Application of vibrational and absorption spectroscopies for the characterization of transition metal complexes

According to Schmidt *et. al.* [27], the vibrational spectroscopic techniques are powerful analytical tools, which provide information on the physical/structural and chemical composition of a sample without a *priori* knowledge. The main feature of vibrational spectroscopy is its intrinsic chemical sensitivity that provides unambiguous information on the molecular and structural composition of a sample with an intense absorption band at the excitation wavelength used. Besides, the radiation used does not harm the sample, and no extrinsic labeling or staining which may perturb the system under investigation is necessary [27]. Furthermore,

vibrational spectroscopy is commonly used to characterize transition metal complexes [26].

Raman spectroscopy is similar to the IR spectroscopy, but the theory of Raman scattering is more complex than the theory of IR absorption. IR arises from a direct resonance between the frequency of the IR radiation and the vibrational frequency of a particular normal mode of vibration. The property of the molecule involved in the resonant interaction is the change in the dipole moment of the molecule with respect to its vibrational motion. IR absorption is a one-photon event. The IR photon encounters a molecule, the photon disappears, and the molecule is elevated in vibrational energy by the energy of the photon at the frequency of vibrational resonance. Simply speaking, IR measures the absorption of infrared light by the sample as a function of frequency. The molecule absorbs $\Delta E = h\nu$ from the IR at each vibrational transition. By contrast, Raman scattering is a two-photon event. In this case, the property involved is the polarizability of the molecule with respect to its vibrational motion. The interaction of the polarizability with the incoming radiation creates an induced dipole moment in the molecule, and the radiation emitted by this induced dipole moment contains the observed Raman scattering. This light scattered by the induced dipole of the molecule consists of both Rayleigh scattering (is strong and has the same frequency as the incident beam, ν_0) and Raman scattering (is very weak ~ 10^{-5} of the incident beam and has frequencies $\nu_0 \pm \nu_m$, where ν_m is a vibrational frequency of a molecule. The $\nu_0 - \nu_m$ and $\nu_0 + \nu_m$ lines are called the *Stokes* and *anti-Stokes* lines, respectively). Rayleigh scattering corresponds to the light scattered at the frequency of the incident radiation, whereas the Raman radiation is shifted in frequency, and hence energy, from the frequency of the incident radiation by the vibrational energy that is gained or lost in the molecule. All these aspects apply that polarizability consists of two components: one is associated with the incident photon and the other with the scattered photon. Thus, in Raman spectroscopy, the vibrational frequency (ν_m) as a shift from the incident beam frequency (ν_0) [143, 144]. The differences in mechanism between Raman and IR spectroscopies are shown in Figure 2.10. The observation of a vibrational band in the Raman spectrum depends on the presence of an accompanying change of the amplitude of the induced dipole moment. The intensity depends on the magnitude of this change. In general, in the case of a diatomic molecule, this change is less sensitive than the change of dipole moment to the environment of the vibrating group. As a result, a group of vibration intensities is more accurately transferable from one molecule to another and from one phase or solvent to another, in the Raman spectrum than they are in the infrared spectrum [145].

In order to record Raman spectra there are two types of equipment used: dispersive and Fourier transform (FT-Raman) spectrometers. Here, a laser is used for the excitation. The selection of laser depends on the type of a sample. For the inorganic sample analysis simple and cheap laser beam of 632.8 nm or 532 nm wavelengths is used. If the sample consists of organic compounds the laser beam of 785 nm or 1064 nm wavelengths is applicable. The advantages and disadvantages of each type spectrometer are listed in Table 2.4 [146].

IR

Raman

$v_0 \pm v_m$(Raman scattering)

v_0(Rayleigh scattering)
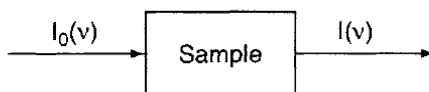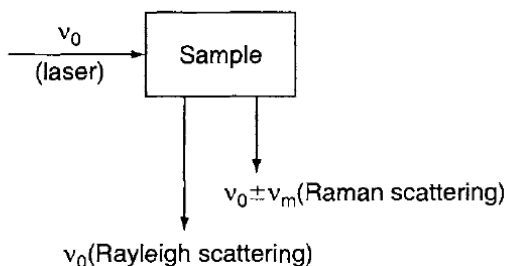
Figure 2.10. Differences in mechanism of Raman *vs.* IR spectroscopies [144]

Table 2.4. Comparison of the dispersive and FT-Raman spectrometers [146]

Type of spectrometer	Advantages	Disadvantages
Dispersive	λ_L^* varies between 220 nm and 785 nm	Applicable not for all samples (because of fluorescence)
	High sensitivity	Resolution is diverse in the entire spectrum
	The RR** experiments are possible	It is compulsory to calibrate the axis of frequencies
	Moving parts are not necessary	
FT-Raman	There is no fluorescence effect	Limited sensitivity
	It is possible to use $\lambda_L > 1000$ nm, usually it is $\lambda_L = 1064$ nm	Large output of laser radiation
	Automatic calibration of frequency axis in each measurement	Water absorption
	Designed libraries of spectra	

* λ_L – the wavelentgh of laser beam
** RR – resonance Raman scattering occurs when the sample is irradiated with an exciting line whose energy corresponds to that of the electronic transition of a particular chromophoric group in a molecule. Under these conditions, the intensities of Raman bands originating in this chromophore are selectively enhanced by a factor of 10^3 to 10^5 [146].

For the characterization purpose of any given substance, Raman spectra are interpreted by the use of known group frequencies and thus it is possible to characterize the substance as one containing a given type of group or groups. Although group frequencies occur within "narrow" limits, interference or perturbation may cause a shift of the characteristic bands due to either the

electronegativity of neighboring groups or atoms, or the spatial geometry of the molecule. Functional groups sometimes have more than one characteristic absorption band associated with them. Additionally, two or more functional groups often absorb in the same region and can usually only be distinguished from each other by other means. One of the most common alternative ways of removing the interference of other group modes is deuteration (isotope effect). For isotopic molecules, i.e. molecules that differ only by the mass of one or both of the nuclei (for example H/D) but not by their atomic number (for example $H^{35}Cl$ and $H^{37}Cl$) the vibrational frequencies are obviously different [141, 147]. In the context of characterization using Raman active group frequencies, the SCN^- ligand should be emphasized. This ligand serves as ideal candidate for a systematic experimental and theoretical examination of vibrational dynamics and has historically been employed as a descriptor of numerous inorganic complexes having this anion. The linear SCN^- anion has only three normal modes: ν_1 (CS stretching at the ca. 750 cm^{-1}), ν_2 (SCN bending at the ca. 470 cm^{-1}) and ν_3 (CN stretching at the ca. 2190–2020 cm^{-1}), which are both active in the IR and Raman spectra. It is highlighted, that due to large oscillator strength of the CN stretching vibration, as well as its position in the spectrum, which is relatively free of interferences, it has long been used as a diagnostic measure of thiocyanate-based complexes [148–151].

Currently, it is well known that because of extended vibrational coupling and the influence of ionization of ending groups, the adequate prediction and interpretation of the vibrational spectra requires the use of quantum chemical calculations [152, 153]. The benefit of such calculations is not so much in the calculated frequencies themselves, which after all are easily gained from the experimental spectrum. But the calculations yield additional information about the mode symmetries and the movements of the atoms involved in the particular vibrations. These can be used to understand changes in frequencies or other features of the experimental spectrum, like peak intensity or broadening that result from changes in pressure, temperature, or chemical composition. Furthermore, deviations from the ideal structure and its expected spectrum can be identified, and the presence of impurity phases can be spotted [154]. Generally, there are two ways to interpret a theoretical vibrational spectrum of a molecule: a visualization of the atom movement, and potential energy distribution (PED) analysis. The first is simple, but trivial and deceptive. First of all because of overestimation of hydrogen atoms movements, which are visible but often, engage negligible energy of the mode. This is especially striking for large molecules in which some normal modes are extended over entire molecule. The PED analysis is more accurate and enables to quantitatively describe the contribution of movement of a given group of atoms in a normal mode. Nevertheless, the PED analysis also has a limitation originating from ambiguity of the solutions. Therefore, a correct PED interpretation requires spectroscopic knowledge and thoroughness of the interpreter [155].

In complement, an important role is played by Raman spectra subtraction procedures in order to perform assignments of fundamental vibrational modes properly. For instance, s systematic noise in the solute spectra can be eliminated by

subtraction of the pure solvent spectrum, which contains the same systematic noise pattern [156].

Beautiful colors and rich excited state (ES) behavior are prominent features of transition metal coordination chemistry. These colors are a visual manifestation of quantum mechanics and are determined by the electronic structure of the compounds [157, 158]. Understanding of the structure and dynamics of electronically ESs is an important goal of current spectroscopic, photophysical, photochemical and theoretical research. As it was mentioned in the 2.2.4 section, besides their fundamental importance, these studies are increasingly driven by various applications of transition metal compounds [136, 158]. In order to characterize the structure and bonding of molecules in the electronic ground-state (GS) or ES, the most commonly used technique is UV-Vis spectroscopy [157]. The recorded UV-Vis spectrum refers to a various electronically ESs (metal-to-ligand charge transfer, MLCT; ligand-to-metal charge transfer, LMCT; ligand-to-ligand charge transfer, LLCT; metal-centered, MC). Namely, the presence of electronic states of different nature, localization, dynamics and reactivity in a limited domain of energy gives unconventional photophysical and photochemical properties to this class of molecules and explains the versatility and the richness of their photochemistry. Moreover, these specific properties responsible for the occurrence under irradiation of fundamental physico-chemical processes such as electron/energy transfer, bond breaking/formation, isomerization, radical formation, and luminescence can be tailored chemically and more recently controlled by shaped laser pulses [159]. In particular, it is necessary to understand the redistribution of electron density brought by optical excitation and the ensuing structural response of both the excited molecule and its immediate environment. As it is seen, the understanding of the GS and ES is demanding, but certainly can be complicated. Anyone, dealing with the photochemical calculations of the ES knows that they are usually intricate, time consuming and very involved. However, there is a fascination in computing of the ES. The possibilities that a molecule has after electronic excitation are plenty and the disentangling of these mechanisms has thrilled computational chemists [158, 160]. According to González *et. al.* [160], the understanding and controlling of photoexcited systems will be crucial for future research in many branches of optics and photonics. Therefore, the interrelated problems of characterization of ES and understanding their dynamics can be addressed by combining experimental and theoretical approaches. Twinning experimental ES studies with quantum-chemical calculations provides a deep insight into the ES character, dynamics and relaxation pathways, well beyond experimental observations [158]. However, the interpretation of the recorded spectra as well as unveiling the molecular stages experienced by the photoactive molecule requires a strong synergy between spectroscopists and theoreticians [160]. Today, the time-dependent DFT (TD-DFT) theory emerges as one of the most practical tools that can be used to predict the electronic properties of transition metal complexes. This method based on the linear response theory is the subject of recent and promising theoretical developments. The treatment of molecular properties by means of the linear response of the charge density to an

applied field is based on a well founded formalism that allows direct computation of polarizabilities, excitation energies and oscillator strengths within the framework of the DFT [159]. Usually, the agreement between the experimental and TD-DFT theoretical absorption spectra depends strongly on the choice of the functionals and basis sets, and on the importance of the surrounding effects which may vary from one molecule/solvent system to another one [159, 161]. Nevertheless, for the time being, the TD-DFT may be the only way to study absorption properties of molecules. Promising functionals and methods have been developed in the last years [160] and the calculation of an absorption profile as a sum of calculated shaped bands appears to be a useful and simple procedure to estimate even low-resolution absorption spectra of transition metal complexes [162].

3. METHODOLOGY

3.1. Methods

The characterization of iron(III) and mercury(II) thiocyanates was done using the following techniques:
1. Raman spectroscopy (Raman spectra of aqueous mixtures at the pH values ~ 2 were recorded);
2. UV-Vis spectroscopy (UV-Vis spectra of aqueous mixtures at the pH values ~ 2 were recorded);
3. Theoretical modeling.

3.1.1. Raman spectroscopy

Raman spectra were recorded in the Department of Organic Chemistry, Center for Physical Sciences and Technology by dr. Ieva Matulaitienė and dr. Zenonas Kuodis. The Echelle type spectrometer RamanFlex 400 (PerkinElmer, Inc. USA) equipped with thermoelectrically cooled (-50 ^{o}C) charge-coupled device (CCD) camera and fiber-optic cable for excitation and collection of the Raman spectra was used. The 785-nm beam of the diode laser was used as the excitation source. Spectra were collected with an integration time of 10 s. Each spectrum was recorded with accumulation of 30-50 scans, yielding total acquisition time of 300-500 s. The wavenumber axis was calibrated using the polystyrene standard (ASTM E 1840), yielding ± 1 cm^{-1} absolute wavenumber accuracy for well defined narrow bands. Intensities were corrected by the intensity standard (SRM 2241) of National Institute of Standards and Technology (NIST). All experiments were performed at least in triplicate.

Parameters of overlapped bands were determined by fitting the experimental contour with Lorentzian-Gaussian form components by using the Grams/AI 8.0 software (Thermo Scientific, Inc. USA) [163]. For the visualization of vibrational spectra the Chemcraft graphical program was used [164]. Detailed assignments of fundamental Raman active vibrational modes were made by isotopic exchange and Raman spectra subtraction procedures. pH/pD measurements of the prepared samples were performed using the pH meter HI 9321 (HANNA Instruments, Inc. USA). The analysis of Raman spectra was performed in collaboration with dr. O. Eicher-Lorka (Department of Organic Chemistry, Center for Physical Sciences and Technology).

3.1.2. UV-Vis spectroscopy

UV spectra of the samples were recorded in the Department of Organic Technology of Kaunas University of Technology. The spectra were acquired on Lambda 35 UV spectrometer (PerkinElmer, Inc. USA) using 2-mm quartz cuvette at wavelengths ranging from 200 nm to 700 nm. All experiments were performed at least in triplicate. pH measurements of the prepared samples were performed using the pH meter HI 9321 (HANNA Instruments, Inc. USA). The analysis of spectra

was performed by using the Grams/AI 8.0 software (Thermo Scientific, Inc. USA) [163]. The visualization of electronic spectra was done using the Chemcraft graphical program [164]. The analysis of electronic spectra was performed in collaboration with dr. O. Eicher-Lorka (Department of Organic Chemistry, Center for Physical Sciences and Technology).

3.1.3. Theoretical modeling

Theoretical modeling and calculations were performed in collaboration with dr. O. Eicher-Lorka (Department of Organic Chemistry, Center for Physical Sciences and Technology) using Gaussian for Windows package version G03W [165].

3.1.3.1. Optimization of molecular structure

The geometry optimizations of iron(III) monoisothiocyanate were accomplished with the DFT method, using the unrestricted Becke three-parameter hybrid functional combined with Lee–Yang–Parr correlation functional (B3LYP) [166, 167] and hybrid functional of Perdew, Burke and Ernzerhof (PBE1PBE) [168] functionals in the sextet high spin state (S=5/2) [169]. For all atoms except the Fe, which was treated with pseudopotentials, the 6-31++G(d,p) [170] basis set was used. The Stuttgart relativistic effective core potential (ECP) 10MDF basis set [171] for the Fe atom was applied. To take into account the solvent effect, some calculations were done using the polarizable continuum model (PCM), specifically integral equation formalism (IEF) model, further referenced as IEFPCM [172]. The geometry optimizations of mercury(II) thiocyanates ($[Hg(SCN)_n]^{2-n}$, where n = 2–4) were accomplished with the DFT method, using the B3LYP functional. Almost all calculations except Hg, which was treated with pseudopotentials, were done using 6-311++G(d,p) basis set. For the Hg(II) atom Stuttgart relativistic ECP 78MWB basis set [173] was used. IEFPCM model was used for the solvent effect calculations. For the calculations involving the simulation of solvent effect, the SURFACE=WDW, ALPHA=1.21 and TSNUM=70, instead of the default settings in order to avoid the oscillatory behavior often encountered during optimization, was set. Several starting geometries failed to converge, and a number of trial structures were required before convergence was achieved.

In order to elucidate the most reliable structure of analyzed iron(III) and mercury(II) thiocyanates, the calculations with explicitly (the water molecules are placed around the simulated solute molecule) or/and implicitly (the solvation effects are calculated by extra terms of the force fields), added water molecules in the first coordination shell were carried out.

For the visualization of optimized geometries the Chemcraft graphical program was used [164].

3.1.3.2. Theoretical modeling of Raman spectra

The frequency calculations of iron(III) monoisothiocyanate were performed with the unrestricted B3LYP and PBE1PBE functionals. The detailed assignments of vibrational modes were based on the potential energy distribution (PED) analysis, which was performed using the software VEDA 4 [174].

The frequency calculations of mercury(II) thiocyanates ($[Hg(SCN)_n]^{2-n}$, where n = 2–4) were performed with the B3LYP functional. Only the calculated frequencies of $C{\equiv}N$ bond were scaled by the 0.9688 scale factor and other were left unchanged [175].

Vibrational spectra were processed and managed using the Grams/AI 8.0 software (Thermo Scientific, Inc. USA) [163]. For the visualization of electronic spectra the Chemcraft graphical program [164] was employed.

3.1.3.3. Theoretical modeling of UV-Vis spectra

The electronic spectra of iron(III) monoisothiocyanate complex were calculated with the B3LYP, Coulomb-attenuated B3LYP functional (CAM-B3LYP) [176] PBE1PBE and the gradient-corrected correlation functional of Perdew, Burke and Ernzerhof (PBEPBE) [177] methods using TD-DFT approach on optimized geometries. The calculations using CAM-B3LYP functional were performed by dr. Juozas Šulskus (Vilnius University, High Performance Computing Center) using Gaussian09 version [178].

The electronic spectra of mercury(II) thiocyanates ($[Hg(SCN)_n]^{2-n}$, where n = 2–4) were calculated with the B3LYP, PBE1PBE and PBEPBE methods using TD-DFT approach on optimized geometries. Electronic spectra were processed and managed using the Grams/AI 8.0 software (Thermo Scientific Inc. USA) [163]. The visualization of electronic spectra was done by the Chemcraft graphical program [164]. The obtained intensities were broadened using Lorentzian shape functions with a constant half-width, which was adjusted manually in the range of ~ 20–30 cm^{-1} to match the corresponding experimental spectrum.

The nature of the main electronic transitions was characterized by the analysis of the natural transition orbitals (NTO). The NTO were obtained using the output files of Gaussian software with appended additional commands.

3.1.3.4. Isotopic substitution and ligand arrangement

In order to perform the assignments of fundamental vibrational modes of each analyzed iron(III) and mercury(II) thiocyanate complex properly, the isotopic substitutions for the experimental and theoretical studies were applied. For this purpose the H_2O/D_2O isotopic substitution was made.

In the case of iron(III) monoisothiocyanate, the influence of different position of SO_4^{2-} ligand *vs*. NCS^- ligand upon its geometry and vibrational frequencies was evaluated by means of theoretical modeling. In the first case the SO_4^{2-} ligand was placed beside the NCS^- ligand, in the other case the SO_4^{2-} ligand was placed on the opposite of the NCS^- ligand. Additionally, the experimental Raman spectra analysis

46

on the vibrational band changes of iron(III) monoisothiocyanate influenced by the presence of additional anions (Cl^-, SO_4^{2-}, NO_3^-) was performed.

3.2. Chemicals and solutions for experimental study

3.2.1. Chemicals

All chemicals (Table 3.1) were of analytical-reagent grade, purchased from Sigma Aldrich and used without further purification. Acidified distilled water and heavy water (deuterium oxide D_2O) were used as the solvents throughout the solution preparation in order to avoid the hydrolysis of iron(III) and mercury(II) salts.

Table 3.1. Chemicals used for the experimental studies

Chemical substance	Properties	Formula	CAS
Iron(III) sulphate hydrate	399.88 g/mol, 97%	$Fe_2(SO_4)_3 \bullet xH_2O$	15244-10-7
Iron(III) chloride hexahydrate	270.30 g/mol	$FeCl_3 \bullet 6H_2O$	10025-77-1
Iron(III) nitrate nonahydrate	404.00 g/mol, ≥98%	$Fe(NO_3)_3 \bullet 9H_2O$	7782-61-8
Mercury(II) sulphate	296.65 g/mol, ≥99%	$HgSO_4$	7783-35-9
Potassium thiocyanate (fixanal)	0.1 mol/l	KSCN	333-20-0
Sulphuric acid	98.03 g/mol 1.84 kg/dm^3	H_2SO_4	7664-93-9
Hydrochloric acid	36.46 g/mol 1.18 kg/dm^3	HCl	7647-01-0
Nitric acid	63.01 g/mol 1.39 kg/dm^3	HNO_3	7697-37-2
Deuterium oxide	99.8%	D_2O	7789-20-0
Potassium sulphate	174.26 g/mol, ≥99%	K_2SO_4	7778-80-5

3.2.2. Procedures

3.2.2.1. Raman spectroscopic analysis

The working solutions of $[Fe(NCS)_n]^{3-n}$, where n = 1–6, mixtures (the overall complexation reaction can be defined as Eq. (1) [80]), in the level of 10^{-1} M were prepared by mixing the stock solutions of iron(III) salts ($Fe_2(SO_4)_3$, $FeCl_3$) and KSCN. The working solution of $[Fe(NCS)]^{2+}$, in the level of 10^{-1} M, was prepared by mixing the stock solution of $Fe(NO_3)_3$ and KSCN. For the dilution to a required volume distilled water was used. The pH of aqueous working solutions was adjusted to ~ 2 ± 0.1 by controlled addition of sulphuric acid, hydrochloric or nitric acid, respectively.

$$Fe^{3+}(aq) + nSCN^-(aq) \rightarrow \left[Fe(SCN)_n\right]^{(3-n)}(aq) \tag{1}$$

For isotopic exchange analysis the working solutions of $[Fe(NCS)_n]^{3-n}$ (where n = 1–6) mixtures, at the same concentration level, were prepared from the stock solutions of $Fe_2(SO_4)_3$ and KSCN using the D_2O as a solvent. The pH of deuterated aqueous $[Fe(NCS)_n]^{3-n}$ working solutions was adjusted to ~ 1.6 ± 0.1, because pD ≈ pH read + 0.44 ≈ 2.04 ± 0.1 [179].

Additionally, two working solutions of $[Fe(NCS)]^{2+}$ mixtures by mixing the stock solutions of $Fe_2(SO_4)_3$ and KSCN with pH and pD values $\sim 0.7 \pm 0.1$ (in distilled water) and 0.3 ± 0.1 (in heavy water), respectively, were prepared. The pH and pD of these mixtures was adjusted by controlled addition of sulphuric acid.

For Raman spectra subtraction analysis the working solution of K_2SO_4, in the level of 10^{-1} M was prepared. The pH of aqueous working solution was adjusted to $\sim 0.7 \pm 0.1$ by controlled addition of sulphuric acid.

The solutions of $[Hg(SCN)_3]^-$, $[Hg(SCN)_4]^{2-}$ complexes, both in the level of 10^{-2} M, and the solution of $Hg(SCN)_2$, in the level of 10^{-3} M (the overall complexation reaction can be defined as Eq. (2) [180]), were prepared by mixing the necessary volumes of stock solutions of $HgSO_4$ and KSCN. Distilled water for the dilution of mixtures to a required volume was used.

$$Hg^{2+}(aq) + nSCN^-(aq) \rightarrow \left[Hg(SCN)_n\right]^{(2-n)}(aq) \qquad (2)$$

For isotopic exchange analysis heavy water was used as a solvent for the preparation of $Hg(SCN)_2$, $[Hg(SCN)_3]^-$ and $[Hg(SCN)_4]^{2-}$ solutions, at the same concentration level.

The properties of all prepared solutions for experimental Raman spectroscopic analysis are shown in Table 3.2.

Table 3.2. Properties of solutions used for experimental Raman spectroscopic analysis

Solutions	Solvent	pH	pD	Salt	Acid	Concentration, M
$[Fe(NCS)_n]^{3-n}$ (where n = 1–6)	H_2O	~ 2	–	$Fe_2(SO_4)_3$	H_2SO_4	10^{-1}
$[Fe(NCS)_n]^{3-n}$ (where n = 1–6)	H_2O	~ 2	–	$FeCl_3$	HCl	10^{-1}
$[Fe(NCS)]^{2+}$	H_2O	~ 2	–	$Fe(NO_3)_3$	HNO_3	10^{-1}
$[Fe(NCS)_n]^{3-n}$ (where n = 1–6)	D_2O	–	$\sim 1{,}6$	$Fe_2(SO_4)_3$	H_2SO_4	10^{-1}
$[Fe(NCS)]^{2+}$	H_2O	$\sim 0{,}7$	–	$Fe_2(SO_4)_3$	H_2SO_4	10^{-1}
$[Fe(NCS)]^{2+}$	D_2O	–	$\sim 0{,}3$	$Fe_2(SO_4)_3$	H_2SO_4	10^{-1}
K_2SO_4	H_2O	$\sim 0{,}7$	–	K_2SO_4	H_2SO_4	10^{-1}
$[Hg(SCN)_3]^-$ and $[Hg(SCN)_4]^{2-}$	H_2O	~ 2	–	$HgSO_4$	H_2SO_4	10^{-2}
$[Hg(SCN)_3]^-$ and $[Hg(SCN)_4]^{2-}$	D_2O	–	$\sim 1{,}6$	$HgSO_4$	H_2SO_4	10^{-2}
$Hg(SCN)_2$	H_2O	~ 2	–	$HgSO_4$	H_2SO_4	10^{-3}
$Hg(SCN)_2$	D_2O	–	$\sim 1{,}6$	$HgSO_4$	H_2SO_4	10^{-3}

3.2.2.2. UV-Vis spectroscopic analysis

The solution of $[Fe(NCS)]^{2+}$ complex with the metal(III)-ligand molar ratio of 1 : 1, all in the level of 10^{-4} M, was prepared by mixing the necessary volumes of the stock solutions of $Fe_2(SO_4)_3$ and KSCN. Distilled water for the dilution of mixture to a known volume was used. The pH of aqueous working solution was adjusted to ~ 2 ± 0.1 by controlled addition of sulphuric acid.

The solutions of $[Hg(SCN)_n]^{2-n}$ complexes with the metal(II)-ligand molar ratios of 1 : 2, 1 : 3 and 1 : 4, all in the level of 10^{-4} M, were prepared by mixing the necessary volumes of the stock solutions of $HgSO_4$ and KSCN. Distilled water for the dilution of mixtures to a known volume was used.

The properties of all prepared solutions for experimental UV-Vis spectroscopic analysis are shown in Table 3.3.

Table 3.3. Properties of solutions used for experimental UV-Vis spectroscopic analysis

Solutions	Solvent	pH	pD	Salt	Acid	Concentration, M
$[Fe(NCS)]^{2+}$	H_2O	~ 2	–	$Fe_2(SO_4)_3$	H_2SO_4	10^{-4}
$[Hg(SCN)_n]^{2-n}$ (where n = 2–4)	H_2O	~ 2	–	$HgSO_4$	H_2SO_4	10^{-4}

4. RESULTS

It is well known that iron(III) and mercury(II) salts are pH dependent. At least at neutral pH of solution, these salts are prone to hydrolyze. For that reason in analytical procedures, such as mercury or chloride determination, the pH of experimental aqueous solutions is acidic [13, 14]. In the acidic aqueous solutions the ionic compounds such as H^+ ion and certain anions (SO_4^{2-}, Cl^-, and etc.) are present. The anions are potential species being introduced as additional ligands in the complex formation processes. Based on this aspect, the acidic aqueous solutions (pH ~ 2) of iron(III) and mercury(II) thiocyanates, acidified with H_2SO_4 acid, are analyzed in this study.

This chapter is divided into two main parts: investigations of iron(III) and mercury(II) thiocyanates by means of theoretical and experimental studies.

The characterization of iron(III) isothiocyanates ($[Fe(NCS)_n]^{3-n}$, where n = 1–6) includes:

1. analysis of ligand binding in the presence of different additional anions (Cl^-, NO_3^-, SO_4^{2-}) by means of Raman spectroscopy;
2. assignments of fundamental vibrational modes of iron(III) isothiocyanates presented in the aqueous solution of sulphuric acid. Assignments are based on the analysis of experimental and calculated Raman spectra;
3. analysis of the performance of different methods and different classes of functionals used for the geometry optimization and calculation of the UV-Vis spectra of iron(III) monoisothiocyanate ($[Fe(NCS)]^{2+}$), respectively. Additionally, the nature of the excited states of $[Fe(NCS)]^{2+}$ is determined.

The characterization of mercury(II) thiocyanates ($[Hg(SCN)_n]^{2-n}$, where n = 2–4) includes:

1. assignments of fundamental vibrational modes of mercury(II) thiocyanates presented in the aqueous solution of sulphuric acid. Assignments are based on the analysis of experimental and calculated Raman spectra;
2. analysis of the performance of different classes of functionals used for the calculation of the UV-Vis spectra.

4.1. Spectroscopic and structural investigations of iron(III) isothiocyanates. A comparative theoretical and experimental study

4.1.1. Ligand binding analysis

Contribution of ligands to the structure and stability of metal complexes may differ substantially depending on the nature of anions and metal ions. Vibrational spectroscopy provides the unique insight into the ligand binding, because the parameters of vibrational bands depend on the ligand binding mode and interaction strength [181–183]. Here the results of experimental Raman spectroscopic analysis

50

on the vibrational band changes of iron(III) monoisothiocyanate influenced by the use of different additional anions (Cl^-, NO_3^-, SO_4^{2-}) are presented.

4.1.1.1. The anion effect on the Raman spectra

All characteristic vibrational assignments for the three analyzed additional anions are gathered in the Table 4.1. Experimentally determined $\nu C=N$ and $\delta N=C=S$ values are in good agreement with the values for isothiocyanates (in the range of 2150–1990 cm^{-1} and 490–450 cm^{-1}, respectively) listed in the literature [150]. Since the broad or low-intensity peaks in Raman spectra were obtained, the assignments of $\nu C=S$ and $\nu Fe–N$ vibrations were difficult except the solution with NO_3^- ion. Moreover, assignments of frequencies observed in the range of 310–220 cm^{-1} are complicated, because of the possible mixing of $\nu Fe–N$ and $\nu Fe–O$ vibrations in this region. The $\nu C=S$ vibration was clarified by recording Raman spectra of complexes with higher coordination number. Moreover, the $\nu Fe–N$ frequencies were identified, assuming that the emerging band with the stable peak at 295 cm^{-1} for the $[Fe(NCS)_6]^{3-}$ complex cannot be associated to Fe–O vibrations. Experiments conducted with the added different additional anions resulted in the changes of $\nu C=N$ vibrations by 2–11 cm^{-1}. This indicates that formed complex results from the metal-ligand interaction with participation of both SCN^- and additional anion (Table 4.1). Changes of other vibrations were also observed, but they were less substantial comparing with the $\nu C=N$ vibration.

Table 4.1. Characteristic vibrational assignments of iron(III) monoisothiocyanate depending on the additional anion presented

Anions	Assignments, cm^{-1}			
	$\nu C=N$	$\nu C=S$	$\delta N=C=S$	$\nu Fe–N$
Cl^-	2065	750[a]	440	296[a]
NO_3^-	2056	749	445	306
SO_4^{2-}	2067	750[a]	446	295[a]

[a] determined in complexes with higher CN

Abbreviations: ν – stretching, δ – deformation

Initial data on the ligand binding were followed by the detailed vibrational assignments of fundamental vibrational modes of the iron(III) monoisothiocyanate. It is known that at the pH values of about 2, the sulphate (SO_4^{2-}) ions are the main species, while hydrogen sulphate (HSO_4^-) ions might be found in the small amount [184]. Based on the previous findings on metal-ligand interaction, the presence of frequencies of the bound SO_4^{2-} ion in iron(III) isothiocyanate complex was assumed. Moreover, the presence of peaks related to the free SO_4^{2-} and HSO_4^- ion was not discounted. In the view of these facts, the assignments of fundamental vibrational modes of the $[Fe(NCS)]^{2+}$ complex were carried out using the Raman spectra subtraction analysis supplemented by the experiments of isotopic H_2O/D_2O substitution (Fig. 4.1, Table 4.2).

51
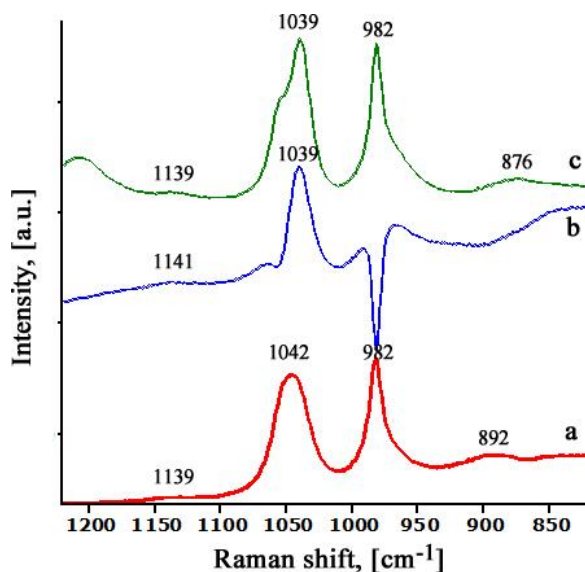
Figure 4.1. Comparison of difference spectra obtained by subtractions in the 1200–850 cm^{-1} region: **a** – the spectrum of aqueous 0.33 M [Fe(NCS)]$^{2+}$ solution, **b** – difference spectrum obtained by subtracting the spectrum of acidified K$_2$SO$_4$ solution (pH ~0.7) from the spectrum of aqueous 0.33 M [Fe(NCS)]$^{2+}$ solution, **c** – the spectrum of deuterated aqueous 0.33 M [Fe(NCS)]$^{2+}$ solution

Table 4.2. Main vibrational band assignments of $[Fe(NCS)]^{2+}$ (acidified with sulphuric acid) according to Raman spectra subtraction procedure in the entire 2100–200 cm^{-1} region

Case	Analyzed spectra	Assignments, cm^{-1}							
		νC=N	ν_{as}S=O* (bound SO$_4^{2-}$)	νS=O (free HSO$_4^-$)	ν_sS=O** (bound SO$_4^{2-}$)	ν_sS=O (free SO$_4^{2-}$)	νC=S	δN=C=S	νFe–N
Case 1	0.33 M [Fe(NCS)]$^{2+}$ pH ~ 2	2067 s	1139 w, b	1042 s		982 s	750 vw	446 m	—
Case 2	0.33 M [Fe(NCS)]$^{2+}$ pH ~ 2 (subtracted spectra of H$_2$O)	2067 s	1139 w, b	1042 s		982 s	750 vw	446 m	—
Case 3	0.33 M [Fe(NCS)]$^{2+}$ pH ~ 2 (subtracted spectra of acidified K$_2$SO$_4$ solution (pH ~ 0.7))	2067 s	1141 w, b	—	1039 s	982 s	750 vw	448 m	—
Literature data		2150─1990 [150]	1142─1148 [185]	around 1047 [186, 187]	1007─1011 [185]	980 [186]		490─450 [150]	220─520 M─ligand [188, 189]

Abbreviations used: s – strong, m – medium, vw – very weak, b – broadband
*assignment made according to PED analysis
** assignment made according to PED analysis

For the Case 1 (Table 4.2) main vibrational bands in the recorded spectrum were assigned. Each assignment of the vibrational band is based on the literature data, performed DFT calculations, and PED analysis which will be discussed in the following section. Raman spectrum of pure complex without the potential water overlapping (Case 2) was obtained after subtraction of water spectrum from the one obtained in Case 1. More complete information was obtained from the subtraction of spectra of the acidified K_2SO_4 solution at the pH ~ 0.7 (Table 4.2 – Case 3 and Fig. 4.1 – ***b*** *spectra*). It allowed to ascertain the νC=S vibration due to increased intensity of the band and discern the vibrational mode of bound SO_4^{2-} ion. As shown in Figure 4.1, it is obvious that the bands at 1053 cm^{-1}, 982 cm^{-1} and 892 cm^{-1} have disappeared and the band at 1039 cm^{-1} became narrower comparing with the band in the *spectrum **a***. The absence of peaks specifies the presence of signals from free SO_4^{2-} and HSO_4^{-} ions. Based on this and literature data [186, 187], the clear peak at 982 cm^{-1} was assigned to the ν_sS=O vibration of free SO_4^{2-} ion. The peaks at 892 cm^{-1} and 1053 cm^{-1} were attributed to the fundamental vibrations of free HSO_4^{-} ion (ν_sS=O). This assignment is based on the cavity formed in the ***b*** *spectrum* in the 940–840 cm^{-1} region and the shift of peak to the higher frequencies in the ***c*** *spectrum* in D_2O experiment. The results of performed subtractions imply that the peak positioned at 1039 cm^{-1} (***b*** *spectrum*) corresponds to the specific symmetric stretching mode of bound SO_4^{2-} ions (due to remained signal). This assumption was affirmed by the H_2O/D_2O exchange experiment (Fig. 4.1 – ***c*** *spectra*). The difference *spectrum **c*** shows a stable position of main peak at 1039 cm^{-1} and the shift of weak shoulder at 1057 cm^{-1} (vibrational mode of free DSO_4^{-} ion). These accurate assignments were made using the Gaussian fitting. As shown in Figure 4.1, the weak and broad, but observable peak at 1139 cm^{-1} remained after subtractions in the *difference spectra **a** and **c***. The absence of changes indicates that the peak belongs to the vibration which is not sensitive to H_2O/D_2O exchange experiment. Based on this and literature data [185], also on PED analysis (Annexes 1 and 2), it can be affirmed, that the peak at 1139 cm^{-1} refers to the asymmetrical stretching mode of bound SO_4^{2-} ion. Besides, according to Myhre *et. al.* [186], the low intensity band of asymmetrical vibration of the free SO_4^{2-} ion exists at 1122 cm^{-1}. For this reason the Raman spectrum subtraction in the Case 3 (Table 4.2) gave adjusted assignment of the bound SO_4^{2-} ion. The small shift from 1139 cm^{-1} (*difference spectra **a, c***) to 1141 cm^{-1} (*difference spectrum **b***) was obtained.

The comparison of literature data and experimentally observed Raman spectra revealed other important finding. According to the well-known spectroscopic data [150], the twisting, rocking and wagging vibrational modes of bound water molecules are found in the 880–530 cm^{-1} region and cannot occur in lattice water molecules. Additionally, the M–O stretching or bending vibrations can be detected at wavenumbers lower than the 900 cm^{-1}. The experimental and calculated Raman spectra obtained in this work showed Raman active bands in the mentioned spectral region. These results confirm the presence of M–O(H_2O) bond in the investigated iron(III) monoisothiocyanate complex. In order to clarify the assumption of bound H_2O molecules, the experiments with isotopically substituted H_2O/D_2O molecules

54

along with Raman spectra subtraction analysis were performed. The obtained difference spectra are shown in Figure 4.2.
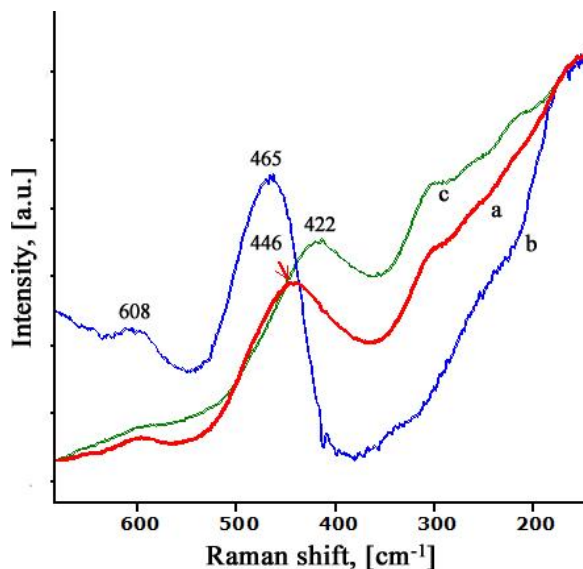
Figure 4.2. Comparison of aqueous solution Raman spectrum and difference spectra obtained by subtractions in the 650–200 cm^{-1} region: **a** – the spectrum of aqueous 0.33 M [Fe(NCS)]$^{2+}$ solution, **b** – difference spectrum obtained by subtracting the spectrum of deuterated aqueous 0.33 M [Fe(NCS)]$^{2+}$ solution from the spectrum of aqueous 0.33 M [Fe(NCS)]$^{2+}$, **c** – difference spectrum of (a – b)

It is obvious that the main stable band with the peak maximum at 608 cm^{-1} (in all obtained spectra) falls in the 880–530 cm^{-1} region, which is inherent to vibrational modes of the bound H$_2$O. Other important assignments encompass the 500–400 cm^{-1} region. The spectrum of [Fe(NCS)]$^{2+}$ solution (*spectrum a*) displayed a broad peak in this region and an overlapping of signals was considered. In order to ascertain the nature of mentioned band, the valuable information was obtained from the difference *spectrum b* (Fig. 4.2). The background subtraction allowed to obtain the Raman band arising from the bound water molecules. As a result, the shifted and narrower peak (due to the effect of D$_2$O) was obtained near 465 cm^{-1} and assigned to the bound H$_2$O vibrations. This assignment was supported by PED analysis (Annexes 1 and 2), where the band of bound H$_2$O molecules in the range of 454–420 cm^{-1} and 463–409 cm^{-1} by B3LYP and PBE1PBE, respectively, was presented. The subtraction of signals of the bound H$_2$O molecules (Fig. 4.2 difference *spectrum c*) enabled for the detection of the adjacent frequencies originated from the deformation vibrations of the NCS$^-$ group with the peak maximum at 422 cm^{-1}. Additionally, this subtraction exposed Raman signals related with the mixing of Fe–N and Fe–O(SO$_4$) vibrations in the 300–200 cm^{-1} region. A merged band profiles were observed in each Raman spectra in the 300–210 cm^{-1} region (Fig. 4.2 *a, b, c spectra*), but the peak positions were not clearly separated. However, literature data [188, 189] and

the performed calculations suggest that M–O and M–N vibrations are expected to be observed in the mentioned spectral region. All the data imply the presence of bound water molecules in the explored complex and allow to assign their vibrational motions correctly.

In summary, the performed initial experiments (isotopic substitution, spectra subtraction) and comparison with literature data allowed the characterization of the reliable structure of iron(III) monoisothiocyanate. In the next chapter, a detailed insight into the approximately elucidated structure and vibrational modes of the $[Fe(NCS)]^{2+}$ complex is provided based on the comparison of experimental and theoretical study followed by PED analysis.

4.1.2. Structure modeling and Raman spectra of $[Fe(NCS)]^{2+}$ complex in the aqueous solution

4.1.2.1. Geometry optimization

In order to determine the most reliable structure of the $[Fe(NCS)]^{2+}$ complex in aqueous solution in the presence of SO_4^{2-} ligand, the geometry optimizations of the $[Fe(NCS)]^{2+}$ complex were performed using different SO_4^{2-} ligand position in the complex. Additionally, the structural changes of complex influenced by different solvation models (hypothetical cases): with explicit (the water molecules are placed around the simulated solute molecule) or explicit and implicit (the solvation effects are calculated by extra terms of the force fields) water molecules in the first coordination shell were evaluated. The optimized structures of each examined hypothetical case along with the calculated bond distances by B3LYP and PBE1PBE methods are shown in Figures 4.3 and 4.4, respectively.
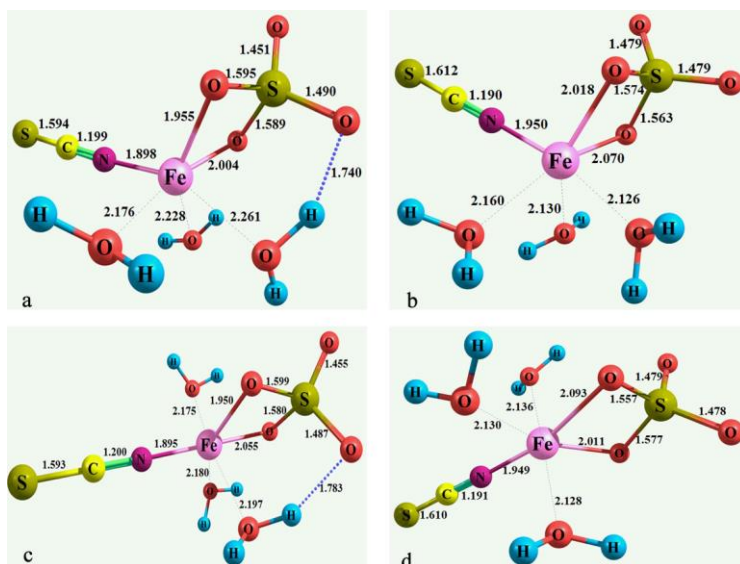
Figure 4.3. Energy-minimized structures of [Fe(NCS)]$^{2+}$ complex using B3LYP method. **a** [Fe(NCS)]$^{2+}$ explicitly solvated, with SO$_4^{2-}$ ligand beside the NCS$^-$ ligand, **b** [Fe(NCS)]$^{2+}$ explicitly-implicitly solvated, with SO$_4^{2-}$ ligand beside the NCS$^-$ ligand, **c** [Fe(NCS)]$^{2+}$ explicitly solvated, with SO$_4^{2-}$ ligand on the opposite of the NCS$^-$ ligand, **d** [Fe(NCS)]$^{2+}$ explicitly-implicitly solvated, with SO$_4^{2-}$ ligand on the opposite of the NCS$^-$ ligand
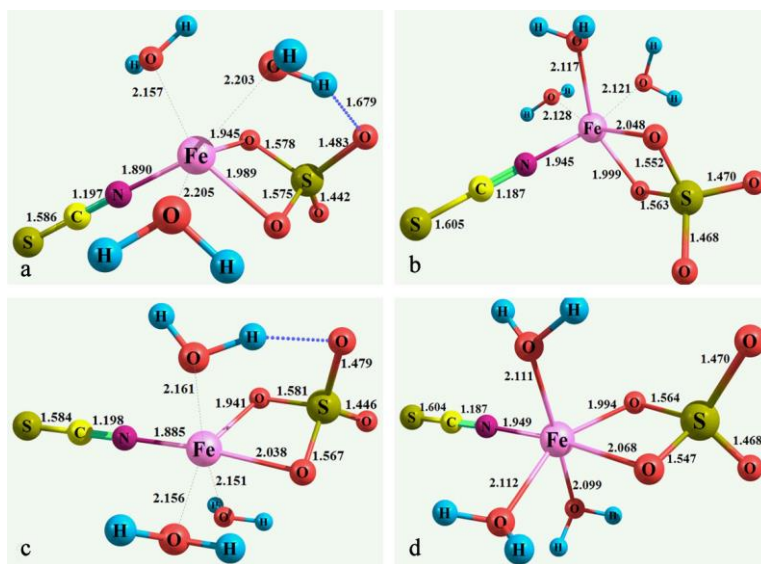
Figure 4.4. Energy-minimized structures of [Fe(NCS)]$^{2+}$ complex using PBE1PBE method. **a** [Fe(NCS)]$^{2+}$ explicitly solvated, with SO$_4^{2-}$ ligand beside the NCS$^-$ ligand, **b** [Fe(NCS)]$^{2+}$ explicitly-implicitly solvated, with SO$_4^{2-}$ ligand beside the NCS$^-$ ligand, **c** [Fe(NCS)]$^{2+}$ explicitly solvated, with SO$_4^{2-}$ ligand on the opposite of the NCS$^-$ ligand, **d** [Fe(NCS)]$^{2+}$ explicitly-implicitly solvated, with SO$_4^{2-}$ ligand on the opposite of the NCS$^-$ ligand

57

To date there are no published studies concerning the structure of titled complex. Results of the optimization studies show the shortening of Fe–N (slightly), Fe–2O(SO$_4$), and Fe–3O(H$_2$O) bonds when the SO$_4^{2-}$ ligand is on the opposite site of the NCS$^-$ ligand (Fig. 4.3). Besides, it is clear that the Fe–2O(SO$_4$) bonds are influenced unequally. The other bond distances such as C=N, C=S, and S=O were almost not influenced by the arrangement of SO$_4^{2-}$ ligand. The same tendency was observed on the energy-minimized structures using the PBE1PBE method (Fig. 4.4). More detailed data on the bond length and angle of the examined complex along with literature data are listed in Table 4.3.

Table 4.3. Selected bond lengths (Å) and angles (°) for the [Fe(NCS)]$^{2+}$ complex in different hypothetical cases using B3LYP and PBE1PBE methods: **1** - [Fe(NCS)]$^{2+}$ explicitly solvated, with SO$_4^{2-}$ ligand beside NCS$^-$ ligand, **2** - [Fe(NCS)]$^{2+}$ explicitly-implicitly solvated, with SO$_4^{2-}$ ligand beside NCS$^-$ ligand, **3** - [Fe(NCS)]$^{2+}$ explicitly solvated, with SO$_4^{2-}$ ligand on the opposite of NCS$^-$ ligand, **4** - [Fe(NCS)]$^{2+}$ explicitly-implicitly solvated, with SO$_4^{2-}$ ligand on the opposite of NCS$^-$ ligand

	Complex								Literature data
	B3LYP				PBE1PBE				
	Explicit	Explicit-implicit	Explicit	Explicit-implicit	Explicit	Explicit-implicit	Explicit	Explicit-implicit	
	1	2	3	4	1	2	3	4	
Bond Length, Å									
Fe–N	1.90	1.95	1.90	1.95	1.89	1.95	1.89	1.95	2.03 [191], [*]1.97 [78]
[*]Fe–O(SO)$_4$	1.98	2.05	2.01	2.05	1.97	2.03	1.99	2.03	1.94 [192], [*]2.01 [193]
[*]Fe–O(H$_2$O)	2.22	2.14	2.19	2.13	2.19	2.12	2.16	2.11	[*]2.01 [194], [**]2.27 [195]
N=C	1.20	1.19	1.20	1.19	1.20	1.19	1.20	1.19	1.15 [191], [*]1.17 [78]
C=S	1.59	1.61	1.59	1.61	1.59	1.61	1.58	1.60	1.63 [191], [*]1.62 [78]
Angles, °									
Fe–N=C	176.0	177.6	178.6	176.9	176.7	179.2	178.8	177.4	176.0 [191], [*]177.2 [78]
N=C=S	179.5	179.8	179.9	179.9	179.5	179.9	179.9	179.9	179.6 [191], [*]178.9 [78]

[*] Average value
[**] Calculated value

Calculated Fe–N bond distances are shorter by 0.02–0.14 Å compared with the found experimental values. It should be noted that all values of experimentally determined bond distances taken from literature are determined for crystal structures mostly having an organic part. Nevertheless, it is clear that explicit-implicit

solvation induces elongation of bond between Fe and N atoms compared with explicitly solvated complex. Calculated length of Fe–O(SO$_4$) and Fe–O(H$_2$O) bonds of each optimized structure is in the range of experimentally identified bond length given by other authors (Table 4.3). Comparing the calculated Fe–O bond distances it was observed that different solvation models cause the opposite effect on changes of Fe–O(SO$_4$) and Fe–O(H$_2$O) bonds. The Fe–O(SO$_4$) bond becomes weaker when the explicit-implicit solvation is used, while the Fe–O(H$_2$O) bond always experiences bond strengthening. The tendency is the same for N=C and C=S bonds. The explicit-implicit solvation slightly strengthens N=C bond, while the C=S bond is slightly weakened. Calculated values of N=C and C=S bond distances are close to experimental. Moreover, it can be seen that the calculated Fe–N=C and N=C=S angles correlate well with the listed experimental values. The optimized structure of [Fe(NCS)]$^{2+}$ complex in all hypothetical cases show that the NCS$^-$ ligand is nearly linear. The bond angles of N=C=S in each case also do not fluctuate markedly and are in the range of 179.46–179.94° (by both B3LYP and PBE1PBE calculations). These values agree well with those reported for the Fe-isothiocyanates with coordinated γ-picoline molecules [190]. Additionally, it can be stated that the presence of linear N=C=S group, strong bond between N=C, and weak bond between C=S confirm the high-spin ground state of [Fe(NCS)]$^{2+}$ complex [191].

4.1.2.2. Experimental and calculated Raman spectra and vibrational assignments

Based on the results of ligand binding characteristics discussed in the 4.1.1 section, a comparative experimental and theoretical (DFT calculations) Raman spectroscopic analysis was performed. Detailed vibrational assignments of the iron(III) monoisothiocyanate in both H$_2$O and D$_2$O using B3LYP and PBE1PBE methods are reported in the Annexes 1 and 2, respectively. The assignments of vibrational modes are based on PED analysis. The aim of comparative vibrational analysis was to elucidate the ligand binding character along with the identification of bound ligand and to establish the most reliable SO$_4$$^{2-}$ *vs.* NCS$^-$ ligand position in the titled complex. Regarding to this, the different arrangement of ligands and functionals (B3LYP and PBE1PBE) in DFT calculations were considered. The effects of different solvation models (implicit or explicit) were also evaluated in order to understand how it can improve the accuracy of reproducing the experimental spectra. The named complex consists of 18 atoms and, according to PED, 16 main vibrational modes in each hypothetical case (Annexes 1 and 2). Seven of sixteen vibrational modes belong to the stretching vibrations. All the rest vibrational modes vary between an in-plane and out-of-plane vibrations, except the σ(O=S=O) bending mode, which always corresponds to the in-plane motion. Only in some cases an additional vibrational modes such as σ((SO$_4$)O−Fe−O(H$_2$O)) and γ(N−Fe−2O(SO$_4$)) were identified.

O–H stretching and H–O–H bending modes. Raman active O−H stretching vibrations of the water molecule are in the 3550−3200 cm^{-1} region [150]. The performed PED analysis shows that the asymmetric and symmetric O–H stretching

vibrations are active in the range of 3900–3100 cm^{-1} and 2900–2270 cm^{-1} for H_2O and D_2O experiments, respectively, in each hypothetical case using both B3LYP and PBE1PBE functionals. The symmetric stretching modes of O–H group are expected at the lower wavenumbers. The only in-plane deformation (scissoring mode, 71–94% by PED) of H–O–H group undoubtedly occurs in the range of 1670–1540 cm^{-1} in water environment in all analyzed hypothetical cases. The other trend was observed in the lower wavenumber region. Starting from the 1015 cm^{-1}, the H–O–H group has the out-of-plane deformation (varied wagging or twisting mode) band which is sometimes decoupled and/or coupled with other vibrations. Moreover, these wagging or twisting vibrational motions in the 629–607 cm^{-1} (by B3LYP) and 668–618 cm^{-1} (by PBE1PBE) region originate mainly (up to 90 %) from the bound H_2O molecules. This finding correlates well with the experimentally observed vibrational band at 608 cm^{-1}, which was assigned to the vibrational motion of bound H_2O.

C=N stretching vibrations. Theoretically computed frequencies of the νC=N were found in the range of 2064–2050 cm^{-1} and 2109–2095 cm^{-1} using B3LYP and PBE1PBE functionals, respectively, which were not affected by D_2O experiment. Experimental Raman spectra of the $[Fe(NCS)]^{2+}$ complex gave unexpected results. The peak maximum at 2067 cm^{-1} in H_2O, which shifted to the lower wavenumber by 6 cm^{-1} (peak maximum at 2061 cm^{-1}) *via* H_2O/D_2O exchange experiment was observed. Such results do not correspond neither with the results of performed calculations on the νC=N vibration in H_2O and D_2O nor with the results of performed studies on the mercury(II) thiocyanates described in the 4.3.2 section. Therefore, Raman spectra of the KSCN solution in H_2O and D_2O were analyzed. Experimentally observed values of the νC≡N vibrations in H_2O shifted to the lower wavenumber by 2 cm^{-1} *via* H_2O/D_2O exchange experiment. Calculated Raman signals of the explicitly solvated SCN$^-$ ion also display small shift (1 cm^{-1}) to the lower wavenumber region. On the basis of these data, it was assumed that there is an interaction between the strongly polarized SCN$^-$ group and H_2O molecules. Regarding to this assumption, it was presumed that the polarized NCS$^-$ group interacts with the H_2O molecules in the investigated $[Fe(NCS)]^{2+}$ complex as well, and as a result the shift in D_2O experiment was obtained. Since a simplified complex structure (without added H_2O molecules to the NCS$^-$ ion) in the geometry optimization course was used, the mentioned polarization effect on the νC=N vibration was not estimated. Moreover, the shifts of νC=N vibration in the aqueous and deuterated solutions are inherent not only to the $[Fe(NCS)]^{2+}$ complex, but also to all complexes with higher coordination number (Table 4.4). These results supplement the assumption on the polarization effect. In general, based on literature data [196] the frequency of C=N bond relative to the free SCN$^-$ speaks very much in favor of a coordination *via* N. The experimentally obtained values on νC=N vibration in $[Fe(NCS)]^{2+}$ complex are almost consistent with the experimentally observed νC≡N vibration of the free SCN$^-$ ion.

S=O stretching vibrations of bound SO_4^{2-} ion. Generally, the asymmetric and symmetric νS=O vibrations gave clear bands and oscillations in two different

regions, depending on the used functionals. For the asymmetric motion vibrations in the 1300–1183 cm^{-1} (by B3LYP) and 1350–1234 cm^{-1} (by PBE1PBE) regions were gained. The symmetric movements were active in the 1094–1084 cm^{-1} (by B3LYP) and 1140–1123 cm^{-1} (by PBE1PBE) region. The isotope substitution had no effect on the asymmetric vibrations and the peak shift of the symmetric vibrations sometimes was in the range of error (up to 5 cm^{-1}) depending on the solvation model used. Assignments of the experimental bands for the S=O stretching modes are identified at 1139 cm^{-1} in both H_2O and D_2O for the asymmetric vibrations, and at 1039 cm^{-1} in both H_2O and D_2O for the symmetric vibrations. Experimentally assigned bands correspond well to the calculated Raman spectra using the B3LYP method.

C=S stretching vibrations. The identification of νC=S vibration in the experimental spectra of [Fe(NCS)]$^{2+}$ complex was complicated due to the very weak Raman signal. Weak Raman signal of νC=S vibration of complexes with low coordination number has been observed for the mercury(II) thiocyanates as well (section 4.3.2). It was found that the signal increases with the increasing coordination number of the ligand. Raman spectra analysis of the [Fe(NCS)$_n$]$^{3-n}$ (where n = 2–6) complexes enabled to confirm the νC=S vibrational band centered at 750 cm^{-1} as listed in Table 4.4. The position of peak is stable in all recorded Raman spectra and the band becomes evident due to increasing coordination number. According to the literature data [197] the wavenumber of νC=S vibration should be increased and the wavenumber of νC=N vibration should be decreased in a complex of the isothiocyanate type in comparison to the free thiocyanate ligand. The recorded spectrum of the aqueous free SCN$^-$ ion displayed the νC–S vibrational mode at 751 cm^{-1}. The comparison of experimentally observed values of the νC=N and νC=S vibrations of investigated complex with the free thiocyanate ion indicates that the NCS$^-$ ligand in the titled complex is bound through the N atom. However, compared to the experimental data obtained νC=S oscillations in the calculated Raman spectra were observed in the higher frequency region (in the range of 954–898 cm^{-1} and 978–920 cm^{-1} by used B3LYP and PBE1PBE, respectively). It is assumed that the inaccuracies are associated with the above mentioned insufficient use of the polarization function on the sulphur atom.

920–805 cm^{-1} region. According to PED, the Raman band in this region arises from the νS–O stretching vibration of bound SO_4^{2-} ion (usually between 70–80%) as shown in the Annexes 1 and 2. This vibrational mode is weak in the calculated Raman spectrum and hardly identifiable experimentally. Calculated Raman spectra showed the splitting of this band and corresponded to the weak or medium bands in the spectra in each hypothetical case. Additionally, Raman bands in D_2O exhibited the same values ($\pm$ 3 cm^{-1}). The PED analysis allowed assigning of the vibrational motion properly and making an assumption that the SO_4^{2-} ion is certainly bound to the Fe^{3+} ion.

578–525 cm^{-1} region. The detailed vibrational assignment by PED revealed that the mode identified as an out-of-plane deformation of O−S=2O or O=S−2O vibrations of the bound SO_4^{2-} ion, was found in the wavenumber range from 578

61

cm^{-1} to 525 cm^{-1} by both functionals used for all the cases. The γ(O−S=2O) vibration tends to be situated in the higher wavenumber and the γ(O=S−2O) vibration in the lower wavenumber region. In addition, it was noticed that both these vibrations are the main motions (69–88%) in the case of explicit and implicit solvation model. In the case of explicit water solvation, the γ(O−S=2O) and γ(O=S−2O) vibrations are combined mainly with the wagging mode of H–O–H group. Nevertheless, these out-of-plane motions are weak in both calculated and experimental Raman spectra.

   N=C=S deformation vibrations. As the experimentally obtained results show (Table 4.1), the δN=C=S deformation vibration varied in the experiments when different additional anions were introduced. It was previously discussed and shown in the Figure 4.2 that in the 500–400 cm^{-1} region the complex frequencies of the bound H$_2$O molecules and NCS$^-$ ligand occur (broad bands were observed). In relation with this data, the shift in D$_2$O experiment could be considered and was identified experimentally. The results show that the H$_2$O/D$_2$O isotopic substitution has a substantial impact on the combined δN=C=S and δH–O–H vibrations. The band shifted to the lower wavenumber up to 26 cm^{-1} in D$_2$O compared with the corresponding peak in H$_2$O (Table 4.4). Despite of the shift, the band remained broad, and correct assignment of the δN=C=S vibration could not be accomplished without above mentioned Raman spectra subtraction procedure or PED analysis. PED showed that in the 490–400 cm^{-1} region the adjacent oscillations of bending modes of the H–O–H group (at 454–397 cm^{-1} by B3LYP, and 463–409 cm^{-1} by PBE1PBE, 66–84% and 66–85% PED, respectively) and deformation vibrations of the NCS$^-$ group exist (Annexes 1 and 2). PED analysis in heavy water solution clearly shows that the δN=C=S vibrational mode is mixed with the bound H–O–H bending (twisting) modes, while in water solution the only δN=C=S deformation (usually between 85–96% by B3LYP and 85–100% by PBE1PBE) vibration was identified. Based on PED and subtraction analysis (Fig. 4.2), the band at 422 cm^{-1} was attributed to the N=C=S deformation vibration. Additionally, experimental and calculated assignments of the δN=C=S vibration correspond well with literature data [150] for isothiocyanate complexes.

   Fe–O and Fe–N stretching vibrations (500–200 cm^{-1} region). The most complicated experimental and calculated Raman spectra analysis was in the 500–200 cm^{-1} wavenumber region. According to Malek *et. al.* [189] the frequency region below 500 cm^{-1} provides information on the metal-ligand stretching vibrations. It was found that the increasing coordination number decreases the metal-ligand stretching frequency [198]. The obtained experimental Raman spectra display one clear and broad band in this region, which as previously discussed was attributed to the mixed vibrations of the bound H$_2$O and NCS$^-$ ligand. Assuming that the investigated complex is six-coordinated, the observation of the metal-ligand stretching modes below 350 cm^{-1} is expected [198]. Experimental Raman spectra of the [Fe(NCS)]$^{2+}$ complex in the 350–200 cm^{-1} region were not informative due to the very broad peaks, indicating the overlapping between a numbers of spectra. Considering this fact, the valuable information from PED and experimental Raman spectra of complexes with the increasing number of the coordinating NCS$^-$ ligands

was received. Experimental Raman spectra of the $[Fe(NCS)_6]^{3-}$ displayed the clear peak at 295 cm^{-1}, while it was unclear in the case of $[Fe(NCS)]^{2+}$ complex. It is assumed that the appearance of peak is related with the continuous increase of the Fe–N bond and equivalent decrease of the Fe–O bond number in the explored structure. Further PED analysis revealed that at the 350–200 cm^{-1} wavenumber region, a lot of vibrational motions could take part and the contribution to the normal modes is mainly less than 50% (except the νFe–O, when the O atom participates from the H_2O molecule). Sometimes the νFe–O(H_2O) vibration exceeds 50% and contribution reaches 89% with B3LYP and 84% with PBE1PBE, respectively. It is difficult to compare such mixing of vibrational modes, but some tendency could be observed. PED data represented that the mixing of νFe–O(H_2O) (contribution to the normal mode was mostly more than 50%), νFe–O(SO_4), and Fe–N vibrations in the 350–250 cm^{-1} region is possible. In this region, the symmetric and asymmetric νFe–O(H_2O) vibrations contribute most to the normal mode compared with the other frequencies. Comparing both B3LYP and PBE1PBE methods, it was observed that the νFe–N vibration alone tends to be found in the 370–350 cm^{-1} region for the investigated $[Fe(NCS)]^{2+}$ complex. This assignment correlates quite well with the above mentioned experimentally observed peak at 295 cm^{-1}, taking into account, that it possibly corresponds to the νFe–N vibrations when more than one NCS$^-$ ligand were introduced. The subsequent region at the calculated 240–210 cm^{-1} provided the same mixing of mentioned three vibrational modes, but the contribution of νFe–O(H_2O) frequencies did not exceed 50%.

Based on comparison of calculated and experimental data on the fundamental vibrational assignments (νO–H, νS=O, δH–O–H, νC=N and etc.) of the $[Fe(NCS)]^{2+}$ complex it is assumed that the B3LYP functional is more appropriate for the calculations. Besides, good correlation between the computed and experimentally obtained data confirms the theoretical structure prediction that six-coordinated Fe^{3+} complex with the three different ligands, NCS$^-$ and SO_4^{2-}, and water molecules, is formed. Calculated Raman spectra when the SO_4^{2-} ligand was situated near the NCS$^-$ ligand correspond better to the experimentally recorded spectra. Moreover, the explicit and/or implicit analysis presumably indicates that the explicit and implicit solvation takes part in the aqueous system of the titled complex.

4.1.2.3. Experimental Raman spectra of $[Fe(NCS)_n]^{3-n}$ complexes

Raman spectra of six aqueous solutions with the established molar ratio of the Fe^{3+} and SCN$^-$ ion were obtained. It was noticed that the attachment of each additional NCS$^-$ ligand to the Fe^{3+} ion causes a gradual growth of the intensities of νC=N and νC=S vibrational bands. Moreover, after each NCS$^-$ ligand attachment the bands attributed to the δN=C=S and νFe–N vibrational modes, as well as νC=N and νC=S, became narrower and more evident. All these observations are shown in Figures 4.5–4.7.

Vibrational assignments of the experimental Raman bands of $[Fe(NCS)_n]^{3-n}$ complexes (where n = 1–6) are summarized in the Table 4.4.

Table 4.4. Raman vibrational assignments of experimentally obtained bands for iron(III) isothiocyanates with higher coordination number in acidic aqueous and deuterated aqueous solutions. pH ~ 2 ± 0.1 (acidified with sulphuric acid)

Complex	Main assignments in H_2O (D_2O), cm^{-1}					
	$\nu C{=}N$	bound $\nu_{as}S{=}O$	bound $\nu_{s}S{=}O^{*}$	$\nu C{=}S$	$\delta N{=}C{=}S$	$\nu Fe{-}N$
[Fe(NCS)]$^{2+}$	2067 (2061)	1139 (1139)	1042 (1040)	750 (750)	446; 422* (420)	B**
[Fe(NCS)$_2$]$^{+}$	2063 (2060)	1139 (B)**	1042 (1040)	750 (750)	443; 415* (418)	B**
[Fe(NCS)$_3$]	2063 (2058)	− (−)	1042 (1040)	750 (750)	442; 412* (414)	B** (299)
[Fe(NCS)$_4$]$^{-}$	2063 (2060)	− (−)	1042 (1040)	750 (750)	437; 412* (414)	295 (300)
[Fe(NCS)$_5$]$^{2-}$	2065 (2063)	− (−)	1042 (1040)	750 (750)	439; 413* (411)	295 (300)
[Fe(NCS)$_6$]$^{3-}$	2065 (2063)	− (−)	1042 (1040)	750 (750)	438; 413* (411)	295 (300)

*assignments after subtraction procedures discussed in the section 4.1.1.1
** B refers to the broadband

In the high-frequency region, the strong peaks in the 2067–2063 cm^{-1} and 2063–2058 cm^{-1} region in H_2O and D_2O, respectively, were assigned to the $\nu C{=}N$ vibrational mode. It is obvious that the hydrogen/deuterium exchange leads to the red shifts by 2–6 cm^{-1} of the $\nu C{=}N$ peak of each iron(III) isothiocyanate complex. These results strengthen the previously discussed assumption that the polarization effect should be taken into account. Additionally, it is clear that the $\nu C{=}N$ vibration is sensitive to the number of added NCS^{-} ligands in both H_2O (Fig. 4.5, Table 4.4) and D_2O (Table 4.4) experiments. Moreover, it was found that the increasing number of NCS^{-} ligands in the aqueous solution shifts the $\nu C{=}N$ vibration to the lower wavenumber position as long as the [Fe(NCS)$_3$] complex is formed. It indicates the weakening of C=N bond in the [Fe(NCS)$_3$] complex comparing with the [Fe(NCS)]$^{2+}$ and [Fe(NCS)$_2$]$^{+}$ complexes. Further increase of the NCS^{-} ligand number induces the opposite – blue shift. The trend of the shift is the same in D_2O experiment (Table 4.4). It is supposed that the blue shift indicates the dissociation behavior of the investigated complexes as well as the presence of signal of the free SCN^{-} ion. Such feature of iron(III) isothiocyanates with higher coordination number was described by Ozutsumi et. al. [80].
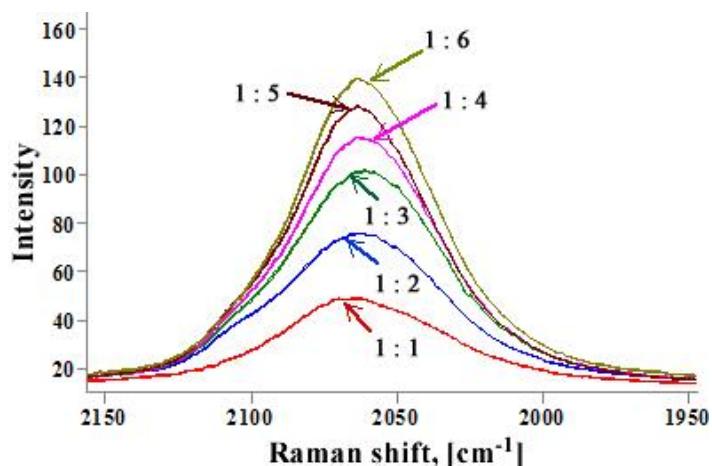
Figure 4.5. Experimentaly observed νC=N stretching vibrational bands in Raman spectra of aqueous $[Fe(NCS)_n]^{3-n}$ solutions, with varying molar ratio of $[Fe^{3+}]$: $[SCN^-]$ from 1 : 1 to 1 : 6
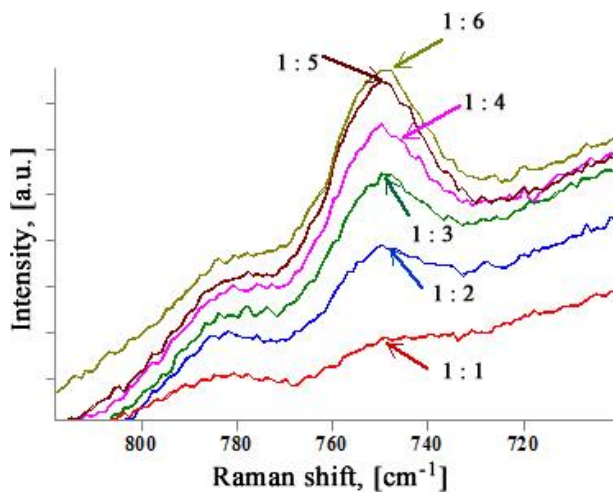
Figure 4.6. Experimentaly observed νC=S stretching vibrational bands in Raman spectra of aqueous $[Fe(NCS)_n]^{3-n}$ solutions, with varying molar ratio of $[Fe^{3+}]$: $[SCN^-]$ from 1 : 1 to 1 : 6
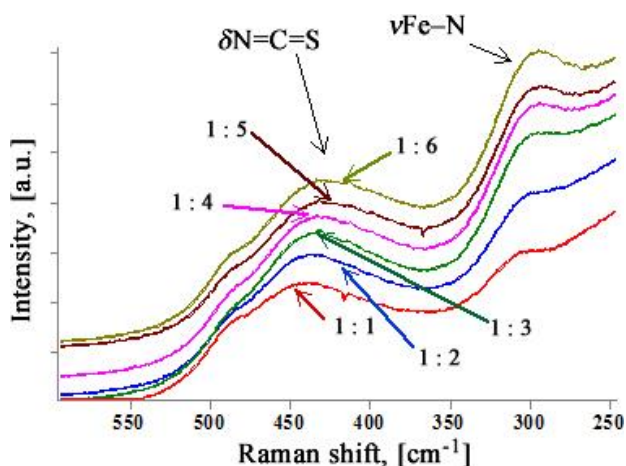
Figure 4.7. Experimentaly observed νFe–N and δN=C=S vibrational bands in Raman spectra of aqueous $[Fe(NCS)_n]^{3-n}$ solutions, with varying molar ratio of $[Fe^{3+}]$: $[SCN^-]$ from 1 : 1 to 1 : 6

Based on experimental results (Table 4.4), it is clear that the weak ν_{as}S=O vibration of the bound SO_4^{2-} is identifiable only in the case of iron(III) monoisothiocyanate. On the contrary, the symmetric νS=O vibrations of the bound SO_4^{2-} at 1042 cm^{-1} and 1040 cm^{-1} in H_2O and D_2O, respectively, were clearly observed in each spectra. The strong signal became weaker with the increasing number of NCS$^-$ ligands, but it did not disappear. Such observation implies that the dissociation of complexes with higher coordination number could take part. Another noticed stable band was assigned to the νC=S vibration, based on previously discussed results. The intensity of this band rises with the increasing number of NCS$^-$ ligands (Fig. 4.6, Table 4.4).

According to the experimental data, the changes in $\Delta\nu$ for the δN=C=S vibration could not be explained properly without the additional data, such as previously mentioned Raman spectra subtraction or PED analysis. This is because the mixing of vibrations of the bound H_2O molecules and δN=C=S occurs and the dissociation of complexes is possible. The assignments of δN=C=S vibration of all $[Fe(NCS)_n]^{3-n}$ complexes were clarified after Raman spectra subtraction procedures (Table 4.4).

Because of the challenges in the detection of Fe–N stretching vibrations in the low-intensity region (the mixing of νFe–O and νFe–N is presented) in experimental Raman spectra, the performed experiments of iron(III) isothiocyanates with higher coordination number, gave valuable results. The stable vibrational band associated with the νFe–N oscillations appeared more prominent with each additional SCN$^-$ ligand in H_2O (Fig. 4.7, Table 4.4) and D_2O (Table 4.4), respectively. The visibility and absence of band shifts allowed assigning of the νFe–N frequencies at 295 cm^{-1} and 300 cm^{-1} in H_2O and D_2O, respectively.

4.2. Theoretical study of electronic absorption spectra of iron(III) monoisothiocyanate

The goal of this part of the work was to perform a research on the molecular structure and electronic excitations of iron(III) monoisothiocyanate presented in the aqueous solution of sulphuric acid by means of theoretical modeling and experimental UV-Vis spectroscopy. The performance of the different classes of functionals on the calculation of the UV-Vis spectra along with different DFT methods used for the geometry optimization was evaluated. Moreover, the effect of different solvation models and different ligand arrangement on the final electronic spectrum was also considered.

The results of performed calculations indicate that TD-PBEPBE approach applied on optimizations using B3LYP, CAM-B3LYP, and PBE1PBE methods is in the worst agreement with experimentally observed spectrum. As far as the visible region is considered, TD-PBEPBE functional experienced a red-shift of main absorption band going up to 30 nm. Furthermore, the second high intensity band in the higher wavelengths region (over 550 nm) appeared which is not reasonable for the experimental one. Moreover, it was found that the effect of explicit and implicit solvation model at the same time does not meet spectral features of experimental spectrum. The calculated maximum in the visible region is usually most intensive peak in the entire spectrum and exhibits the shift to the longer wavelengths (red-shift) compared with experimental one. On the contrary, blue-shifted absorption maximum was usually observed in the UV region. Based on the simulation data it was found that the theoretical absorption spectra when the SO_4^{2-} ligand is on the opposite site of the NCS^- ligand do not correspond to the experimental. In most cases the maximum of main absorption band in the visible region shifts to the longer wavelengths up to 70 nm. Besides, simulated spectra with such ligand arrangement were not able to reproduce spectral features of experimental spectrum in the region below ~ 280 nm. Based on these findings and omitting the results which engendered in quite big discrepancies, more detailed comparison between experimental and calculated electronic spectra when SO_4^{2-} ligand is beside the NCS^- ligand with the explicit solvation model (the complex **1,** Table 4.3) is presented in the following.

In the Figures 4.8–4.10 the experimental UV spectrum together with TD-DFT calculated ones for complex **1** are reported. Experimental spectrum gave one absorption band in the visible region with the maximum at 453 nm. A much greater intense absorption band was observed in the near UV part with the peak maximum at 301 nm (Fig. 4.8). Additionally, experimental spectrum presents an intense band with the shoulder in the region of the spectrum extending from ~ 210 nm to 270 nm with the approximate maximum of 216 nm. Comparing all TD-B3LYP simulated and experimental absorption spectra (Fig. 4.8) with TD-CAM-B3LYP (Fig. 4.9) and TD-PBE1PBE (Fig. 4.10), it is clear that regardless of the method used to optimize geometry the TD-B3LYP functional is in worst agreement with experimental. One can see that the absorption maximum in the visible part is quite red-shifted with the deviation from the experimental maximum of about 25–40 nm (Fig. 4.8). Moreover, this absorption band tends to have a double-peak character with the second peak

maximum in the range of 490–530 nm, which is not characteristic neither for experimental spectrum nor for the TD-CAM-B3LYP and TD-PBE1PBE simulated spectra. If the UV part of the spectra is analyzed, it is clear that this part also does not match with the experimental absorption spectrum.
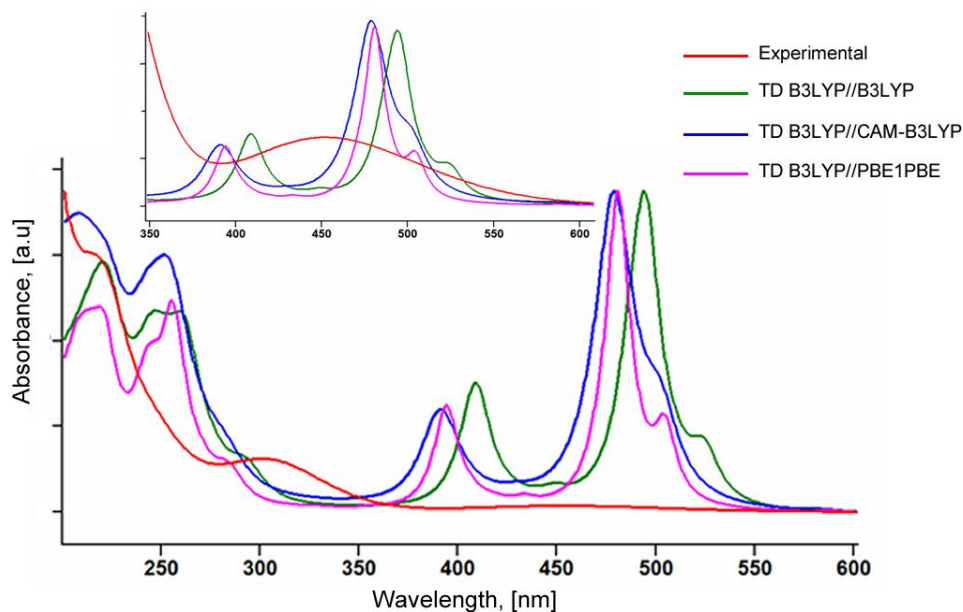
Figure 4.8. Absorption spectra of iron(III) monoisothiocyanate calculated with TD B3LYP functional and different methods for geometry optimization *vs*. the experimental one. Inset shows the magnified view of experimental band in the visible region
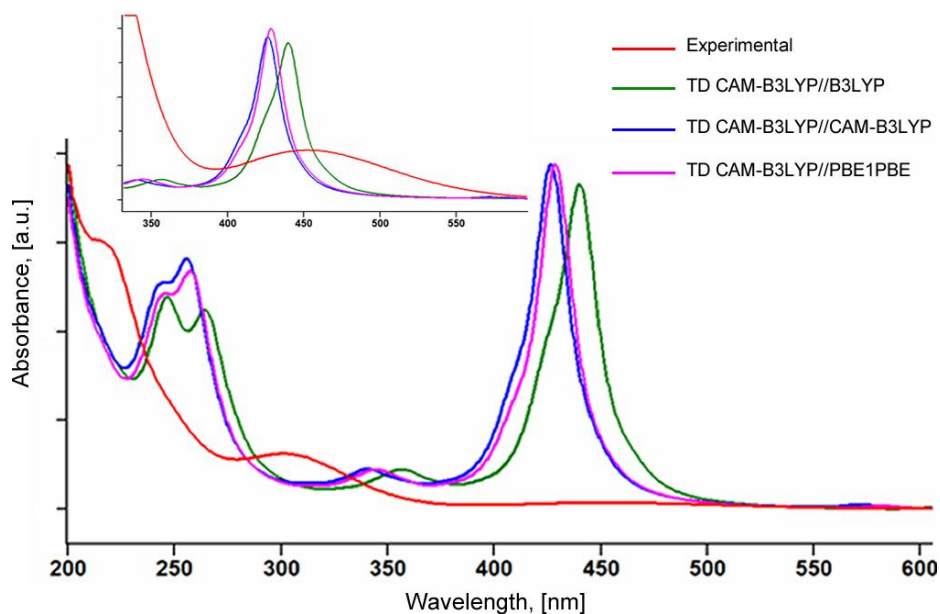
Figure 4.9. Absorption spectra of iron(III) monoisothiocyanate calculated with TD CAM-B3LYP and different methods for geometry optimization *vs.* the experimental one. Inset shows the magnified view of experimental band in the visible region
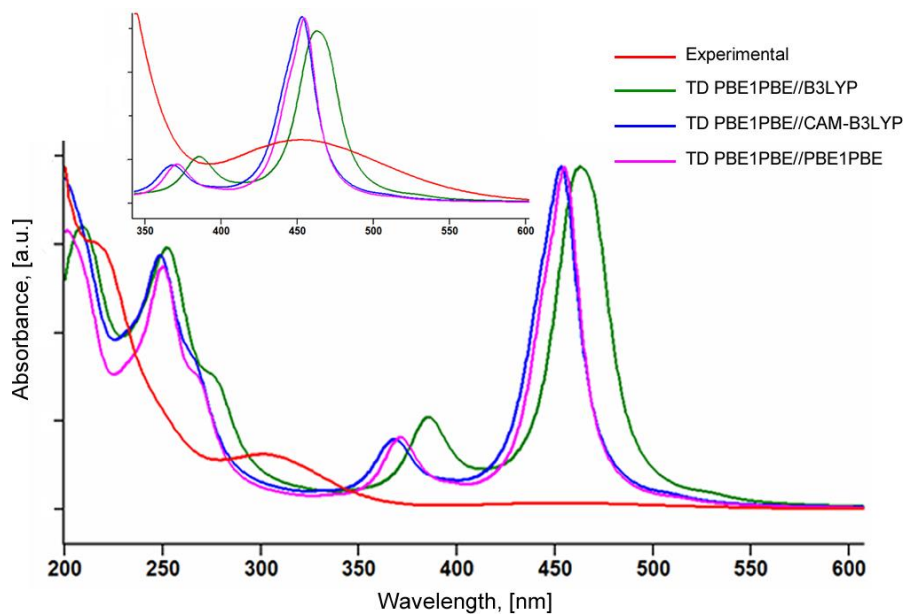
Figure 4.10. Absorption spectra of iron(III) monoisothiocyanate calculated with TD PBE1PBE and different methods for geometry optimization *vs.* the experimental one. Inset shows the magnified view of experimental band in the visible region

The simulated absorption spectrum using TD-CAM-B3LYP approach on all three optimized structures experiences a less pronounced deviation (in the range of 15–25 nm) from the experimental maximum in visible region compared with TD-B3LYP (Fig. 4.9). Unlike the apparent red-shift in the visible part, caused by the used TD-B3LYP functional, the blue-shift using TD-CAM-B3LYP was always identified in the calculated spectra. If the UV region is inspected, it is clear that TD-CAM-B3LYP functional gives absorption bands with a general shape and tendency that are in reasonable agreement with experimental spectrum. Actually, the third TD-PBE1PBE functional used for all analyzed DFT methods is in best agreement with experimentally obtained spectrum, even if the band shape and intensities are less well reproduced (Fig. 4.10). The deviation is 0 nm and 1 nm for CAM-B3LYP and PBE1PBE, respectively, and 10 nm for B3LYP compared with the experimental maximum at 453 nm. It should be noted that all TD-DFT computed absorption spectra (Fig. 4.8–4.10) have relatively higher intensity at the longer wavelengths (low-energy) and relatively lower intensity at the shorter wavelengths (high-energy). That is the opposite of experimentally observed spectral features. Simulated electronic spectra show blue-shifted maximum in the range of 260–280 nm compared with the peak of 301 nm in the experimental spectrum. Nevertheless, the characteristic spectral feature of experimental spectrum in the 200–230 nm could be identified in each TD-PBE1PBE calculated spectra (Fig. 4.10). It is interesting to note that although it was found that explicit-implicit solvation model failed to reproduce the absorption in visible part and lower than 280 nm, it is able correctly reproduce the large and intense experimental band at the 301 nm. In view of that fact, the valuable information was obtained from the excited state analysis. It was found out that the main electronic transition at about 300 nm using explicit-implicit solvation model corresponded to water-to-metal charge transfer. It could be assumed that this transition is sensitive to the implicit solvation environment and as consequence a good compliance with experimentally observed band was obtained.

Generally, it can be assumed that the choice of the functional used for TD calculations is much more important than the choice of the method used for geometry optimization. The PBE1PBE and CAM-B3LYP methods used for geometry optimization gave very similar absorption spectra, while slightly different spectral tendencies using B3LYP were observed.

Analysis of excited states. It was already mentioned in the literature review that electronically excited states are of key importance for photochemistry and for a variety of optical materials applied in the development of new technologies. Hence, the TD-DFT theory emerges as one of the most practical tools that can be used to predict the electronic properties of transition metal complexes. In this section, the nature of the excited states obtained from TD-PBE1PBE calculation using PBE1PBE level of theory since the latter functionals showed a good overall compliance, compared with the experimental $[Fe(NCS)]^{2+}$ spectrum, is described. The wavelengths, singlet states, and molecular orbital (MO) interactions of the most important vertical transitions in terms of oscillator strength (greater than 0.01) are listed in the Table 4.5. The classification in terms of transition character was based

on the composition of the occupied and virtual MOs of the dominant excitation (according to transition coefficients) of the excited state considered for the $[Fe(NCS)]^{2+}$ complex. Some characteristic CTs (charge transfer) are visually shown in Figure 4.11.

Table 4.5. Main electronic transition of the benchmark $[Fe(NCS)]^{2+}$ complex calculated with TD-PBE1PBE//PBE1PBE

Transition	MO interaction*	Transition type	Wavelength, nm	Oscillator strength f
6	HOMO→LUMO	LMCT	455	0.1857
7	HOMO-2→LUMO	LMCT	444	0.0623
17	HOMO-1→LUMO+4	LMCT	372	0.0215
18	HOMO→LUMO+4	LMCT	368	0.0143
27	HOMO-5→LUMO+2	LMCT	270	0.0279
28	HOMO-5→LUMO+2	LMCT	268	0.0168
32	HOMO-7→LUMO+1	LMCT	252	0.0719
34	HOMO-8→LUMO	LMCT	248	0.0338
39	HOMO-5→LUMO+3	LMCT	237	0.0144
41	HOMO-5→LUMO+3	LMCT	232	0.016
56	HOMO-10→LUMO+1	LMCT	212	0.0205
58	HOMO-1→LUMO+6	LLCT	210	0.0268
66	HOMO-13→LUMO	LMCT	202	0.0113
68	HOMO→LUMO+8	LLCT	201	0.0221
71	HOMO-11→LUMO+2	LMCT	200	0.0238

*according to the highest transition coefficient

By analyzing the main electronic transitions summarized in Table 4.5, it was noticed that the visible part of the spectrum refers to two ligand-to-metal charge transfers (LMCT). Obtained transition coefficients for HOMOs (highest occupied molecular orbitals) of transition 6 indicate an extremely important role of the NCS^- ligand where isothiocyanate definitively acts as the principal electron donor group (Fig. 4.11). However, due to the participation of a small number of HOMOs, at the same time the SO_4^{2-} ligand based LMCT transition was also found to contribute. Unlike the transition 6, the second excitation transition in the visible region (transition 7) involves lower-energy occupied MOs which are mainly centered on the SO_4 ligand (Fig. 4.11). Here electrons are donated by all O atoms. Nevertheless, a small contribution from occupied MOs of NCS^- ligand was also fixed. It can be assumed that both NCS^- and SO_4^{2-} ligands are the main ones responsible for appeared absorbance peak in the visible part of UV-Vis spectrum. Based on the obtained results, all low-lying transitions in the near UV region (200–380 nm) were

still characterized as LMCT. It was observed that at the intersection point of visible and near UV wavelengths, the electron donation from NCS$^-$ ligand is prevalent (transitions 17 and 18). At the wavelengths lower than 370 nm the vast majority of HOMOs are essentially orbitals of the SO$_4^{2-}$ ligand with the charge transfer delocalized on metal. Here it should be emphasized that depending on the respective excited state, the additional HOMOs of the H$_2$O and NCS$^-$ ligands were also fixed in the transition. Based on transition coefficients, the pure SO$_4^{2-}$ ligand character highest occupied MOs are presented in the transitions 27 (Fig. 4.11), 28, 39, 41 (Table 4.5). Concerning particular MO involved in these transitions, electrons are transferred from all four or three O atoms of SO$_4^{2-}$ ligand to iron. More diverse electronic transitions were noticed in the range of 200–250 nm. This region exhibits two main absorption peaks. The absorption band at the higher wavelengths encompasses two main transitions – 32 and 34. According to transition coefficients, both these excited states have NCS $\rightarrow$ Fe, SO$_4$ $\rightarrow$ Fe, SO$_4$ and H$_2$O $\rightarrow$ Fe LMCT character. The latter transition is shown visually in Fig. 4.11. However, based on transition coefficients, it can be seen the tendency that both transitions being much more delocalized over the NCS$^-$ ligand. Transitions 56, 66 and 71 are typical for LMCT state (Fig. 4.11 *transition 56 c*), but the contribution of ligand-to-ligand charge transfer (LLCT) was also fixed. Here, the electron transfer from S to C atoms in the NCS$^-$ ligand and from NCS$^-$ ligand to H$_2$O ligand (Fig. 4.11, *transition 56 a and b)* was identified. By analyzing the LMCT state of the transitions 56, 66 and 71 it is clear that the excited electron density is mainly delocalized over the H$_2$O ligand. As far as nearly far UV region is approached, electronic transitions 58 (Fig. 4.11) and 68 were assigned as LLCT transitions, in which electrons are mainly promoted from the NCS-based MO, to the empty MOs of the H$_2$O ligand.

Generally, the excited state analysis enabled to determine which of iron(III) monoisothiocyanate's active substituent is significant contributor to the spectral properties of the complex.
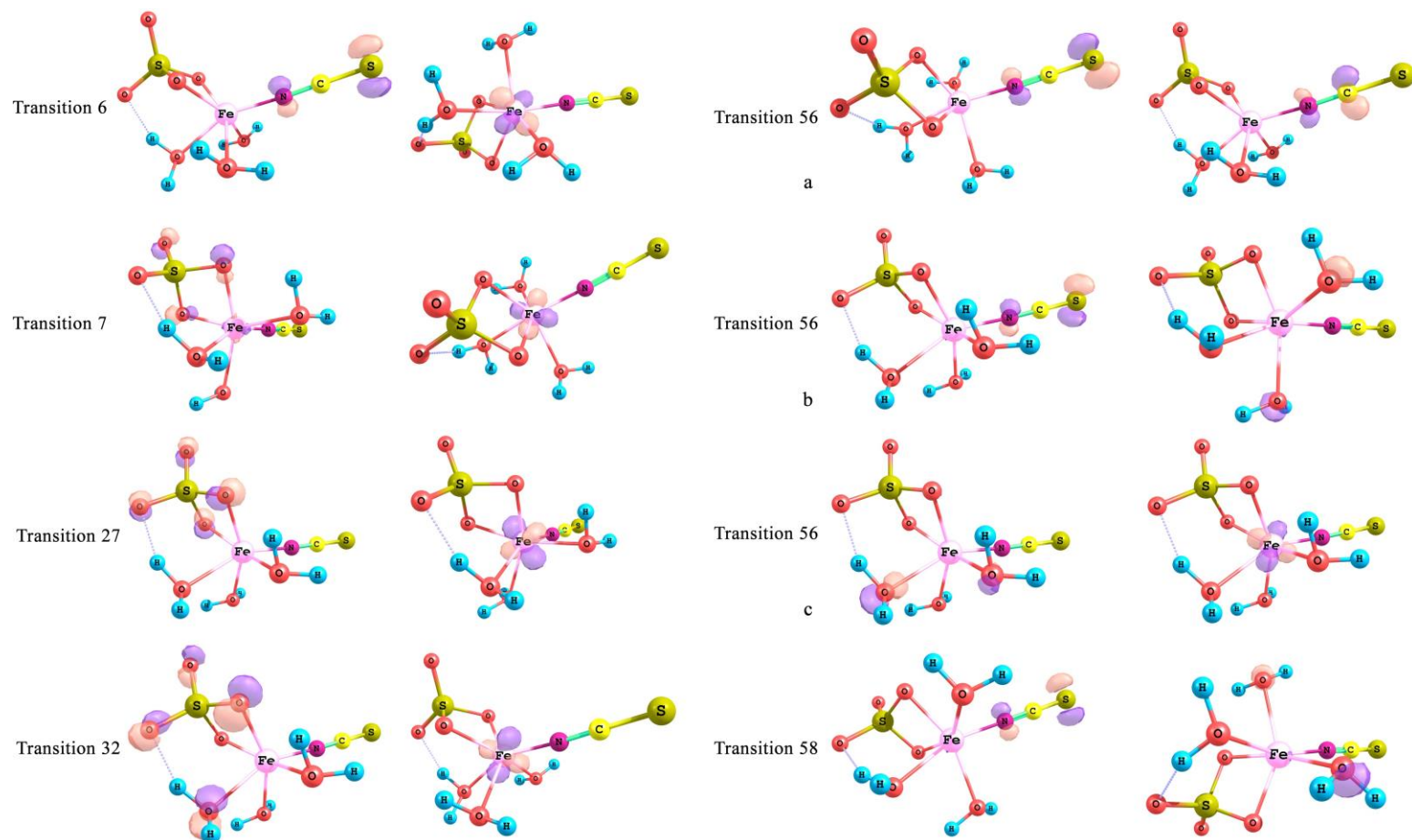
Figure 4.11. The TD-PBE1PBE/PBE1PBE calculated singlet electron transition (illustrations) for selected transitions

Transition 6

Transition 56
a

Transition 7

Transition 56
b

Transition 27

Transition 56
c

Transition 32

Transition 58

4.3. Molecular structure of mercury(II) thiocyanate complexes based on DFT calculations and experimental UV-Vis and Raman spectroscopic studies

4.3.1. Structure modeling of $[Hg(SCN)_n]^{2-n}$ and SCN^-

In order to elucidate the most reliable structure of free SCN^- and $Hg(SCN)_2$, $[Hg(SCN)_3]^-$ and $[Hg(SCN)_4]^{2-}$ complexes in the aqueous solution, the geometry optimizations of each complex using different solvation models (hypothetical cases): with explicit or/and implicit water molecules were performed. All the calculated and experimental structural data of each examined structures are gathered in Table 4.6. The optimized geometry of SCN^- ion with C–S and C≡N bond distances of 1.67 Å and 1.18 Å correlates well with the experimental values from literature (Table 4.6). The differences varying from 0.02 to 0.04 Å may be influenced by the K^+ and NH_4^+ cations present in the sample during experimental analysis by other researches. The optimized structures of $Hg(SCN)_2$, $[Hg(SCN)_3]^-$ and $[Hg(SCN)_4]^{2-}$ complexes in all hypothetical cases take a bent conformation (Fig. 4.12).

Table 4.6. Geometrical parameters and energy of $Hg(SCN)_2$, $[Hg(SCN)_3]^-$, $[Hg(SCN)_4]^{2-}$ complexes in different hypothetical cases

Complex	Bond	Calculated bond lengths (average), Å	Experimental bond lenghts (solvent), Å	Angle	Calculated bond angle (average), °	Experimental bond angle (solvent), °	Energy, kcal/mol	Dipole moment
SCN⁻	C–S	1.67	1.69[a1], 1.63[a2]	S–C≡N	180.0		-308212.7745	1.6562
	C≡N	1.18	1.15[a1], 1.15[a2]					
SCN⁻ solvated	C–S	1.66	1.69[a1], 1.63[a2]	S–C≡N	180		-308271.6987	2.3349
	C≡N	1.18	1.15[a1], 1.15[a2]					
$[(SCN^-)(H_2O)_2]^-$	C–S	1.66	1.69[a1], 1.63[a2]	S–C≡N	178.5		-404193.3402	1.4337
	C≡N	1.17	1.15[a1], 1.15[a2]					
$[(SCN^-)(H_2O)_2]^-$ solvated	C–S	1.66	1.69[a1], 1.63[a2]	S–C≡N	178.5		-404193.3402	1.4334
	C≡N	1.17	1.15[a1], 1.15[a2]					
$Hg(SCN)_2$	Hg–S	2.33	2.41 (DMSO)[b]	S–Hg–S	178.6		-616958.5051	2.7168
	C–S	1.70		Hg–S–C	94.6	107° [b] (DMSO)		
	C≡N	1.16		S–C≡N	178.1			
$Hg(SCN)_2$ solvated	Hg–S	2.46	2.41[b] (DMSO)	S–Hg–S	180.0		-617033.1889	0
	C–S	1.68		Hg–S–C	104.1	107° [b] (DMSO)		
	C≡N	1.17		S–C≡N	176.9			
$Hg(SCN)_2(H_2O)_2$	Hg–S	2.44	2.41[b] (DMSO)	S–Hg–S	138.7		-712957.3253	1.0597
	Hg–O	2.19		S–Hg–O	103.5			
	C–S	1.69		Hg–S–C	90.8	107° [b] (DMSO)		
	C≡N	1.17		O–Hg–O	97.1			
				S–C≡N	175.7			
$Hg(SCN)_2(H_2O)_2$ solvated	Hg–S	2.44	2.41[b] (DMSO)	S–Hg–S	142.6		-712968.8169	0.689
	Hg–O	2.18		S–Hg–O	102.4			
	C–S	1.69		Hg–S–C	93.5	107° [b] (DMSO)		
	C≡N	1.17		O–Hg–O	95.9			

Table 4.6. Continued

Complex	Bond	Calculated bond lengths (average), Å	Experimental bond lenghts (solvent), Å	Angle	Calculated bond angle (average), °	Experimental bond angle (solvent), °	Energy, kcal/mol	Dipole moment
				S–C≡N	178.6			
$[Hg(SCN)_3]^-$	Hg–S	2.43	2.464[b] (DMSO)	S–Hg–S	120.0		-925225.7275	0.0039
	C–S	1.69		Hg–S–C	99.9	107° [b] (DMSO)		
	C≡N	1.16		S–C≡N	176.9			
$[Hg(SCN)_3]^-$ solvated	Hg–S	2.45	2.464[b] (DMSO)	S–Hg–S	120.0		-925268.8072	0.0852
	C–S	1.69		Hg–S–C	98.7	107° [b] (DMSO)		
	C≡N	1.17		S–C≡N	177.6			
$[Hg(SCN)_3(H_2O)]^-$	Hg–S	2.50	2.464[b] (DMSO)	S–Hg–S	114.7		-973220.4722	3.5743
	Hg–O	2.21		S–Hg–O	103.4			
	C–S	1.68		Hg–S–C	96.5	107° [b] (DMSO)		
	C≡N	1.17		S–C≡N	176.7			
$[Hg(SCN)_3(H_2O)]^-$ solvated	Hg–S	2.50	2.464[b] (DMSO)	S–Hg–S	115.9		-973258.1460	7.4747
	Hg–O	2.22		S–Hg–O	101.9			
	C–S	1.68		Hg–S–C	95.8	107° [b] (DMSO)		
	C≡N	1.17		S–C≡N	177.7			
$[Hg(SCN)_4]^{2-}$	Hg–S	2.54	2.531[b1], 2.547[b2] (DMSO), 2.54[c] (water)	S–Hg–S	109.5		-1233413.0032	0.0049
	C–S	1.68		Hg–S–C	106.3	108° [b] (DMSO), 102° [b] (water)		
	C≡N	1.17		S–C≡N	175.8			
$[Hg(SCN)_4]^{2-}$ solvated	Hg–S	2.52	2.531[b1], 2.547[b2] (DMSO), 2.54[c] (water)	S–Hg–S	109.5		-1233553.2590	0.074

Table 4.6. Continued

Complex	Bond	Calculated bond lengths (average), Å	Experimental bond lenghts (solvent), Å	Angle	Calculated bond angle (average), °	Experimental bond angle (solvent), °	Energy, kcal/mol	Dipole moment
	C–S	1.68		Hg–S–C	100.2	108° [b] (DMSO), 102° [b] (water)		
	C≡N	1.17		S–C≡N	177.8			
$[Hg(SCN)_4(H_2O)_2]^{2-}$	Hg–S	2.54	2.531[b1], 2.547[b2] (DMSO), 2.54[c] (water)	S–Hg–S	109.5		-1329394.9234	1.364
	C–S	1.68		Hg–S–C	103.6	108° [b] (DMSO), 102° [b] (water)		
	C≡N	1.17		S–C≡N	177.1			
$[Hg(SCN)_4(H_2O)_2]^{2-}$ solvated	Hg–S	2.56	2.531[b1], 2.547[b2] (DMSO), 2.54[c] (water)	S–Hg–S	108.7		-1329514.7649	12.4823
	C–S	1.68		Hg–S–C	103.5	108° [b] (DMSO), 102° [b] (water)		
	C≡N	1.17		S–C≡N	178.0			

[a1], [a2] Taken from Ref. [47]
[b], [b1], [b2] Taken from Ref. [196]
[c] Taken from Ref. [199]
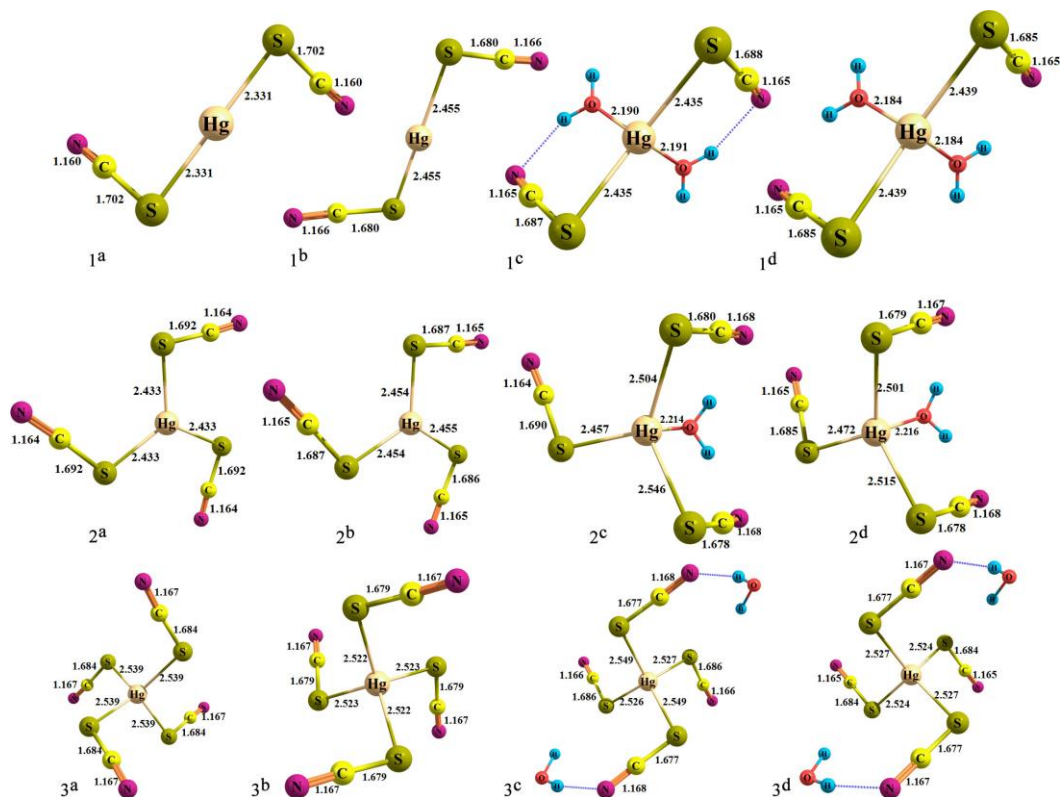
Figure 4.12. Energy-minimized structures of $[Hg(SCN)_n]^{2-n}$ complexes. $\mathbf{1^a}$ $Hg(SCN)_2$ non-solvated, $\mathbf{1^b}$ $Hg(SCN)_2$ implicit solvation, $\mathbf{1^c}$ $Hg(SCN)_2(H_2O)_2$ explicit solvation, $\mathbf{1^d}$ $Hg(SCN)_2(H_2O)_2$ explicit/implicit solvation, $\mathbf{2^a}$ $[Hg(SCN)_3]^-$ non-solvated, $\mathbf{2^b}$ $[Hg(SCN)_3]^-$ implicit solvation, $\mathbf{2^c}$ $[Hg(SCN)_3(H_2O)]^-$ explicit solvation, $\mathbf{2^d}$ $[Hg(SCN)_3(H_2O)]^-$ explicit/implicit solvation, $\mathbf{3^a}$ $[Hg(SCN)_4]^{2-}$ non-solvated, $\mathbf{3^b}$ $[Hg(SCN)_4]^{2-}$ implicit solvation, $\mathbf{3^c}$ $[Hg(SCN)_4(H_2O)_2]^{2-}$ explicit solvation, $\mathbf{3^d}$ $[Hg(SCN)_4(H_2O)_2]^{2-}$ explicit/implicit solvation

Comparing the optimization results of $Hg(SCN)_2$ complex without the solvation effect and using solvation (implicit or/and explicit water molecules), it can be seen that there is a clear differences between the energies of non-solvated complex and using implicit solvation. Also the effect of each implicit or explicit solvation markedly changed the dipole moment (Table 4.6). According to the calculation results, the most polar molecule is $Hg(SCN)_2$ in non-solvated environment. Comparing the calculated Hg–S bond distances it was observed that both the implicit and explicit solvation separately induces the elongation of bond between Hg and S atoms compared with non-solvated model. But the effect of both solvation models in tandem does not change the Hg–S bond length comparing with the explicit solvation effect alone. The C–S and C≡N bond lengths almost do not differ in all the cases. The main and clear changes are the energy and dipole moment when the solvation effects are introduced into the system. Based on the simulation data it was found that the complex ion $[Hg(SCN)_3]^-$ is the most polar of all analyzed complexes when both the explicit and implicit solvation models were applied. The bond differences between the Hg–S atoms of non-solvated $[Hg(SCN)_3]^-$ complex compared with the different solvation models do not vary significantly. Nevertheless, the same tendency as was discussed about the $Hg(SCN)_2$ complex remains: each chemical environment promotes lengthening of Hg–S bond.

The optimized geometric parameters of $[Hg(SCN)_4]^{2-}$ complex ion showed that the difference of the analyzed parameters is high comparing the complex presented in non-solvated environment with the implicit solvation (Table 4.6). The differences are also much bigger comparing with the results of $Hg(SCN)_2$ and $[Hg(SCN)_3]^-$ complexes discussed above. The effect of explicit and implicit water molecules at the same time renders the complex ion $[Hg(SCN)_4]^{2-}$ more polar compared with rest solvation models or non-solvated $[Hg(SCN)_4]^{2-}$ complex ion. It was observed that the length of Hg–S bond of $[Hg(SCN)_4]^{2-}$ complex ion in each case is the only variable parameter while the lengths of C–S and C≡N bond remain constant. In contrast to the former discussions it was found out that the Hg–S bond becomes weakest when at the same time the explicit and implicit solvation is involved. The calculated length of Hg–S bond is in good agreement with experimentally identified bond length given by other authors [199] when the solvent is water. The deviation is $\pm$ 0.02 Å, while in the case of $[Hg(SCN)_4]^{2-}$ and $[Hg(SCN)_4(H_2O)_2]^{2-}$ ions in non-solvated environment the calculated and experimental values are identical. The bond angles of S–Hg–S and S–C≡N in each case also do not fluctuate markedly. However the prominent alteration of Hg–S–C angle was noticed. The disparity is between $0.1 - 6.1°$.

Generally there are some basic features that are characteristic for the optimized structures. The molecular modeling data clearly indicate the formation of four-coordinated Hg(II) complexes with four thiocyanate and (or) water ligands. The Hg–S–C fragment is always bent. Moreover, there is always a slight bending involved for the S–C≡N bond angle which varies between 1 and 4°. The Hg–S bond lengths increased with increasing the number of ligands. Consequently, the weakest bonding mode between metal ion and SCN^- ligand is for $[Hg(SCN)_4]^{2-}$ complex ion. Such

tendency also was noticed experimentally by other researches (Table 4.6) when the solvent was dimethylsulphoxide (DMSO).

4.3.2. Vibrational spectra of $[Hg(SCN)_n]^{2-n}$ complexes in the aqueous solution

The Raman spectra of aqueous solutions with the established molar ratio of Hg^{2+} and SCN^- ion were obtained. The vibrational spectral analysis was performed on the basis of literature and calculation data. The frequencies of the Hg–S, C–S, C≡N vibrational modes have been measured for the free SCN^- ion, neutral $Hg(SCN)_2$ molecule, anionic $[Hg(SCN)_3]^-$ and $[Hg(SCN)_4]^{2-}$ complexes when the solvent was water. The detailed vibrational assignments of fundamental modes along with the calculated peak intensities are shown in Table 4.7. For visual comparison, the observed and simulated Raman spectra are presented in Figure 4.13. For the interpretation of calculated and experimentally determined Raman spectra the attention mainly was focused on the analysis of the Raman spectra bands arising from the Hg–SCN and SCN^- groups. Two characteristic vibration modes have been assigned as valuable: v_1(Hg–S stretching mode) and v_2(C≡N stretching mode), respectively.

The results of the performed Raman spectroscopic analysis for SCN^- anion are in good agreement with the characteristic values for the vC–S, vC≡N stretching and δS–C≡N bending modes of the thiocyanate anion listed in literature [150**Error! Bookmark not defined.**] and with the calculated Raman spectra. Three regions with different frequencies are attributed for free SCN^- ion in the vibrational spectra (460–465 cm^{-1}, S–C≡N bending vibration modes, 730–756 cm^{-1}, C–S stretching, and 2120–2148 cm^{-1}, C≡N stretching vibration modes). Unfortunately, the S–C≡N deformation vibrational mode was not revealed in the experimental Raman spectra and also was very weak in the calculated spectra.

The calculation data from the Table 4.7 show that the vHg–S vibration is sensitive to the number of SCN^- ligands. As the number of bound SCN^- ions increases, the effective charge on the Hg metal decreases and the vHg–S vibration number becomes lower. This tendency was confirmed by the Raman spectral analysis. The decrease of vHg–S vibration number was observed earlier by Šašić *et. al.* [73]. Additionally, the behavior of vHg–S vibration in the case of increasing number of SCN^- ligands remains when the water is changed to other solvents such as DMSO or dimethylformamide (DMF) [73, 75, 196]. The presence of the third SCN^- ion reduces the positive charge of Hg^{2+} and the experimental vHg–S downshifts by about 22–28 cm^{-1}, compared with those of the corresponding solution of $Hg(SCN)_2$. Attachment of fourth ligand to the Hg^{2+} ion causes a further decrease in the vHg–S wavenumber of about 5–12 cm^{-1} compared with the $[Hg(SCN)_3]^-$. The calculated differences of vHg–S vibrations are greater, depending on the each hypothetical case.

Table 4.7. Vibrational assignments of $Hg(SCN)_2$, $[Hg(SCN)_3]^-$, $[Hg(SCN)_4]^{2-}$ complexes in the different hypothetical cases obtained from DFT calculations and determined experimentally

Complex	Vibrational assignments	Calculated unscaled frequency (average) H_2O (D_2O), cm^{-1}	Intensity	Scaled frequency (scale factor 0.9688) H_2O (D_2O), cm^{-1}	Experimental frequency in H_2O (D_2O), cm^{-1}	Experimental frequency according to the literature, cm^{-1}
SCN$^-$	δS–C≡N	460	w			
	νC–S	730	m		750	747[e]
	νC≡N	2132	s	2066	2068	2068[e]
SCN$^-$ solvated	δS–C≡N	465	vw			
	νC–S	742	w		750	747[e]
	νC≡N	2120	s	2054	2068	2068[e]
[(SCN$^-$)(H$_2$O)$_2$]$^-$	δS–C≡N	465	vw			
	νC–S	756	w		750	747[e]
	νC≡N	2148	s	2081	2068	2068[e]
[(SCN$^-$)(H$_2$O)$_2$]$^-$ solvated	δS–C≡N	465	vw			
	νC–S	756	w		750	747[e]
	νC≡N	2148	s	2081	2068	2068[e]
Hg(SCN)$_2$	νHg–S	290	m		284 (281, 256)	266[a], 264[b] (DMSO), 271[b] (DMF), 279[b] (water)
	δS–C≡N	434	vw		451	
	νC–S	687	vw			
	νC≡N	2253	vs	2182	2147 (2146)	2131[c] (DMSO)
Hg(SCN)$_2$ solvated	νHg–S	211	vw		284 (281, 256)	266[a], 264[b] (DMSO), 271[b] (DMF), 279[b] (water)
	δS–C≡N	434	vw		451	
	νC–S	716	vw			
	νC≡N	2197	vs	2129	2147 (2146)	2131[c] (DMSO)
Hg(SCN)$_2$(H$_2$O)$_2$	νHg–S	245, 302 (245, 289)	m		284 (281, 256)	266[a], 264[b] (DMSO), 271[b] (DMF), 279[b] (water)
	δS–C≡N	475	vw		451	

Table 4.7. Continued

Complex	Vibrational assignments	Calculated unscaled frequency (average) H$_2$O (D$_2$O), cm^{-1}	Intensity	Scaled frequency (scale factor 0.9688) H$_2$O (D$_2$O), cm^{-1}	Experimental frequency in H$_2$O (D$_2$O), cm^{-1}	Experimental frequency according to the literature, cm^{-1}
	νC–S	708	w			
	νC≡N	2209 (2210)	vs	2141 (2141)	2147 (2146)	2131[c] (DMSO)
Hg(SCN)$_2$(H$_2$O)$_2$ solvated	νHg–S	236, 302 (237, 291)	m		284 (281, 256)	266[a], 264[b] (DMSO), 271[b] (DMF), 279[b] (water)
	δS–C≡N	474	vw		451	
	νC–S	706	m			
	νC≡N	2204 (2202)	vs	2135 (2134)	2147 (2146)	2131[c] (DMSO)
[Hg(SCN)$_3$]$^-$	νHg–S	255	m		256 (255), 262 (261)	242[a], 246[b] (DMSO), 248[b] (DMF), 252[b] (water)
	δS–C≡N	422	vw		453	
	νC–S	699	w			714[c] (water)
	νC≡N	2223	vs	2153	2131 (2132), 2137 (2138)	2119[c] (DMSO). 2117[c] (water)
[Hg(SCN)$_3$]$^-$ solvated	νHg–S	239	m		256 (255), 262 (261)	242[a], 246[b] (DMSO), 248[b] (DMF), 252[b] (water)
	δS–C≡N	428	w		453	
	νC–S	707	w			714[c] (water)
	νC≡N	2211	vs	2142	2131 (2132), 2137 (2138)	2119[c] (DMSO). 2117[c] (water)
[Hg(SCN)$_3$(H$_2$O)]$^-$	νHg–S	245, 282 (246, 271)	m		256 (255), 262 (261)	242[a], 246[b] (DMSO), 248[b] (DMF), 252[b] (water)
	δS–C≡N	425	vw		453	
	νC–S	717	w			714[c] (water)
	νC≡N	2189, 2219 (2188, 2218)	vs	2121, 2150 (2121, 2150)	2131 (2132), 2137 (2138)	2119[c] (DMSO). 2117[c] (water)
[Hg(SCN)$_3$(H$_2$O)]$^-$ solvated	νHg–S	237, 278 (233, 271)	w		256 (255), 262 (261)	242[a], 246[b] (DMSO), 248[b] (DMF), 252[b] (water)

Table 4.7. Continued

Complex	Vibrational assignments	Calculated unscaled frequency (average) H_2O (D_2O), cm^{-1}	Intensity	Scaled frequency (scale factor 0.9688) H_2O (D_2O), cm^{-1}	Experimental frequency in H_2O (D_2O), cm^{-1}	Experimental frequency according to the literature, cm^{-1}
	δS–C≡N	426	vw		453	
	νC–S	715	w			714[c] (water)
	νC≡N	2188, 2205 (2186, 2206)	vs	2119, 2137 (2119, 2137)	2131 (2132), 2137 (2138)	2119[c] (DMSO). 2117[c] (water)
[Hg(SCN)$_4$]$^{2-}$	νHg–S	206, 219	m		240 (240), 252 (252)	235[a1], 234[b] (DMSO), 234[b] (DMF), 238[b] (water)
	δS–C≡N	433	vw		454	
	νC–S	709	vw		717 (717)	710[d], 717[e], 714[c](water)
	νC≡N	2192	vs	2124	2122 (2122)	2117[d], 2117[c], 2114[e] (water)
[Hg(SCN)$_4$]$^{2-}$ solvated	νHg–S	217, 232	m		240 (240), 252 (252)	235[a1], 234[b] (DMSO), 234[b] (DMF), 238[b] (water)
	δS–C≡N	434	vw		454	
	νC–S	714	w		717 (717)	710[d], 717[e], 714[c](water)
	νC≡N	2190	vs	2122	2122 (2122)	2117[d], 2117[c], 2114[e] (water)
[Hg(SCN)$_4$(H$_2$O)$_2$]$^{2-}$	νHg–S	206, 223 (206, 224)	m		240 (240), 252 (252)	235[a1], 234[b] (DMSO), 234[b] (DMF), 238[b] (water)
	δS–C≡N	405, 433	vw		454	
	νC–S	708,722	w		717 (717)	710[d], 717[e], 714[c](water)
	νC≡N	2199 (2197)	vs	2130 (2130)	2122 (2122)	2117[d], 2117[c], 2114[e] (water)

[a], [a1] Taken from Ref. [196]
[b] Taken from Ref. [73]
[c] Taken from Ref. [75]
[d] Taken from Ref. [199]
[e] Taken from Ref. [200]
Abbreviations: s – strong; m – medium; w – weak; vw – very weak; vs – very strong; ν – stretching; δ – deformation
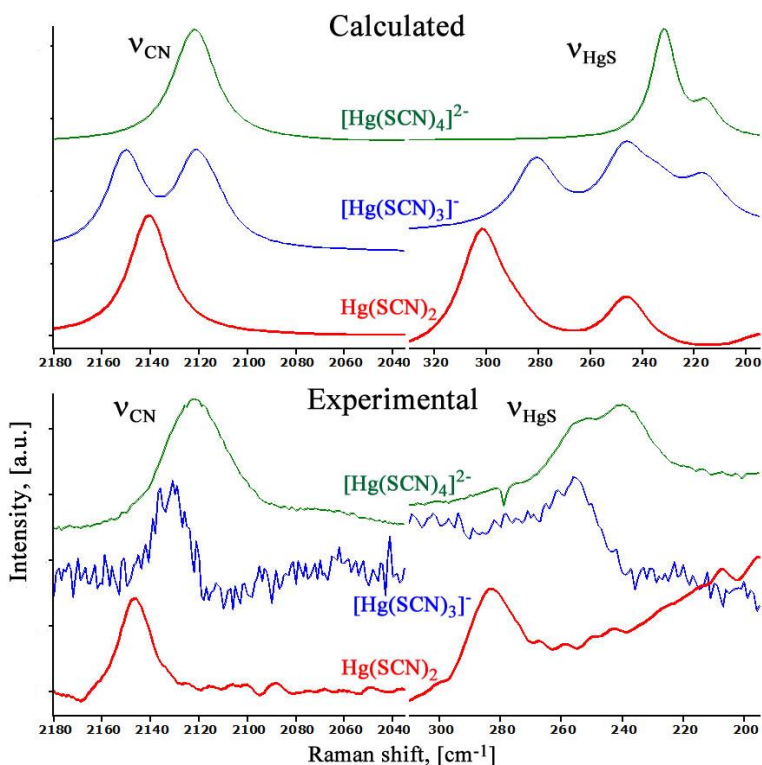
Figure 4.13. The calculated and experimental Raman spectrum of each $[Hg(SCN)_n]^{2-n}$ complex in the aqueous solution in a range of 200–320 cm^{-1} and 2040–2180 cm^{-1}

The calculated and experimentally observed νC–S vibration modes were not informative in this study because the signal always was very weak or weak. Furthermore, it was noticed that the signal of νC–S band gets better with the added number of SCN$^-$ ligand. In the case of $[Hg(SCN)_4]^{2-}$ it was possible to identify the νC–S vibration at 717 cm^{-1}. There is a lack of such data in literature too. It was found only some experimental values of νC–S vibration in water solution (Table 4.7) and only for $[Hg(SCN)_3]^-$ and $[Hg(SCN)_4]^{2-}$ complexes.

The greatest changes in $\Delta\nu$ were identified for νC≡N vibration according to the experimental and calculated data. The tendency is the same: the increased number of SCN$^-$ ligands shifts the νC≡N vibration to the lower wavenumber position. Generally, it can be stated that the more ligands are introduced in the complexation, the weaker Hg–S and C≡N bond is formed. This was confirmed by calculated bond length (Table 4.6). Figure 4.13 shows the Raman spectra of Hg^{2+} ion coordinated series in the νHg–S and νC≡N regions. All the peaks of νHg–S and νC≡N stretching modes are sufficiently well separated from the peaks of the free SCN$^-$.

In general the solutions containing $[Hg(SCN)_3]^-$ complex ion gave spectra which were more difficult to analyze. It is known that $[Hg(SCN)_3]^-$ complex ion is

prone to partial disproportionation to $Hg(SCN)_2$ and $[Hg(SCN)_4]^{2-}$ species [196]. Such feature has been recognized during preparation procedure of the solution containing $[Hg(SCN)_3]^-$ complex ion. The solution became turbid due to the formation of the slightly soluble $Hg(SCN)_2$ complex. Raman spectra of the solution, containing $[Hg(SCN)_3]^-$ complex ion, exhibited three well separated peaks at 2143 cm^{-1}, 2131 cm^{-1} and 2070 cm^{-1}. The first one is very similar to $\nu C{\equiv}N$ vibrational mode of $Hg(SCN)_2$ complex and the third is associated with $\nu C{\equiv}N$ vibration of free SCN^- group. In order to improve the assignment of Raman spectra of $[Hg(SCN)_3]^-$ complex ion, the subtraction of the spectra of $Hg(SCN)_2$ and $[Hg(SCN)_4]^{2-}$ complexes from the spectrum of $[Hg(SCN)_3]^-$ complex was made. Difference spectrum displayed two peaks 2131 cm^{-1} and 2137 cm^{-1} in $\nu C{\equiv}N$ region and two 256 cm^{-1}, 261 cm^{-1} peaks in $\nu Hg{-}S$ region, respectively. This double-peak character of mentioned regions was also displayed in the calculation results (Table 4.7). It was presumed that the assignment of 2117 cm^{-1} peak to $\nu C{\equiv}N$ vibration for both $[Hg(SCN)_3]^-$ and $[Hg(SCN)_4]^{2-}$ complexes of other researches [76] is incorrect and the disproportionation feature of $[Hg(SCN)_3]^-$ complex ion was not taken into account. In addition, the peak of $\nu C{\equiv}N$ vibration mode of free SCN^- ion at 2066 cm^{-1} in each analyzed $[Hg(SCN)_n]^{2-n}$ aqueous solution was observed. On the contrary, this peculiarity is not characteristic for mercury(II) thiocyanate complexes in DMSO solution [196]. Moreover, the calculated and experimental Raman spectra showed previously unnoticed splitting of $\nu Hg{-}S$ peak of $[Hg(SCN)_4]^{2-}$ complex ion (Table 4.7, Fig. 4.13).

The analysis of experimental Raman spectra of $Hg(SCN)_2$ complex was the most complicated due to its low solubility. Therefore, the weak signals with low signal to noise ratio have been obtained. Also the splitting character of $\nu Hg{-}S$ compared with $[Hg(SCN)_3]^-$ and $[Hg(SCN)_4]^{2-}$ ions in the experimental spectra was not recognized.

Based on the comparison of the calculated and experimental Raman spectra of each mercury(II) thiocyanate complex in different hypothetical case (with implicit or explicit water molecules) the attempt to determine the most reliable structure of each complex has been made. In the case of $Hg(SCN)_2$ and $[Hg(SCN)_3]^-$ ion it can be seen that the calculated Raman spectra correlates well with the experimental one when the $Hg(SCN)_2$ complex includes two water molecules and the $[Hg(SCN)_3]^-$ complex ion — one water molecule as the ligand. The addition of implicit water molecules slightly improves the results. Based on the data for $[Hg(SCN)_4]^{2-}$ complex ion the other trend was noticed. The implicit solvation model around the $[Hg(SCN)_4]^{2-}$ complex ion in aqueous media represented the most probable mode and the calculated model with the explicitly added water molecules only impaired the results. These data clearly indicate the formation of four-coordinated mercury(II) thiocyanate complexes in the water environment.

4.3.3. Vibrational spectra of $[Hg(SCN)_n]^{2-n}$ complexes in the heavy water solution

In order to perform the assignments of fundamental vibrational modes of each $[Hg(SCN)_n]^{2-n}$ complex properly as well as verify the interaction of ligands with Hg^{2+} ion, the isotopic substitutions were made. Presumably, if the Hg^{2+} ion in the all three complexes is four-coordinated, the H_2O replacement with D_2O will have the minimal influence on fundamental vibrations of $[Hg(SCN)_4]^{2-}$ complex and maximal on $Hg(SCN)_2$ complex. The performed calculations with two H_2O/D_2O molecules for the $[Hg(SCN)_4]^{2-}$ complex ion showed almost identical peaks in the Raman spectra. In excellent agreement with the calculated spectra, the experimental spectra in both these cases were identical. In the case of $Hg(SCN)_2$ the calculations showed that the frequency of $\nu C\equiv N$ stretching vibration was not sensitive to isotopic exchange. On the contrary, the second $\nu Hg-S$ vibration at 302 cm^{-1} decreased by 13 cm^{-1} (while the first one at 245 cm^{-1} was steady) via H_2O/D_2O exchange modeling (Table 4.7). It should be noted that the vibrations at the 250–300 cm^{-1} region are complex vibrations of Hg–S and Hg–O stretching. Additionally, it is obvious that the isotopic substitution has substantial influence to the $\nu Hg-S$ and $\nu Hg-O$ stretching modes. This tendency was observed in the experimental Raman spectra of $Hg(SCN)_2$ as well. After the isotopic exchange the $\nu C\equiv N$ stretching remains unchanged and the $\nu Hg-S$ stretching decreased by 3 cm^{-1}. Additionally, the Raman spectra of $Hg(SCN)_2$ in D_2O exhibited one further $\nu Hg-S$ peak at 256 cm^{-1} (Fig. 4.14). The calculated Raman spectra of $Hg(SCN)_2$ in the D_2O and H_2O also displayed two well separated $\nu Hg-S$ stretching modes. It can be assumed that the H_2O environment hides one of Hg–S stretching modes due to weak intensity of signal and low solubility of $Hg(SCN)_2$ complex in water.
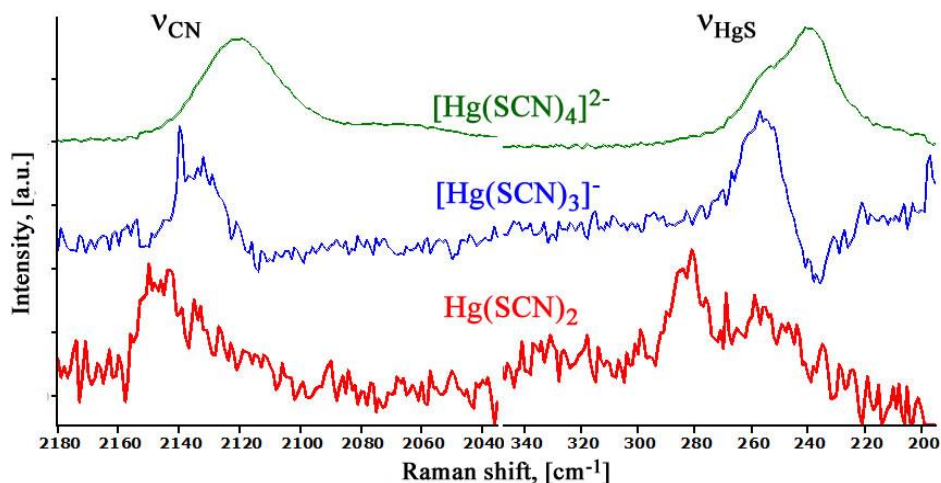
Figure 4.14. The experimental Raman $\nu Hg-S$ and $\nu C\equiv N$ stretching vibrational spectra for the $[Hg(SCN)_n]^{2-n}$ complexes in the heavy water solution

In general, the isotopic changes have played an important role in performing better vibrational assignments. It was possible to identify the second νHg–S vibrational mode in the case of $Hg(SCN)_2$ and confirm that the Hg^{2+} ion in the all complexes is four-coordinated.

4.3.4. UV spectra of $[Hg(SCN)_n]^{2-n}$ complexes in the aqueous solution

The experimental electronic spectra supplemented by simulated spectra of the $Hg(SCN)_2$, $[Hg(SCN)_3]^-$, $[Hg(SCN)_4]^{2-}$ complexes are missing. According to this the research in order to assess the performance of the different functionals on the calculation results of UV spectra was performed. Different functionals, including different solvation effects, in order to understand how taking into account these contributions the accuracy of reproducing the experimental spectra can be improved were considered. Starting from the optimized geometry obtained by DFT B3LYP calculations the electronic spectra were calculated using B3LYP, PBE1PBE and PBEPBE levels of theory for each hypothetical case.

The experimental spectra of $Hg(SCN)_2$, $[Hg(SCN)_3]^-$, $[Hg(SCN)_4]^{2-}$ complexes together with the TD-DFT calculated ones are reported in the Figure 4.15.

The experimental spectrum of $Hg(SCN)_2$ presents an intense and sharp maximum in the region of the spectrum extending from ~ 208 to 240 nm with maximum of 222 nm. Moreover, a much lesser intense absorption band was identified near the latter one centered at about 267 nm. Actually, it was observed that the use of PBE1PBE functional corresponds better to the experimentally obtained data in each hypothetical case. Indeed, the used PBE1PBE functional together with both explicit and implicit solvation models exhibited an absorption maximum and band shape in better agreement with the experimental results. In this case, the deviation from the experimental maximum of about 4 nm for most intense peak, and about 2 nm for the second one, even if the band intensities were less well reproduced, was obtained. The worst results were obtained using the PBEPBE functional.

The experimental absorption spectra of $[Hg(SCN)_3]^-$ complex is similar to experimental spectra of $Hg(SCN)_2$ complex. The only differences lie in the less intensive absorption band region. Here the hipsochromic shift with the maximum of 262.5 nm was observed and the intensity of 222 nm peak is higher of about 0.05 compared with the peak of 222 nm of $Hg(SCN)_2$ complex. The computed spectrum using the PBE1PBE hybrid functional in common with the explicit solvation showed a very good agreement with its experimental counterpart over the entire spectra. Even spectral features with lower intensity were nicely reproduced.

The experimental electronic spectra of $[Hg(SCN)_4]^{2-}$ complex ion do not differ greatly from the spectra of $Hg(SCN)_2$ and $[Hg(SCN)_3]^-$ complexes. The main peak centers at 222 nm and the second one (identified using fitting) has maximum at 260 nm which shows the small hipsochromic shift compared with the spectra of $[Hg(SCN)_3]^-$ complex. As was previous established for $Hg(SCN)_2$ and $[Hg(SCN)_3]^-$ complexes, the theoretical description using the PBE1PBE functional is the best for

$[Hg(SCN)_4]^{2-}$ complex too. However, unlike the previous discussed, the implicit solvation model is the most characteristic for $[Hg(SCN)_4]^{2-}$ complex. The computed electronic spectrum also showed a good agreement with the experiment one indicating that analyzed systems were treated accurately by means of TD-DFT method. The calculated maximum in the less intensive absorption band region as well as the intense and sharp one differ by 6 nm from experimentally determined values.
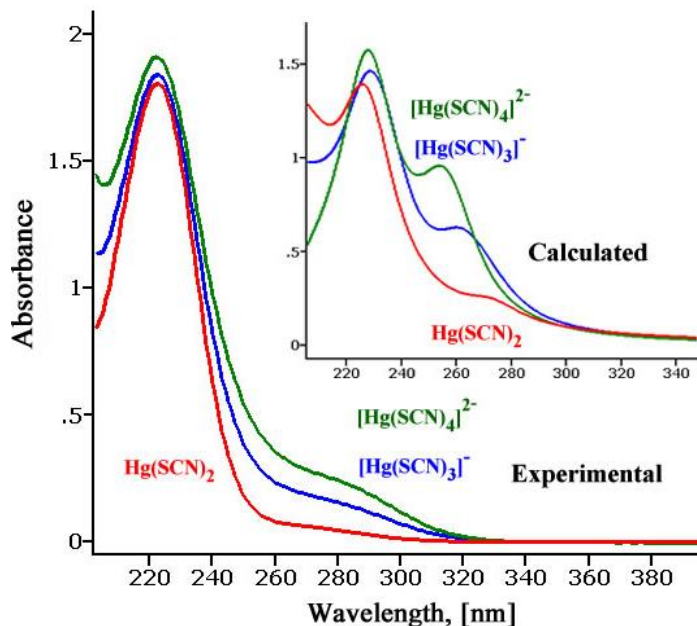
Figure 4.15. The calculated and experimental absorption spectra of $Hg(SCN)_2$, $[Hg(SCN)_3]^-$, $[Hg(SCN)_4]^{2-}$ complexes in aqueous solution

The obtained TD-DFT calculation results show that the selection of the functional, that sometimes may be not fairly applied, can bring important differences on the final simulated absorption spectra. In general all the computed spectra at PBE1PBE level shows an almost perfect agreement with the experimental electronic spectra and even spectral features with lower intensity are adequately reproduced. Additionally, the arrangement of peaks from the lowest intensity of $Hg(SCN)_2$ complex to highest intensity of $[Hg(SCN)_4]^{2-}$ complex is perfectly restored too. Moreover, the experimental and computed data showed that the increasing number of SCN^- ligands in the analyzed complexes with Hg^{2+} ion, induces the hipsochromic shift in the less intense absorption band region.

4.4. Raman spectroscopic study of aqueous mixture of mercury(II) and iron(III) thiocyanates

This section briefly illustrates the application of the obtained knowledge on the characteristic vibrational properties of explored complexes for the analysis of a series of Hg(II) thiocyanate and Fe(III) monoisothiocyanate complexes, which are formed simultaneously during simple titrimetric analysis.

The formation constants between Hg^{2+} and SCN^- ions are larger than between Fe^{3+} and SCN^- ions (see Eqs. (3)–(7)). The complexation mainly follows the reactions [180, 201, 202]:

$$Hg^{2+}(aq) + SCN^-(aq) \rightarrow [Hg(SCN)]^+(aq) \qquad K_1 = 2.0 \times 10^8 \qquad (3)$$

$$HgSCN^+(aq) + SCN^-(aq) \rightarrow Hg(SCN)_2(aq) \qquad K_2 = 1.0 \times 10^8 \qquad (4)$$

$$Hg(SCN)_2(aq) + SCN^-(aq) \rightarrow [Hg(SCN)_3]^-(aq) \qquad K_3 = 7.0 \times 10^2 \qquad (5)$$

$$Hg(SCN)_3^-(aq) + SCN^-(aq) \rightarrow [Hg(SCN)_4]^{2-}(aq) \qquad K_4 = 7.0 \times 10^1 \qquad (6)$$

$$Fe^{3+}(aq) + SCN^-(aq) \rightarrow [Fe(SCN)]^{2+}(aq) \qquad K_5 = 8.9 \times 10^2 \qquad (7)$$
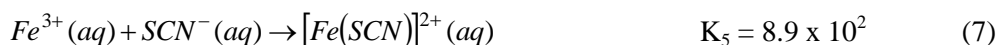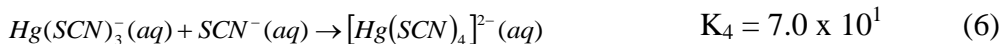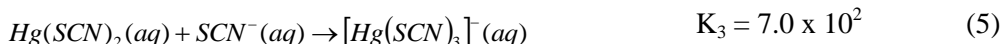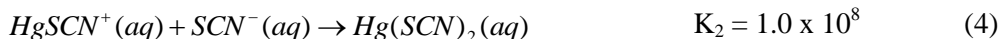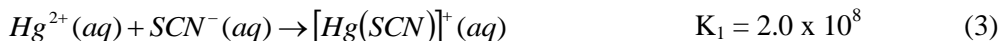
Based on the values of formation constants of complexes between Hg^{2+} and Fe^{3+}, and SCN^- ions respectively, the magnitude of formation constant K_2 of $[Hg(SCN)_2]$ in an aqueous solution, indicates that Hg^{2+} ions have a far greater affinity for SCN^- ion than does Fe^{3+} ion. K_3 of $[(Hg(SCN)_3]^-$ and K_5 of $Fe(NCS)^{2+}$ are the same order of magnitude. However, the K_3 is a little higher than K_2 and red $[Fe(NCS)]^{2+}$ complex is formed, indicating the end-point of titration. According to Li X-G. et al., (2008) [14] the colorless $[Hg(SCN)_2]$ complex is the only speciation for mercury(II) in the sample at the equivalence-point. This conclusion is denied by the performed analysis of a number of calculated and experimentally observed Raman spectra of mercury(II) and iron(III) thiocyanate complexes and their mixtures. The obtained data indicate that at the end-point of titration when red $[Fe(NCS)]^{2+}$ complex appears, the $[Hg(SCN)_3]^-$ complex ion is formed also. It was mentioned that the $[Hg(SCN)_3]^-$ is prone to partial disproportionation to $Hg(SCN)_2$ and $[Hg(SCN)_4]^{2-}$ species. This disproportionation character was confirmed by the in detail performed assignments of fundamental vibrational modes of each mercury(II)-thiocyanate and iron(III)-thiocyanate complex. Figure 4.16 presents the evidence of speciation visually.
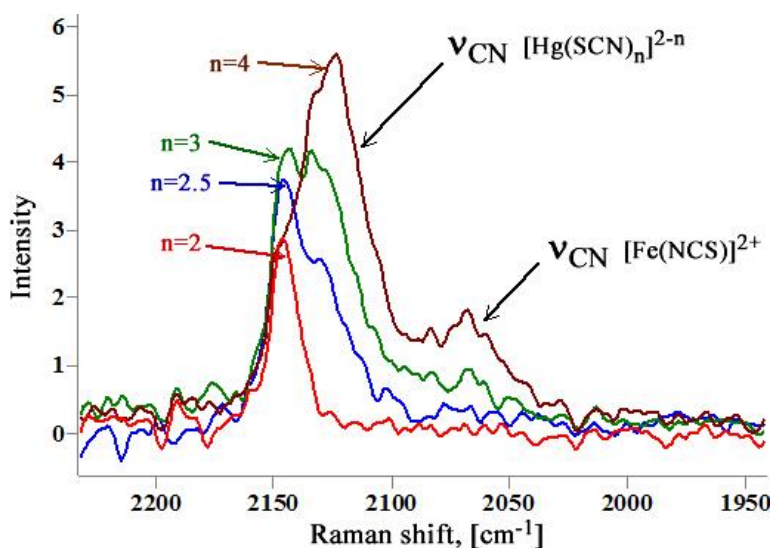
Figure 4.16. The experimental Raman $\nu C\equiv N$ stretching vibrational spectra for the mixture of $[Hg(SCN)_n]^{2-n}$ and $[Fe(NCS)]^{2+}$ complexes in the aqueous solution

It is clearly seen that not only the characteristic $\nu C\equiv N$ vibrational band for $[Hg(SCN)_3]^-$ complex exists, but also the appearance of characteristic $\nu C=N$ band for $[Fe(NCS)]^{2+}$ complex at ~ 2065 cm^{-1} is evident. The origin of the latter could be perceived even when the Hg^{2+} and SCN^- molar ratio is 1 : 2.5, while there is no doubt in the case of $[Hg(SCN)_4]^{2-}$.

5. THE MAIN RESULTS AND CONCLUSIONS

1. Detailed vibrational assignments of the fundamental vibrational modes of iron(III) isothiocyanates were determined by isotopic H_2O/D_2O exchange, Raman spectra subtraction analysis on experimental Raman spectra, and PED analysis on calculated Raman spectra. The bands near 2067 cm^{-1}, 1139 cm^{-1}, 1042 cm^{-1}, 750 cm^{-1}, 465 cm^{-1}, 422 cm^{-1}, 295 cm^{-1} have been assigned to νC=N, bound ν_{as}S=O, bound ν_sS=O, νC=S, δH–O–H, δN=C=S, νFe–N vibrations of the iron(III) monoisothiocyanate in aqueous acidic solution, respectively.

2. Calculated Raman and UV spectra of iron(III) monoisothiocyanate, when the SO_4^{2-} ligand was situated near the NCS^- ligand, corresponded better to the experimentally recorded Raman and UV spectra. The analysis of explicit and/or implicit solvation indicated that the explicit and implicit solvation model in tandem is more appropriate for the calculation of Raman spectra of the titled complex than explicit model alone. Experimental UV spectrum is better described by the explicit solvation model.

3. Fifteen most important vertical electronic transitions in terms of oscillator strength (greater than 0.01) have been identified. The vast majority of electronic transitions are characterized as ligand-to-metal (LMCT) charge transfers, where the NCS^- and SO_4^{2-} ligands act as the principal electron donor groups. The results of calculations using different methods and functionals show that the choice of the functional used for TD calculations is much more important than the choice of the method used for geometry optimization. The PBE1PBE and CAM-B3LYP methods used for geometry optimization gave very similar absorption spectra, while slightly different spectral tendencies using B3LYP were observed.

4. Detailed vibrational assignments of the fundamental vibrational modes of mercury(II) thiocyanates were determined by isotopic H_2O/D_2O exchange, Raman spectra subtraction analysis on experimental Raman spectra. The vibrational bands at 2122 cm^{-1} (νC≡N), 717 cm^{-1} (νC–S), 454 cm^{-1} (δS–C≡N), 240 and 252 cm^{-1} (νHg–S) have been identified for the $[Hg(SCN)_4]^{2-}$ complex. The vibrational bands at 2131 cm^{-1} (νC≡N), 453 cm^{-1} (δS–C≡N), 256 and 262 cm^{-1} (νHg–S) have been attributed to the $[Hg(SCN)_3]^-$ complex. The vibrational bands at 2147 cm^{-1} (νC≡N), 451 cm^{-1} (δS–C≡N), 284 cm^{-1} (νHg–S) have been assigned to the $[Hg(SCN)_2]$ complex.

5. In the case of $Hg(SCN)_2$ and $[Hg(SCN)_3]^-$ complex ions, the calculated Raman spectra correlates well with the experimental one when the explicit solvation has been used. The addition of implicit water molecules slightly improved the results. For the $[Hg(SCN)_4]^{2-}$ complex ion, the implicit solvation model represented the spectra in better agreement with the experimentally observed. The obtained TD-PBE1PBE calculation results show almost perfect agreement with the experimental electronic spectra and even spectral features with lower intensity were adequately reproduced.

6. The $[Hg(SCN)_2]$ complex ion is not the only speciation for mercury(II) in the sample when Fe^{3+}, Hg^{2+}, and SCN^- ions are presented. The presence of $[Hg(SCN)_3]^{1-}$ complex ion, which prones to partial disproportionation to $Hg(SCN)_2$ and $[Hg(SCN)_4]^{2-}$ species, has been established.

6. REFERENCES

1. Machura, B., *et. al*. Synthesis, spectroscopic characterization, X-ray structure, and DFT calculations of [Cu(tppz)(SCN)2]. *Journal of Structural Chemistry*, 2013, vol. 24, p. 89-96.

2. Małecki, J. G.; Gron, T.; Duda, H. Structural, spectroscopic and magnetic properties of thiocyanate complexes of Mn(II), Ni(II) and Cu(II) with the 1-methylimidazole ligand. *Polyhedron*, 2012, vol. 36, no. 1, p. 56-68.

3. Shukla, M., *et. al*. Synthesis, structure, UV–Vis–IR spectra, magnetism and theoretical studies on CuII[(2-aminomethyl)pyridine](thiocyanate)2 and comparisons with an analogous CuII complex. *Polyhedron*, 2011, vol. 30, no. 5, p. 754-763.

4. Bhattacharjee, C. R.; Goswami, P.; Mondal, P. Synthesis, structural characterization, and DFT studies of new mixed-ligand iron(III) Schiff-base complexes. *Journal of Coordination Chemistry*, 2010, vol. 63, no. 11, p. 2002-2011.

5. Cao, P., *et. al*. Potential Dependence of the Orientation of Thiocyanate Adsorbed on an Iron Electrode as Probed by Surface-Enhanced Raman Spectroscopy. *Journal of Physical Chemistry B*, 2002, vol. 106, no. 29, p. 7283-7285.

6. Bučko, T., *et. al*. Spin crossover transition of Fe(phen)2(NCS)2: periodic dispersion-corrected density-functional study. *Physical Chemistry Chemical Physics*, 2012, vol. 14, no. 16, p. 5389-5396.

7. Małecki, J. G., *et. al*. Thiocyanate manganese(II) complexes with pyridine and its derivatives ligands. *Polyhedron*, 2011, vol. 30, no. 5, p. 746-753.

8. Machura, B., *et. al*. Cu(II), Ni(II), and Hg(II) thiocyanate complexes incorporating 4,5-diazafluoren-9-one: synthesis, spectroscopic characterization, X-ray studies, and magnetic properties. *Journal of Structural Chemistry*, 2011, vol. 22, no. 5, p. 1053-1064.

9. Fukushima, N., *et. al*. Ab initio density functional studies on the stability of tetrathiocyanato complexes of Zn(II), Cd(II) and Hg(II). *Inorganica Chimica Acta*, 1997, vol. 255, no. 1, p. 211-214.

10. Gancheff, J. S., *et. al*. Experimental, DFT and TD-DFT studies of rhenium complexes with thiocyanate ligands. *Inorganica Chimica Acta*, 2012, vol. 387, p. 314-320.

11. Khandar, A. A., *et. al*. Dicarboxylate assisted synthesis of the monoclinic heterometallic tetrathiocyanato bridged copper(II) and mercury(II) coordination polymer {Cu[Hg(SCN)4]}n: Synthesis, structural, vibration, luminescence, EPR studies and DFT calculations. *Journal of Solid State Chemistry*, 2011, vol. 184, no. 2, p. 379-386.

12. Machura, B., *et. al*. Novel copper complexes based on the thiocyanate bridge – Synthesis, X-ray studies and magnetic properties. *Polyhedron*, 2011, vol. 30, no. 5, p. 832-840.

13. Cirello-Egamino, J.; Brindle, I. D. Determination of chloride ions by reaction with mercury thiocyanate in the absence of iron(III) using a UV-photometric, flow injection method. *Analyst*, 1995, vol. 120, no. 1, p. 183–186.

14. Li, X.-G.; Dou, Q.; Huang, M.-R. Titrimetric analysis of total mercury ions. *Monatshefte für Chemie - Chemical Monthly*, 2008, vol. 139, no. 10, p. 1157-1162.

15. Mihaljević, B.; Katušin-Ražem, B.; Ražem, D. The reevaluation of the ferric thiocyanate assay for lipid hydroperoxides with special considerations of the mechanistic aspects of the response. *Free Radical Biology and Medicine*, 1996, vol. 21, no. 1, p. 53-63.

16. Basavaiah, K.; Swamy, J. M. Application of potassium dichromate and iron–thiocyanate in the spectrophotometric investigations of phenothiazines. *Farmaco*, 2001, vol. 56, no. 8, p. 579-585.

17. Misiuk, W. Extractive spectrophotometric methods for the determination of doxepin hydrochloride in pharmaceutical preparations using titanium (IV) and iron (III) thiocyanate complexes. *Farmaco*, 2005, vol. 60, no. 1, p. 61-69.

18. Li, J., *et. al*. Thiocyanate hydrometallurgy for the recovery of gold. Part I: Chemical and thermodynamic considerations. *Hydrometallurgy*, 2012, vol. 113-114, p. 1-9.

19. Li, J., *et. al*. Thiocyanate hydrometallurgy for the recovery of gold. Part V: Process alternatives for solution concentration and purification. *Hydrometallurgy*. 2012, vol. 113-114, p. 31-38.

20. Wang, Q-M.; Guo, G-C.; Mak, T. C. W. Structural variation in cationic coordination networks in double salts of silver(I) thiocyanate and silver(I) selenocyanate. *Polyhedron*, 2001, vol. 20, no. 21, p. 2683-2687.

21. Kohle, O.; Ruile, S.; Grätzel, M. Ruthenium(II) Charge-Transfer Sensitizers Containing 4,4'-Dicarboxy-2,2'-bipyridine. Synthesis, Properties, and Bonding Mode of Coordinated Thio- and Selenocyanates. *Inorganic Chemistry*, 1996, vol. 35, no. 16, p. 4779-4787.

22. Shurdha, E., *et. al*. Extended Network Thiocyanate- and Tetracyanoethanide- based First-Row Transition Metal Complexes. *Inorganic Chemistry*, 2012, vol. 51, no. 18, p. 9655-9665.

23. Shultz, P. W.; Leroi, G. E.; Popov, A. I. Solvation of SCN- and SeCN- Anions in Hydrogen-Bonding Solvents. *Journal of the American Chemical Society*, 1996, vol. 118, no. 43, p. 10617-10625.

24. *Introduction to Coordination Chemistry*. Lawrance, G. A. Great Britain: John Wiley and Sons, Ltd., 2010. 304 p. ISBN: 978-0-470-51930-1.

25. Supkowski, R. M.; Horrocks, Wiliam DeW. On the determination of the number of water molecules, q, coordinated to europium(III) ions in solution from luminescence decay lifetimes. *Inorganica Chimica Acta*, 2002, vol. 340, p. 44-48.

26. Suffren, Y.; Rollet, F.-G.; Reber, C. Raman spectroscopy of transition metal complexes : molecular vibrational frequencies, phase transitions, isomers, and electronic structure. *Comments on Inorganic Chemistry*, 2011, vol. 32, no. 5-6, p. 246-276.

27. Schmidt, D. A.; Kopf, I.; Brundermann, E. A matter of scale: from far-field microscopy to near-field nanoscopy. *Laser & Photonics Reviews*, 2012, vol. 6, no. 3, p. 296-332.

28. Erras-Hanauer, H.; Clark, T.; van Eldik, R. Molecular orbital and DFT studies on water exchange mechanisms of metal ions. *Coordination Chemistry Reviews*, 2003, vol. 238–239, p. 233-253.

29. Autschbach, J. Density Functional Theory applied to calculating optical and spectroscopic properties of metal complexes: NMR and Optical Activity. *Coordination Chemistry Reviews*, 2007, vol. 251, no. 13-14, p. 1796-1821.

30. Kornobis, K., *et. al*. Electronically Excited States of Vitamin B12: Benchmark Calculations Including Time-Dependent Density Functional Theory and Correlated ab Initio Methods. *Journal of Physical Chemistry A*, 2011, vol. 115, no. 7, p. 1280-1292.

31. *Chemistry of Transition Elements*. Satake, M.; Mido, Y. India: Discovery Publishing House, 1994. 215 p. ISBN 81-7141-243-2.

32. *The Basics of Chemistry*. Myers, R. United States of America: Greenwood Publishing Group, Inc., 2003. 373 p. ISBN 0-313-31664-3.

33. Khandelwal, B. L.; Krishnan, V. *Chemistry of Transition Elements* [interactive] [2014-05-04]. Access: http://nsdl.niscair.res.in/jspui/handle/123456789/247.

34. *Inorganic Chemistry*, 2nd edition. Housecroft, C. E.; Sharpe, A. G. England: Person Education Limited, 2005. 949 p. ISBN-10: 0-13-039913-2, ISBN-13: 978-0-13-039913-7.

35. *d- and f- Block Chemistry*. Jones, C. J. Great Britain: John Wiley and Sons, Ltd., 2002. 184 p. ISBN 0-471-22476-6.

36. *Inorganic Chemistry*. Wulfsberg, G. United States of America: University Science Books, 2000. 983 p. ISBN 1-891389-01-7.

37. Ward, M. D. Transition-metal sensitized near-infrared luminescence from lanthanides in d-f heteronuclear arrays. *Coordination Chemistry Reviews*, 2007, vol. 251, no. 13-14, p. 1663-1677.

38. Zhao, B., *et. al*. Design and Synthesis of 3d−4f Metal-Based Zeolite-type Materials with a 3D Nanotubular Structure Encapsulated "Water" Pipe. *Journal of the American Chemical Society*, 2004, vol. 126, no. 10, p. 3012-3013.

39. Albrecht, M. Cyclometalation Using d-Block Transition Metals: Fundamental Aspects and Recent Trends. *Chemical Reviews*, 2010, vol. 110, no. 2, p. 576-623.

40. Ghosh, T., *et. al*. Thiocyanate and Dicyanamide Anion Controlled Nuclearity in Mn, Co, Ni, Cu, and Zn Metal Complexes with Hemilabile Ligand 2-Benzoylpyridine, *Crystal Growth & Design*, 2011, vol. 11, no. 7, p. 3198-3205.

41. Kong, L., *et. al*. Four divalent metal thiocyanate coordination compounds containing a rigid functional pyridine ligand. *Polyhedron*, 2010, vol. 29, no. 6, p. 1575-1582.

42. Das, S., *et. al*. Syntheses, structures and luminescence behaviours of Group 12 metal(II) thiocyanate complexes with a tetradentate Schiff base: Variation in molecular and crystalline architectures with the change of congeneric metal ions. *Polyhedron*, 2012, vol. 38, no. 1, p. 26-35.

43. Nockemann, P., *et. al*. Anionic Rare-Earth Thiocyanate Complexes as Building Blocks for Low-Melting Metal-Containing Ionic Liquids. *Journal of the American Chemical Society*, 2006, vol. 128, no. 42, p. 13658-13659.

44. Kishi, S.; Kato, M. Thermal and Photo Control of the Linkage Isomerism of Bis(thiocyanato)(2,2'-bipyridine)platinum(II). *Inorganic Chemistry*, 2003, vol. 42, p. 8728-8734.

45. Georgousis, Z. D., *et. al*. Synthesis, structural characterization and antioxidant/anti-inflammatory activity of pentacoordinated bis(isoselenocyanato) and bis(isothiocyanato) CuII and NiII complexes with Me5dien: Crystal structure of [Cu(Me5dien)(NCSe)2]. *Journal of Molecular Structure*, 2007, vol. 837, no. 1-3, p. 30-37.

46. Maria Kulandai Raja Balan, A., *et. al*. Mixed ligand complexes of nickel(II), copper(II) and zinc(II) with nicotinanilide and thiocyanate with some nickel(II), copper(II) and zinc(II) salt. *International Journal of Pharmaceutical and Life Sciences*, 2013, vol. 3, no. 2, p. 67-75.

47. Dobado, J. A., *et. al*. On the bonding isomerism in three-co-ordinated copper(I) thiocyanates. *Journal of the Chemical Society, Dalton Transactions*, 1999, vol. 3, p. 489-496.

48. Shurdha, E., *et. al*. First Row Transition Metal(II) Thiocyanate Complexes, and Formation of 1-, 2-, and 3-Dimensional Extended Network Structures of M(NCS)2(Solvent)2 (M = Cr, Mn, Co) Composition. *Inorganic Chemistry*, 2013, vol. 52, no. 18, p. 10583-10594.

49. Shurdha, E., *et. al*. Extended Network Thiocyanate- and Tetracyanoethanide-Based First-Row Transition Metal Complexes. *Inorganic Chemistry*, 2012, vol. 51, no. 18, p. 9655-9665.

50. Shurdha, E., *et. al*. Dinuclear [CoII(NCMe)5CoII(NCS)4] Possessing Octahedral and Tetrahedral CoII Sites. *Inorganic Chemistry*, 2011, vol. 50, no. 21, p. 10546-10548.

51. Zhang, H., *et. al*. Molecular and crystal engineering of a new class of inorganic cadmium-thiocyanate polymers with host–guest complexes as organic spacers, controllers, and templates. *Coordination Chemistry Reviews*, 1999, vol. 183, no. 1, p. 157-195.

52. *Inorganic Chemistry for Dummies*. Matson, M. L.; Orbaek, A. W. New Jersey: John Wiley and Sons, Inc., 2013. 384 p. ISBN 978-1-118-21794-8.

53. Buda, C., *et. al*. Stability Studies of Transition-Metal Linkage Isomers Using Quantum Mechanical Methods. Groups 11 and 12 Transition Metals. *Journal of Chemical Information Modeling*, 2005, vol. 45, no. 4, p. 965-970.

54. *Variety in Coordination Modes of Ligands in Metal Complexes*. Kawaguchi, S. Berlin Heidelberg: Springer-Verlag, 1988. 123 p. ISBN 978-3-642-50148-7.

55. Buckingham, D. A. The linkage isomerism of thiocyanate bonded to cobalt (III). *Coordination Chemistry Reviews*, 1994, vol. 135–136, p. 587-621.

56. Chiumia, G. C., *et. al*. Terminal S-coordinated thiocyanate in a nickel(II) complex.: X-ray structures of Ni(poph)(H2O)(SCN)(NCS) and Ni(poqh)(H2O)(NCS)2 (poph = 2-pyridinecarboxaldehyde 1-oxide 2′-pyridinylhydrazone, poqh = 2-pyridinecarboxaldehyde 1-oxide 2′-quinolynylhydrazone). *Inorganica Chimica Acta*, 1999, vol. 285, no. 2, p. 297-300.

57. *Principles of Descriptive Inorganic Chemistry*. Wulfsberg, G. United States of America: University Science Books, 1991. 461 p. ISBN 0-935702-66-0.

58. Hancock, R. D.; Martell, A. E. Hard and Soft Acid-Base Behavior in Aqueous Solution: Steric Effects Make Some Metal Ions Hard: A Quantitative Scale of Hardness-Softness for Acids and Bases. *Journal of Chemical Education*, 1996, vol. 73, no. 7, p. 654-661.

59. *Introduction to Modern Inorganic Chemistry*, 6th edition. MacKay, K. M.; MacKay, R. A.; Henderson, W. United Kingdom: Nelson Thrones Ltd, 2002. 612 p. ISBN 0-7487-6420-8.

60. Zhu, H., *et. al*. A blue luminescent di-2-pyridylamine cadmium complex with an unexpected arrangement of thiocyanate ligands: a supramolecular layered structure

based on hydrogen bonds and π–π stacking interactions. *Inorganic Chemistry Communications*, 2001, vol. 4, no. 10, p. 577-581.

61. Bose, D., *et. al*. Polymeric end-to-end bibridged cadmium(II)thiocyanates containing monodentate and bidentate N-donor organic blockers: supramolecular synthons based on π–π and/or C–H··π interactions. *Polyhedron*, 2004, vol. 23, no. 12, p. 2045-2053.

62. Hazari, A., *et. al*. The influence of H-bonding on the 'ambidentate' coordination behaviour of the thiocyanate ion to Cd(II): a combined experimental and theoretical study. *Dalton Transactions*, 2014, vol. 43, p. 8007-8015.

63. Kabešová, M.; Gažo, J. Structure and classification of thiocyanates and the mutual influence of their ligands. *Chemicke Zvesti (present Chemical Papers)*, 1980, vol. 34, no. 6, p. 800-841.

64. *Chemistry: Principles and Practise*, 3rd edition. Reger, D. L.; Goode, S. R.; Ball, D. W. Canada: Cengage Learning, 2010. 1120 p. ISBN-10: 0534420125, ISBN-13: 9780534420123.

65. Homanen, P., *et. al*. Ruthenium(II) Bipyridine Complexes: Synthesis and Characterization of Ru(bpy)(CO)2(SCN)2, Ru(dmbpy)(CO)2Cl2, and Ru(dmbpy)(CO)2(NCS)H (bpy = 2,2'-Bipyridine; dmbpy = 6,6'-Dimethyl-2,2'-bipyridine). *Organometallics*, 1996, vol. 15, no. 19, p. 4081-4084.

66. Kabešová, M., *et. al*. Bonding properties of thiocyanate groups in copper(II) and copper(I) complexes. *Coordination Chemistry Reviews*, 1995, vol. 140, p. 115-135.

67. Machura, B., *et. al*. Thiocyanate manganese(II) and cobalt(II) complexes of bis(pyrazol-1-yl)methane and bis(3,5-dimethylpyrazol-1-yl)methane – Syntheses, spectroscopic characterization, X-ray structure and magnetic properties. *Polyhedron*, 2013, vol. 56, p. 189-199.

68. Miezis, A. Infrared Studies on the Thiocyanate Ion and its Complexes with Palladium(II). *Acta Chemica Scandinavica*, 1973, vol. 27, p. 3746-3760.

69. Meng, X.-R., *et. al*. Influence of the anion on the coordination mode of an unsymmetrical N-heterocyclic ligand in Cd(II) complexes: From discrete molecule to one- and two-dimensional structures. *Polyhedron*, 2010, vol. 29, no. 13, p. 2619-2628.

70. Fu-Tai Tuan, D.; Reed, J. W. Studies of the linkage and bonding of triatomics in transition metal complexes: Part 2. NCS− complexes. *Journal of Molecular Structure*, 1991, vol. 232, p. 111-121.

71. Hush, N. S.; Reimers, J. R. Solvent Effects on the Electronic Spectra of Transition Metal Complexes. *Chemical Reviews*, 2000, vol. 100, no. 2, p. 775-786.

72. Ishiguro, S.-I., *et. al*. Solvent conformation and ion solvation: From molecular to ionic liquids. *Pure and Applied Chemistry*, 2006, vol. 78, no. 8, p. 1595-1609.

73. Šašić, S., *et. al*. Raman Spectra and Solvent-Solute Interaction of Mercury(II)-Thiocyanate Complexes in Some Aprotic Donor Solvents. *Spectroscopy Letters*, 1995, vol. 28, no. 8, p. 1217-1224.

74. Sancho, M. I., *et. al*. Spectroscopic Study of Solvent Effects on the Electronic Absorption Spectra of Flavone and 7-Hydroxyflavone in Neat and Binary Solvent Mixtures. *International Journal of Molecular Sciences*, 2011, vol. 12, 12, p. 8895-8912.

75. Šašić, S.; Antić-Jovanović, A.; Jeremić, M. An investigation of the equilibrium of mercury(II) thiocyanate complexes in DMF solutions via Raman spectra and factor

analysis. *Journal of the Chemical Society, Faraday Transactions*, 1998, vol. 94, no. 21, p. 3255-3260.

76. Šašić, S.; Jeremić, M.; Antić-Jovanović, A. Raman study of solvent–solute interactions in solutions of mercury(II)–thiocyanate complexes. *Journal of Raman Spectroscopy*, 1998, vol. 29, no. 4, p. 321-325.

77. Wöhlert, S.; Jess, I.; Näther, C. The influence of the metal cation and the N-donor ligand on the reactivity and structures of Cd and Zn coordination compounds with 3-bromopyridine and 3-chloropyridine. *Inorganica Chimica Acta*, 2013, vol. 407, p. 243-251.

78. Hsieh, C.-H., *et. al*. Ambidentate Thiocyanate and Cyanate Ligands in Dinitrosyl Iron Complexes. *Inorganic Chemistry*, 2013, vol. 52, no. 4, p. 2119-2124.

79. Lakshmi Reddy, S.; Endo, T.; Siva Reddy, G. *Electronic (Absorption) Spectra of 3d Transition Metal Complexes* [interactive] [2014-03-20]. Access: http://cdn.intechopen.com/pdfs-wm/38537.pdf

80. Ozutsumi, K., *et. al*. Complexation of Iron(III) with Thiocyanate Ions in Aqueous Solution. *Analytical Sciences*, 1992, vol. 8, no. 4, p. 521-526.

81. van Staden, J. F., *et. al*. Non-linearity with metal-metal ligand complex reactions in flow injection systems. Metal-thiocyanate reactions. *Analytica Chimica Acta*, 1997, vol. 350, no. 1-2, p. 37-50.

82. Capitan, M. J., *et. al*. Salt effects in the kinetics of the formation of the iron(III) thiocyanate complex. *Journal of the Chemical Society, Faraday Transactions 1: Physical Chemistry in Condensed Phases*, 1989, vol. 85, no. 12, p. 4193-4199.

83. Sultan, S. M.; Bishop, E. A study of the formation and stability of the iron(III)-thiocyanate complex in acidic media. *Analyst*, 1982, vol. 107, p. 1060-1064.

84. Korondán, I.; Nagypál, I. NMR relaxation studies in solutions of transition metal complexes. X. The stepwise equilibria in the iron(III)-thiocyanate system studied by NMR relaxation. *Inorganica Chimica Acta*, 1983, vol. 73, p. 131-134.

85. Ozutsumi, K., *et. al*. Structure of iron(III) and formation of iron(III) thiocyanato complexes in N,N-dimethylacetamide. *Polyhedron*, 1993, vol. 12, no. 18, p. 2185-2192.

86. Ozutsumi, K.; Kurihara, M.; Kawashima, T. Structure of iron(III) ion and its complexation with thiocyanate ion in N,N-dimethylformamide. *Talanta*, 1993, vol. 40, no. 5, p. 599-607.

87. Skorupa, A.; Korybut-Daszkiewicz, B.; Mroziński, J. Heteronuclear thiocyanate-bridged compounds of the type (NiL)3[M(NCS)6]2 (M=Fe(III), Cr(III); L=5,6,12,13-Me4-[14]-4,11-dieneN4). *Inorganica Chimica Acta*, 2002, vol. 336, p. 65-70.

88. Tomkiewicz, A.; Kłak, J.; Mroziński, J. Bimetallic complexes with macrocyclic ligands. Variation of magnetic exchange interactions in some heteronuclear thiocyanato-bridged compounds. *Materials Science-Poland*, 2004, vol. 22, p. 253-263.

89. Melendres, C. A.; O'Leary, T. J.; Solis, J. Effect of thiocyanate on the corrosion and passivation behaviour of copper and iron: laser Raman spectroscopy and photoelectrochemical studies. *Electrochimica Acta*, 1991, vol. 36, no. 3-4, p. 505-511.

90. Cao, P., *et. al*. Potential Dependence of the Orientation of Thiocyanate Adsorbed on an Iron Electrode as Probed by Surface-Enhanced Raman Spectroscopy. *The Journal of Physical Chemistry B*, 2002, vol. 106, no. 29, p. 7283-7285.

91. Ivšić, A. G.; Tamhina, B. Extraction and Formation of Iron(III) Thiocyanate Complexes: Application for Spectrophotometric Determination of Iron. *Croatica Chemica Acta*, 2003, vol. 76, no. 4, p. 323-328.

92. Wang, S., *et. al*. Separation of Iron(III) with Ammonium Thiocyanate-H2O-n-Propyl Alcohol Extraction System in the Presence of Sodium Chloride. *Journal-Chinese Chemical Society Taipei*, 2004, vol. 51, p. 707-712.

93. Barbosa-Filho, O.; Monhemius, A. J. Iodide—thiocyanate leaching system for gold. *Hydrometallurgy*, 1994, vol. 94, p. 425-440.

94. Broadhurst, J. L.; du Preez, J. G. H. A thermodynamic study of the dissolution of gold in an acidic aqueous thiocyanate medium using iron (III) sulphate as an oxidant. *Hydrometallurgy*, 1993, vol. 32, no. 3, p. 317-344.

95. Applicants Wan, R. Y.; Marc LeVier, K. *Precious metal recovery using thiocyanate lixiviant*. No. US7285256 B2, 2003-08-28.

96. Li, J., *et. al*. Thiocyanate hydrometallurgy for the recovery of gold. Part III: Thiocyanate stability. *Hydrometallurgy*, 2012, vol. 113-114, p. 19-24.

97. Li, J., *et. al*. Thiocyanate hydrometallurgy for the recovery of gold. Part IV: Solvent extraction of gold with Alamine 336. *Hydrometallurgy*, 2012, vol. 113-114, p. 25-30.

98. Nasri, H.; Debbabi, M. Synthesis, spectroscopic and structural characterization of the pentacoordinate high-spin Fe (III) isothiocyanate "picket fence" porphyrin complex. *Polyhedron*, 1998, vol. 17, no. 20, p. 3607-3612.

99. Manoussakis, G., *et. al*. Studies of Mixed-Ligand Complexes of Dithiocarbamato–Thiocyanato and Iron(III), Nickel(II), Copper(II) and Zinc(II). *European Journal of Medicinal Chemistry*, 1987, vol. 22, p. 421-425.

100. Raju, K. C.; Radhakrishnan, P.K. Complexes of Iron(III) with N,N′‐bis(4‐Antipyrylmethylidene)ethylenediamine. *Synthesis and Reactivity in Inorganic and Metal-Organic Chemistry*, 2003, vol. 33, no. 1, p. 23-33.

101. Nayak, S., *et. al*. Kinetics and Mechanism of the Formation of (1,5)bis(2-hydroxybenzamido)3- azapentaneiron(III) and its Reactions with Thiocyanate, Azide, Acetate, Sulfur(IV) and Ascorbic Acid in Solution, and the Synthesis and Characterization of (nitrato)bis- (2-hydroxybenzamido)3-azapentaneiron(III). The Role of Phenol–amide–amine Coordination. *Transition Metal Chemistry*, 2005, vol. 30, no. 8, p. 917-932.

102. Nayak, S.; Dash, A. C. Kinetics and mechanism of the formation of (1,8) bis (2-hydroxybenzamido)3,6-diazaoctaneiron(III) and its reactions with thiocyanate, azide, acetate, sulfur(IV) and ascorbic acid in solution, and the synthesis and characterization of a novel oxo bridged diiron(III) complex. The role of phenol–amide–amine coordination. *Transition Metal Chemistry*, 2006, vol. 31, no. 6, p. 813-828.

103. Ivanović-Burmazović, I.; Hamza, Mohamed S. A.; van Eldik, R. Solvent Tuning of the Substitution Behavior of a Seven-Coordinate Iron(III) Complex. *Inorganic Chemistry*, 2006, vol. 45, no. 4, p. 1575-1584.

104. Sarauli, D., *et. al*. Seven-Coordinate Iron Complex as a Ditopic Receptor for Lithium Salts: Study of Host−Guest Interactions and Substitution Behavior. *Inorganic Chemistry*, 1997, vol. 46, no. 19, p. 7848-7860.

105. Kojlo, A., *et. al.* Analytical study of the reaction of phenothiazines with some oxidants, metal ions, and organic substances. *Journal of Trace and Microprobe Techniques*, 2001, vol. 19, no. 1, p. 45-70.

106. *Environmental Chemistry and Toxicology of Mercury*. Liu, G.; Cai, Y.; O'Driscoll, N. New Jersey: John Wiley&Sons, Inc., 2010. 600 p. ISBN 978-0-470-57872-8.

107. Wang, E.-C., *et. al.* Three 2-Aminobenzothiazole-Based Mercury Complexes Tuned by Competitive Coordination Between the Coligands: Synthesis, Structures, and Fluorescent Properties. *Synthesis and Reactivity in Inorganic, Metal-Organic, and Nano-Metal Chemistry*, 2011, vol. 41, no. 7, p. 791-797.

108. Machura, B., *et. al.* Synthesis, spectroscopic investigations, X-ray studies and magnetic properties of novel three-dimensional thiocyanato-bridged manganese(II)–mercury(II) coordination polymers. *Polyhedron*, 2013, vol. 49, no. 1, p. 216-222.

109. Soldin, Ž., *et. al.* Role of the group 12 metals in tuning the structural motif: From complexes to halometallate salts of 3-carbamoyl-1-methylpyridinium. *Polyhedron*, 2013, vol. 52, p. 689-698.

110. Machura, B., *et. al.* Novel bimetallic thiocyanate-bridged Cu(II)–Hg(II) compounds—synthesis, X-Ray studies and magnetic properties. *Journal of Solid State Chemistry*, 2013, vol. 197, p. 218-227.

111. Ravi Kumar, S. M.; Selvakumar, S.; Sagayaraj, P. Synthesis, growth and physicochemical properties of an organometallic nonlinear optical crystal: Mercury cadmium chloride thiocyanate. *Optik – International Journal for Light and Electron Optics*, 2014, vol. 125, no. 3, p. 1071-1074.

112. Jagdish, P.; Rajesh, N. P. Effect of copper on the growth morphology and characterization of zinc mercury thiocyanate crystals. *Journal of Industrial and Engineering Chemistry*, 2012, vol. 18, no. 6, p. 2157-2161.

113. Vijayabhaskaran, B.; Ramachandra Raja, C. Influence of metallic substitution on the physical properties of nickel mercury thiocyanate nonlinear optical crystal. *Optik – International Journal for Light and Electron Optics*, 2013, vol. 124, no. 12, p. 1366-1368.

114. Machura, B., *et. al.* Heterobimetallic Mn(II)-Hg(II) polynuclear complexes containing Hg(SCN)42- unit : synthesis, spectroscopic investigations, X-ray studies and magnetic properties. *Polyhedron*, 2011, vol. 30, no. 15, p. 2499-2504.

115. Machura, B., *et. al.* Heterobimetallic Cu(II)–Hg(II) polynuclear complexes containing Hg(SCN)42− unit – Synthesis, spectroscopic investigations, X-ray studies and magnetic properties. *Polyhedron*, 2010, vol. 29, no. 8, p. 2023-2032.

116. Zhang, P., *et. al.* Theory studies on the linear and nonlinear optical properties of MnHg(SCN)4 crystal. *Optics Communications*, 2013, vol. 286, p. 322-328.

117. Ramesh, V., *et. al.* Growth, spectroscopic and physicochemical properties of bis mercury ferric chloride tetra thiocyanate: A nonlinear optical crystal. *Spectrochimica Acta Part A: Molecular and Biomolecular Spectroscopy*, 2013, vol. 108, p. 236-243.

118. Wang, X. Q., *et. al.* Spectroscopic and thermal properties of FeHg(SCN)4. *Thermochimica Acta*, 2004, vol. 414, no. 1, p. 53-58.

119. Li, C.-S., *et. al.* Synthesis, structure and magnetic properties of two μ-oxo and thiocyanato-bridged manganese(II)–mercury(II) coordination polymers. *Inorganica Chimica Acta*, 2007, vol. 360, no. 11, p. 3569-3574.

120. Khandar, A. A., *et. al*. One-dimensional ladder like and two-dimensional polymorphs of heterometallic thiocyanate bridged copper(II) and mercury(II) coordination polymer: Syntheses, structural, vibration, luminescence and EPR studies. *Inorganica Chimica Acta*, 2011, vol. 366, no. 1, p. 184-190.

121. Mahmoudi, G.; Morsali, A. Mercury(II) metal–organic coordination polymers with pyrazine derivatives. *CrystEngComm*. 2009, vol. 11, no. 9, p. 1868-1879.

122. Satapathi, S., *et. al*. Syntheses, structures and luminescence behaviors of mono- and dinuclear complexes of type [M(L)(NCS)2]n [M = Zn/Hg, n = 1; M = Cd, n = 2; L = (N,N-diethyl,N′-(pyridin-2-yl)benzylidene)ethane-1,2-diamine]: Variation of coordination matrices and nuclearities with the change of congeneric metal ions. *Polyhedron*, 2011, vol. 30, no. 2, p. 387-396.

123. Montazerozohori, M.; Sedighipoor, M.; Joohari, S. Electrochemical Behavior of bis((E) 3-(2-Nitrophenyl) Allylidene)Propane-1,2-Diamine as a New Schiff Base and Some Its New XII Group Complexes. *International Journal of Electrochemical Science*, 2012, vol. 7, p. 77-88.

124. Chattopadhyay, S., *et. al*. Synthesis, molecular and crystalline architectures, and properties of novel bis(bidentate) and bis(tridentate) Schiff base bridged dinuclear mercury(II)pseudohalides: Control of coordination numbers by varying denticities. *Polyhedron*, 2010, vol. 29, no. 6, p. 1667-1675.

125. Mahmoudi, G.; Morsali, A. Three new HgII metal–organic polymers generated from 1,4-bis(n-pyridyl)-3,4-diaza-2,4-hexadiene ligands. *Inorganica Chimica Acta*, 2009, vol. 362, no. 9, p. 3238-3246.

126. Khandar, A. A., *et. al*. Syntheses, studies and crystal structures of coordination polymers and dinuclear complexes of mercury(II) halides and thiocyanate with a symmetrical Schiff base ligand. *Inorganica Chimica Acta*, 2013, vol. 394, p. 36-44.

127. Đaković, M., *et. al*. Thiocyanate complexes of the group 12 metals with pyridine-2-carboxamide: Synthesis and structural characterization. *Polyhedron*, 2008, vol. 27, no. 1, p. 210-222.

128. Kharat, A. N.; Bakhoda, A.; Zamanian, S. Synthesis and structural studies of some fluorescent group XII metal complexes with a terpyridine based ligand. *Polyhedron*, 2011, vol. 30, no. 6, p. 1134-1142.

129. Mahmoudi, G.; Morsali, A.; Zeller, M. Mercury(II) acetate/thiocyanate coordination polymers with n-donor ligands, spectroscopic, thermal and structural studies. *Inorganica Chimica Acta*, 2009, vol. 362, no. 1, p. 217-225.

130. Kongsted, J., *et. al*. Solvent effects on the electronic absorption spectrum of camphor using continuum, discrete or explicit approaches. *Chemical Physics Letters*, 2010, 484 (4-6), 185-191.

131. Zakerhamidi, M. S.; Ghanadzadeh, A.; Moghadam, M. Solvent Effects on the UV/ Visible Absorption Spectra of Some Aminoazobenzene Dyes. *Chemical Science Transactions*, 2012, vol. 1, no. 1, p. 1-8.

132. Homocianu, M., *et. al*. Solvent Effects on the Electronic Absorption and Fluorescence Spectra. *International Journal of Advanced Applied Physics Research*, 2011, vol. 2, no. 1, p. 1-9.

133. Sancho, M. I., *et. al*. Spectroscopic Study of Solvent Effects on the Electronic Absorption Spectra of Flavone and 7-Hydroxyflavone in Neat and Binary Solvent

Mixtures. *International Journal of Molecular Sciences*, 2011, vol. 12, no. 12, p. 8895-8912.

134. Orozco, M.; Luque, F. J. Theoretical Methods for the Description of the Solvent Effect in Biomolecular Systems. *Chemical Reviews*, 2000, vol. 100, no. 11, p. 4187-4225.

135. *Solvation Effects on Molecules and Biomolecules. Computational Methods and Applications*. Challenges and Advances in Computational Chemistry and Physics, vol. 6. Canuto, S. Springer, 2008. 536 p. ISBN 978-1-4020-8269-6.

136. Adamo, C.; Jacquemin, D. The calculations of excited-state properties with Time-Dependent Density Functional Theory. *Chemical Society Reviews*, 2013, vol. 42, no. 3, p. 845-856.

137. Bizzarri, A. R.; Cannistraro, S. Molecular Dynamics of Water at the Protein−Solvent Interface. *The Journal of Physical Chemistry B*, 2002, vol. 106, no. 26, p. 6617-6633.

138. Wang, L.-P.; van Voorhis, T. A Polarizable QM/MM Explicit Solvent Model for Computational Electrochemistry in Water. *Journal of Chemical Theory and Computation*, 2012, vol. 8, no. 2, p. 610-617.

139. Cappelli, C.; Mennucci, B.; Monti, S. Environmental Effects on the Spectroscopic Properties of Gallic Acid: A Combined Classical and Quantum Mechanical Study. *The Journal of Physical Chemistry A*, 2005, vol. 109, no. 9, p. 1933-1943.

140. Kim, J., *et. al*. Tight β-turns in peptides. DFT-based study of infrared absorption and vibrational circular dichroism for various conformers including solvent effects. *Theoretical Chemistry Accounts*, 2008, vol. 119, no. 1-3, p. 81-97.

141. Kubelka, J.; Huang, R.; Keiderling, T. A. Solvent Effects on IR and VCD Spectra of Helical Peptides: DFT-Based Static Spectral Simulations with Explicit Water. *The Journal of Physical Chemistry B*, 2005, vol. 109, no. 16, p. 8231-8243.

142. Kato, M., *et. al*. Electronic structure calculation study of metal complexes with a phytosiderophore mugineic acid. *Inorganica Chimica Acta*, 2011, vol. 370, no. 1, p. 304-310.

143. *Handbook of Raman Spectroscopy*. Lewis, I. R.; Edwards, Howell G. M. United States of America: Marcel Dekker, Inc., 2001. 1056 p. ISBN 0-8247-0557-2.

144. *Introductory Raman Spectroscopy,* 2nd Edition. Ferraro, J. R.; Nakamoto, K.; Brown, C. W. United States of America: Academic Press, 2003. 434 p. ISBN 0-12-254105-7.

145. *Modern Spectroscopy,* 4th Edition. Hollas, J. M. England: John Wiley & Sons Ltd, 2004. 452 p. ISBN 0-470-84416-7.

146. Senvaitienė, J.; Lukšėnienė, J.; Vedrickienė, L. J. *Muziejinių eksponatų priežiūra. I dalis. Meno kūrinių technikos ir tyrimai*. Vilnius, 2008, 364 p.

147. Upadhyay, G., *et. al*. Solvent dependent frequency shift and Raman noncoincidence effect of S=O stretching mode of Dimethyl sulfoxide in liquid binary mixtures. *Spectrochimica Acta Part A: Molecular and Biomolecular Spectroscopy*, 2013, vol. 109, p. 239-246.

148. Lenchenkov, V.; She, C.; Lian, T. Vibrational Relaxation of CN Stretch of Pseudo-Halide Anions (OCN-, SCN-, and SeCN-) in Polar Solvents. *The Journal of Physical Chemistry B*, 2006, vol. 110, no. 40, p. 19990-19997.

149. Schultz, P. W.; Leroi, G. E.; Harrison, J. F. Ab initio calculations of ionic and hydrogen bonding interactions with the OCN-, SCN- and SeCN- anions. *Molecular Physics*, 1996, vol. 88, no. 1, p. 217-246.

150. *Infrared and Raman Characteristic Group Frequencies: tables and charts*, 3rd edition. Socrates, G. England: John Wiley & Sons Ltd., 2001. 347 p. ISBN 0-470-09307-2.

151. Herber, R. H. *Variable Temperature FTIR Spectroscopy of Transition Metal Complexes Using the SCN Reporter Ligand*, June 19, 1989, Fairfax, VA. Proc. SPIE 1145, 7th International Conference on Fourier Transform Spectroscopy, 463 doi:10.1117/12.969550.

152. Diaz Fleming, G., *et. al*. Theoretical surface-enhanced Raman spectra study of substituted benzenes: I. Density functional theoretical SERS modelling of benzene and benzonitrile. *Spectrochimica Acta Part A: Molecular and Biomolecular Spectroscopy*, 2008, vol. 71, no. 3, p. 1049-1055.

153. Riauba, L., *et. al*. A Study of Cysteamine Ionization in Solution by Raman Spectroscopy and Theoretical Modeling. *The Journal of Physical Chemistry A*, 2006, vol. 110, no. 50, p. 13394–13404.

154. Többens, D. M.; Kahlenberg, V. Improved DFT calculation of Raman spectra of silicates. *Vibrational Spectroscopy*, 2011, vol. 56, no. 2, p. 265-272.

155. Jamróz, M. H. Vibrational Energy Distribution Analysis (VEDA): Scopes and limitations. *Spectrochimica Acta Part A: Molecular and Biomolecular Spectroscopy*, 2013, vol. 114, p. 220-230.

156. McCamant, D. W.; Kukura, P.; Mathies, R. A. Femtosecond Broadband Stimulated Raman: A New Approach for High-Performance Vibrational Spectroscopy. *Applied Spectroscopy*, 2003, vol. 57, no. 11, p. 1317-1323.

157. Reber, C. Absorption and luminescence spectroscopy of transition metal compounds: from coordination geometries to excited-state properties. *Canadian Journal of Analytical Sciences and Spectroscopy*, 2008, vol. 53, no. 3, p. 91-101.

158. Vlček, A.; Záliš, Jr. S. Modeling of charge-transfer transitions and excited states in d^6 transition metal complexes by DFT techniques. *Coordination Chemistry Reviews*, 2007, vol. 251, no. 3-4, p. 258-287.

159. Daniel, C. Electronic spectroscopy and photoreactivity in transition metal complexes. *Coordination Chemistry Reviews*, 2003, vol. 238-239, p. 143-166.

160. González, L.; Escudero, D.; Serrano-Andrés, L. Progress and Challenges in the Calculation of Electronic Excited States. *A European Journal of Chemical Physics and Physical Chemistry*, 2012, vol. 13, no. 1, p. 28-51.

161. Bossert, J.; Daniel, C. Electronic absorption spectroscopy of $[Ru(phen)_2(bpy)]^{2+}$, $[Ru(phen)_2(dmbp)]^{2+}$, $[Ru(tpy)(phen)(CH_3CN)]^{2+}$ and $[Ru(tpy)(dmp)(CH_3CN)]^{2+}$: A theoretical study. *Coordination Chemistry Reviews*, 2008, vol. 252, no. 23-24, p. 2493-2503.

162. Gorelsky, S. I.; Lever, A. B. P. The Electronic Structure and Spectra of $[Ru(NH_3)_4(LL)]^{2+}$ (LL=bpy, bpz, bqdi) studied by Density Functional Theory and INDO/S. Charge Transfer Character of Electronic Transitions and their Solvatochromism. *Canadian Journal of Analytical Sciences and Spectroscopy*, 2003, vol. 48, no. 1, p. 1-12.

163. The GRAMS spectroscopy software for visualizing, processing and managing spectroscopy data www.thermoscientific.com.

164. The Chemcraft graphical program for working with quantum chemistry computations www.chemcraftprog.com.

165. Gaussian 03, Revision D.01, Frisch, M. J.; Trucks, G. W.; Schlegel, H. B.; Scuseria, G. E.; Robb, M. A.; Cheeseman, J. R.; Montgomery Jr., J. A.; Vreven, T.; Kudin, K. N.; Burant, J. C.; Millam, J. M.; Iyengar, S. S.; Tomasi, J.; Barone, V.; Mennucci, B.; Cossi, M.; Scalmani, G.; Rega, N.; Petersson, G. A.; Nakatsuji, H.; Hada, M.; Ehara, M.; Toyota, K.; Fukada, R.; Hasegawa, J.; Ishida, M.; Nakajima, T.; Honda, Y.; Kitao, O.; Nakai, H.; Klene, M.; Li, X.; Know, J. E.; Hratchian, H. P.; Cross, J. B.; Adamo, C.; Jaramillo, J.; Gomperts, R.; Stratmann, R. E.; Yazyev, O.; Austin, A. J.; Cammi, R.; Pomelli, C.; Ochterski, J. W.; Ayala, P. Y.; Morokuma, K.; Voth, G. A.; Salvador, P.; Dannenburg, J. J.; Zakrzewski, V. G.; Dapprich, S.; Daniels, A. D.; Strain, M. C.; Farkas, O.; Malick, D. K.; Rabuck, A. D.; Raghavachari, K.; Foresman, J. B.; Ortiz, J. V.; Liashenko, A.; Piskorz, P.; Komaromi, I.; Martin, R. L.; Fox, D. J.; Keith, T.; Al-Laham, M. A.; Peng, C. Y.; Nanayakkara, A.; Challacombe, M.; Gill, P. M. W.; Johnson, B.; Chen, W.; Wong, M. W.; Gonzalez, C.; and Pople, J. A.; Gaussian, Inc., Wallingford, CT, 2004.

166. Becke, A. D. Density-functional thermochemistry. III. The role of exact exchange. *The Journal of Chemical Physics*, 1993, vol. 98, no. 7, p. 5648-5652.

167. Lee, C.; Yang, W.; Parr, R. G. Development of the Colle-Salvetti Correlation-Energy Formula into a Functional of the Electron Density. *Physical Review B*, 1988, vol. 37, p. 785-789.

168. Perdew, J. P.; Burke, K.; Ernzerhof, M. Generalized Gradient Approximation Made Simple. *Physical Review Letters*, 1997, vol. 78, p. 1396.

169. Zakharov, I. I., *et. al*. DFT-based thermodynamics of fenton reactions rejects the 'pure' aquacomplex models. *Computational and Theoretical Chemistry*, 2011, vol. 964, no. 1-3, p. 94-99.

170. Francl, M. M., *et. al*. Self-Consistent Molecular Orbital Methods. 23. A Polarization Basis Set for Second Row Elements. *Journal Chemical Physics*, 1982, vol. 77, p. 3654-3665.

171. Dolg, M., *et. al*. Energy-adjusted ab initio pseudopotentials for the first row transition elements. *Journal Chemical Physics*, 1987, vol. 86, p. 866-872.

172. Cossi, M., *et. al*. Energies, structures, and electronic properties of molecules in solution with the C-PCM solvation model. *Journal of Computational Chemistry*, 2003, vol. 24, no. 6, p. 669-681.

173. Küchle, W., *et. al*. Ab initio pseudopotentials for Hg through Rn. I. Parameter sets and atomic calculations. *Molecular Physics*, 1991, vol. 74, no. 6, p. 1245-1263.

174. Jamróz, M. H. Vibrational Energy Distribution Analysis VEDA 4, Warsaw, 2004-2010.

175. Merrick, J. P.; Moran, D.; Radom, L. An Evaluation of Harmonic Vibrational Frequency Scale Factors. *The Journal of Physical Chemistry A*, 2007, vol. 111, no. 45, p. 11683-11700.

176. Yanai, T.; Tew, D.; Handy, N. A new hybrid exchange–correlation functional using the Coulomb-attenuating method (CAM-B3LYP). *Chemical Physics Letters*, 2004, vol. 393, no. 1-3, p. 51-57.

177. Perdew, J. P.; Burke, K.; Ernzerhof, M. Generalized Gradient Approximation Made Simple. *Chemical Physics Letters*, 1996, vol. 77, p. 3865.

178. Gaussian 09, Revision A.02, Frisch, M. J.; Trucks, G. W.; Schlegel, H. B.; Scuseria, G. E.; Robb, M. A.; Cheeseman, J. R.; Scalmani, G.; Barone, V.; Mennucci, B.; Petersson, G. A.; Nakatsuji, H.; Caricato, M.; Li, X.; Hratchian, H. P.; Izmaylov, A. F.; Bloino, J.; Zheng, G.; Sonnenberg, J. L.; Hada, M.; Ehara, M.; Toyota, K.; Fukuda, R.; Hasegawa, J.; Ishida, M.; Nakajima, T.; Honda, Y.; Kitao, O.; Nakai, H.; Vreven, T.; Montgomery, J. A.; Peralta, Jr., J. E.; Ogliaro, F.; Bearpark, M.; Heyd, J. J.; Brothers, E.; Kudin, K. N.; Staroverov, V. N.; Kobayashi, R.; Normand, J.; Raghavachari, K.; Rendell, A.; Burant, J. C.; Iyengar, S. S.; Tomasi, J.; Cossi, M.; Rega, N.; Millam, J. M.; Klene, M.; Knox, J. E.; Cross, J. B.; Bakken, V.; Adamo, C.; Jaramillo, J.; Gomperts, R.; Stratmann, R. E.; Yazyev, O.; Austin, A. J.; Cammi, R.; Pomelli, C.; Ochterski, J. W.; Martin, R. L.; Morokuma, K.; Zakrzewski, V. G.; Voth, G. A.; Salvador, P.; Dannenberg, J. J.; Dapprich, S.; Daniels, A. D.; Farkas, Ö.; Foresman, J. B.; Ortiz, J. V.; Cioslowski, J.; and Fox, D. J.; Gaussian, Inc., Wallingford CT, 2009.

179. Trembleau, L.; Smith, T. A. D.; Abdelrahman, M. H. Receptor conformational change induces fluoride binding despite competitive water binding. *Chemical Communications*, 2013, vol. 49, p. 5850-5852.

180. Clever, H. L.; Johnson, S. A.; Derrick, M. E. The solubility of Mercury and Some Sparingly Soluble Mercury Salts in Water and Aqueous Electrolyte Solutions. The *Journal of Physical Chemistry*, 1985, vol. 14, no. 3, p. 631-680.

181. *Physical Methods in Chemistry and Nano Science*. Barron, A. R. Houston: Connexions, Rice University, 2012. 702 p. ISBN 978-1-300-0654-4-9.

182. Torreggiani, A., *et. al*. Raman study of in vivo synthesized Zn(II)-metallothionein complexes: structural insight into metal clusters and protein folding. *Biopolymers*, 2008, vol. 89, no. 12, p. 1114-1124.

183. Carey, P. R.; Dong, J. Following Ligand Binding and Ligand Reactions in Proteins via Raman Crystallography. *The Journal of Biochemistry*, 2004, vol. 43, no. 28, p. 8885-8893.

184. Niaura, G.; Malinauskas, A. Surface-enhanced Raman spectroscopy of ClO4- and SO42- anions adsorbed at a Cu electrode. *Journal of the Chemical Society, Faraday Transactions*, 1998, vol. 94, no. 15, p. 2205-2211.

185. Knittle, E.; Phillips, W.; Williams, Q. An infrared and Raman spectroscopic study of gypsum at high Pressures. *Physics and Chemistry of Minerals*, 2001, vol. 28, p. 630-640.

186. Lund Myhre, C. E., *et. al*. Spectroscopic Study of Aqueous H2SO4 at Different Temperatures and Compositions: Variations in Dissociation and Optical Properties. *The Journal of Physical Chemistry A*, 2003, vol. 107, p. 1979-1991.

187. Čejka, J., *et. al*. A vibrational spectroscopic study of hydrated Fe3+ hydroxyl-sulfates; polymorphic minerals butlerite and parabutlerite. *Spectrochimica Acta Part A: Molecular and Biomolecular Spectroscopy*, 2011, vol. 79, no. 5, p. 1356-1363.

188. Mink, J., *et. al*. Infrared and Raman spectroscopic and theoretical studies of hexaaqua metal ions in aqueous solution. *Journal of Molecular Structure*, 2003, vol. 661-662, p. 141-151.

189. Malek, K.; Kozłowski, H.; Proniewicz, L. M. Interaction of Na(I), Ni(II) and Cu(II) with 2-cyano-2-(hydroxyimino)acetic acid: Spectroscopic and theoretical studies. *Polyhedron*, 2005, vol. 24, no. 10, p. 1175-1184.

190. Harris, J. D., *et. al.* Synthesis and characterization of anionic transition metal isothiocyanate complexes prepared from metal powders and thiourea. *Inorganica Chimica Acta*, 2002, vol. 338, p. 99-104.

191. Scheidt, W. R., *et. al.* Preparation and molecular stereochemistry of six-coordinate (isothiocyanato)(pyridine)(porphinato)iron(III) complexes. (Isothiocyanato)(meso-tetraphenylporphinato)(pyridine)iron(III), a low-spin complex with a nonlinear FeNCS group, and (isothiocyanato)(octaethylporphinato)(pyridine)iron(III), a high-spin complex with nonequivalent axial ligands. *Journal of the American Chemical Society*, 1982, vol. 104, no. 12, p. 3367-3374.

192. Zhang, J. Y.; Wang, L.; Liu, Y. μ-Oxido-bis[bis(phenanthroline-κ2N,N')(sulfato-κ O)iron(III)] octahydrate. *Acta Crystallographica Section E*, 2011, E67 m1568-1569 doi:10.1107/S1600536811042723.

193. Horn Jr., A., *et. al.* Synthesis, molecular structure and spectroscopic, electrochemical and magnetic properties of a new dinuclear iron complex containing μ-sulfate-di-μ-alkoxo bridges: evaluating the influence of the sulfate bridge on the physicochemical properties of the di-μ-alkoxo-diiron unit. *Journal of the Brazilian Chemical Society*, 2006, vol. 17, no. 8, p. 1584-1593.

194. Armentano, D., *et. al.* Syntheses, Crystal Structures, and Magnetic Properties of the Oxalato-Bridged Mixed-Valence Complexes [FeII(bpm)3]2[FeIII2(ox)5]·8H2O and FeII(bpm)3Na(H2O)2Fe(ox)3·4H2O (bpm = 2,2'-Bipyrimidine). *Inorganic Chemistry*, 2001, vol. 40, no. 4, p. 655-660.

195. Stefánsson, A.; Lemke, K. H.; Seward, T. M. *Iron(III) complexation in hydrothermal solutions – An experimental and theoretical study* : *Proceedings of ICPWS XV*, September 8–11, 2008, Berlin. 7 p. http://www.15icpws.de/papers/09_Geo-05_stefansson.pdf.

196. Person, I.; Iverfeldt, Å.; Ahrland, S. An X-Ray Diffraction and Raman Study of Mercury(II), Cadmium(II) and Zinc(II) Thiocyanate Complexes in Dimethylsulfoxide Solution. *Acta Chemica Scandinavica A*, 1981, vol. 35, p. 295-304.

197. *Challenges in Molecular Structure Determination*. Reichenbächer, M.; Popp, J. Berlin: Springer-Verlag Berlin Heidelberg, 2012. 482 p. ISBN 978-3-642-24389-9.

198. *Vibrational Spectroscopy, Theory and Applications*. Sathyanarayana, D. N. New Delhi: New Age International (P) Ltd., Publishers, 2004. 716 p. ISBN 81-224-1517-2.

199. Yamaguchi, T.; Yamamoto, K.; Ohtaki, H. X-Ray Diffraction, Raman, and NMR Studies on Tetrathiocyanato Complexes of Zinc(II), Cadmium(II), and Mercury(II) Ions in Aqueous Solution. *Bulletin of the Chemical Society of Japan*, 1985, vol. 58, no. 11, p. 3235-3243.

200. Taylor, K. A.; Long, T. V.; Plane, R. A. Raman Intensity Study of Zn (II), Cd (II), and Hg (II) Thiocyanate Complexes in Aqueous Solutions. *The Journal of Chemical Physics*, 1967, vol. 47, no. 138, p. 138-142.

201. Jaworski, A.; Stojek, Z.; Osteryoung, J. G. Oxidation of mercury microelectrodes in complexing media in the presence and absence of supporting electrolyte: Formation of thiocyanate complexes. *Journal of Electroanalytical Chemistry*, 2003, vol. 558, p. 141-153.

202. *Chemistry: The practical science*. Kelter, P.; Mosher, M.; Scott, A. United States of America: Houghton Mifflin Company, 2008. p. ISBN-10 0-547-05393-2, ISBN-13 978-0-547-05393-6.

LIST OF PUBLICATIONS ON THE THEME OF THIS DISSERTATION

Publications corresponding to the list of the Institute of Science Information (ISI) database:

1. **Elijošiutė, Erika;** Eicher-Lorka, Olegas; Griškonis, Egidijus; Matulaitienė, Ieva; Jankūnaitė, Dalia; Denafas, Gintaras. Molecular structure of mercury(II) thiocyanate complexes based on DFT calculations and experimental UV-electron spectroscopy and Raman studies // Spectrochimica Acta Part A : Molecular and Biomolecular Spectroscopy. Oxford : Pergamon-Elsevier Science. ISSN 1386-1425. 2013, Vol. 115, p. 574-582. [Science Citation Index Expanded (Web of Science)]. [0,236]. [IF (E): 1,977 (2012)].

2. **Elijošiutė, Erika;** Eicher-Lorka, Olegas; Griškonis, Egidijus; Kuodis, Zenonas; Jankūnaitė, Dalia; Denafas, Gintaras. Spectroscopic and structural investigations of iron(III) isothiocyanates. A comparative theoretical and experimental study // Spectrochimica Acta Part A : Molecular and Biomolecular Spectroscopy. Oxford : Pergamon-Elsevier Science. ISSN 1386-1425. 2014, Vol. 129, p. 43-51. [Science Citation Index Expanded (Web of Science)]. [0,236]. [IF (E): 1,977 (2012)].

Publications in peer-reviewed journals and conferences:

1. **Elijošiutė, Erika;** Griškonis, Egidijus; Jankūnaitė, Dalia; Denafas, Gintaras. Determination of mercury(I) and mercury(II) in binary aqueous mixtures using titrimetric analysis // CRETE 2012 : 3rd International Conference on Industrial and Hazardous Waste Management, 12 - 14 September, 2012, Chania, Greece. Chania : Technical University of Crete, 2012. ISBN 9789608475175. p. 1-8.

2. **Elijošiutė, Erika;** Eicher-Lorka, Olegas; Griškonis, Egidijus; Jankūnaitė, Dalia; Denafas, Gintaras. Intrinsic view of $[Hg(SCN)_n]^{2-n}$ molecules in the aqueous solution: DFT calculations and Raman spectroscopic study // Nanochemistry and Nanomaterials : International Conference of Young Chemists, December 7-9, 2012, Palanga, Lithuania : book of abstracts. Vilnius : Vilniaus universiteto leidykla, 2012. ISBN 9786094591389. p. 24.

3. **Elijošiutė, Erika;** Eicher-Lorka, Olegas; Griškonis, Egidijus; Jankūnaitė, Dalia; Denafas, Gintaras. Structural investigation of $[Hg(SCN)_n]^{2-n}$ complexes in water and heavy water solutions by raman spectroscopy and theoretical modeling // Open Readings 2013 = Laisvieji skaitymai 2013 : 56th scientific conference for young students of physics and natural sciences, March 20-23, 2013, Vilnius, Lithuania : programme and abstracts / Faculty of physics, Vilnius University. Vilnius : Vilnius University. ISSN 2029-4425. 2013, p. 95.

4. **Elijošiutė, Erika;** Eicher-Lorka, Olegas; Matulaitienė, Ieva; Griškonis, Egidijus; Jankūnaitė, Dalia; Denafas, Gintaras. Raman spectroscopic study of aqueous mixture of mercury(II) and iron(III) thiocyanates // 11-oji Lietuvos chemikų tarptautinė konferencija [elektroninis išteklius] : Vilnius, 2013 m. rugsėjo 27 d. = 11th International conference of Lithuanian chemists, Vilnius, September 27, 2013 / VMTI fizinių ir technologijos mokslų centro Chemijos institutas, Vilniaus universitetas, Lietuvos mokslų akademija. [S.l. : s.n.], 2013. ISBN 97860995511. p. [1].

5. **Elijošiutė, Erika;** Eicher-Lorka, Olegas; Griškonis, Egidijus; Jankūnaitė, Dalia; Denafas, Gintaras. UV titration of Hg(II) in fenton reagent solution // EcoBalt 2013 : 18th international scientific conference, October 25-27, 2013 Vilnius, Lithuania : book of abstracts. Vilnius : Vilniaus universiteto leidykla, 2013. ISBN 9786094592416. p. 25.

6. **Elijošiutė, Erika; Elijošiutė, Erika;** Eicher-Lorka, Olegas; Kuodis, Zenonas; Griškonis, Egidijus; Jankūnaitė, Dalia; Denafas, Gintaras. Investigation of iron(III)monoisothiocyanate in acidic aqueous solution by Raman spectroscopy and DFT calculation // ChemCYS2014 : Chemistry Conference for Young Scientists, February 27-28, 2014 Blankenberge, Belgium : book of abstracts. p. 313.

ACKNOWLEDGEMENTS

CURRICULUM VITAE

Name, Surname: Erika Elijošiutė
Date and place of birth: 16th of August, 1985, Pakruojis, Lithuania
Nationality: Lithuanian
Address, E-mail: Pramonės pr. 42-25, Kaunas, Lithuania
erika.elijosiute@ktu.lt
Education:

2010–2014   Kaunas University of Technology (KTU), Faculty of Chemical Technology, Department of Environmental Engineering, Doctoral studies in the field of Chemistry (03 P)

2008–2010   Kaunas University of Technology (KTU), Faculty of Chemical Technology, Department of Environmental Engineering, Master of Environmental Engineering

2004–2008   Vytautas Magnus University, Faculty of Natural Sciences. Bachelor of Ecology

1992–2004   Lygumai secondary school, Pakruojis district

Experience:

2013–now   Kaunas University of Technology (KTU), Faculty of Chemical Technology, Department of Environmental Engineering, laboratory assistant

Fields of interest:

Inorganic chemistry, analytical chemistry, environmental chemistry, quantum chemistry.

LIST OF ANNEXES

ANNEX 1. Calculated and experimental vibrational assignments of $[Fe(NCS)]^{2+}$ complex in the different hypothetical cases by B3LYP method. Theoretical assignments are based on detailed PED analysis. Abbreviations: ν – stretching; ν_{as} – asymmetric stretching; ν_s – symmetric stretching; σ – deformation; σ_{sci} – scissoring deformation; σ_t – twisting deformation; σ_w – wagging deformation; γ – out-of-plane deformation

Calculated								Approximate description	Experimental
SO_4^{2-} ligand is beside the NCS^- ligand				SO_4^{2-} ligand is on the opposite of the NCS^- ligand					
explicitly solvated		explicitly-implicitly solvated		explicitly solvated		explicitly-implicitly solvated			
Wavenumber H_2O (D_2O), cm^{-1}	Band assignments in H_2O, PED %	Wavenumber H_2O (D_2O), cm^{-1}	Band assignments in H_2O, PED %	Wavenumber H_2O (D_2O), cm^{-1}	Band assignments in H_2O, PED %	Wavenumber H_2O (D_2O), cm^{-1}	Band assignments in H_2O, PED %		Wavenumber H_2O (D_2O), cm^{-1}
3882 (2848)	100 ν_{as}O−H	3555 (2609)	99 ν_{as}O−H	3873 (2839)	100 ν_{as}O−H	3548 (2603)	93 ν_{as}O−H	bound H_2O	
3856 (2824)	99 ν_{as}O−H	3548 (2603)	99 ν_{as}O−H	3868 (2833)	100 ν_{as}O−H	3544 (2601)	92 ν_{as}O−H	bound H_2O	
3853 (2806)	99 νO−H	3545 (2601)	99 ν_{as}O−H	3841 (2798)	100 νO−H	3539 (2595)	100 ν_{as}O−H	bound H_2O	
3760 (2709)	100 ν_sO−H	3495 (2520)	91 ν_sO−H	3748 (2703)	100 ν_sO−H	349 (2516)	90 ν_sO−H	bound H_2O	
3721 (2685)	100 ν_sO−H	3486 (2512)	99 νO−H	3735 (2695)	100 ν_sO−H	3482 (2510)	99 ν_sO−H	bound H_2O	
3194 (2326)	99 νO−H	3483 (2510)	96 νO−H	3246 (2362)	98 νO−H	3479 (2507)	88 ν_sO−H	bound H_2O	
2064 (2064)	88 νN=C + 11 νC=S	2059 (2059)	92 νN=C	2057 (2057)	88 νN=C + 12 νC=S	2050 (2050)	92 νN=C	NCS	2067 (2061)
1652 (1202)	74 σ_{sci}H−O−H	1549 (1136)	88 σ_{sci}H−O−H	1658 (1207)	89 σ_{sci}H−O−H	1549 (1135)	89 σ_{sci}H−O−H	bound H_2O	
1621 (1186)	90 σ_{sci}H−O−H	1543 (1132)	88 σ_{sci}H−O−H	1625 (1190)	83 σ_{sci}H−O−H	1544 (1133)	92 σ_{sci}H−O−H	bound H_2O	

Calculated								Approximate description	Experimental
SO_4^{2-} ligand is beside the NCS^- ligand				SO_4^{2-} ligand is on the opposite of the NCS^- ligand					
explicitly solvated		explicitly-implicitly solvated		explicitly solvated		explicitly-implicitly solvated			
Wavenumber H_2O (D_2O), cm^{-1}	Band assignments in H_2O, PED %	Wavenumber H_2O (D_2O), cm^{-1}	Band assignments in H_2O, PED %	Wavenumber H_2O (D_2O), cm^{-1}	Band assignments in H_2O, PED %	Wavenumber H_2O (D_2O), cm^{-1}	Band assignments in H_2O, PED %		Wavenumber H_2O (D_2O), cm^{-1}
1592 (1168)	90 σ_{sci}H−O−H	1539 (1131)	94 σ_{sci}H−O−H	1610 (1180)	81 σ_{sci}H−O−H	1543 (1132)	90 σ_{sci}H−O−H	bound H_2O	
1300 (1300)	94 ν_{as}S=O	1183 (1183)	97 ν_{as}S=O	1289 (1289)	100 ν_{as}S=O	1186 (1186)	97 ν_{as}S=O	bound SO_4^{2-}	1139 (1139)
1084 (1081)	86 ν_sS=O	1091 (1091)	89 ν_sS=O	1092 (1089)	100 ν_sS=O	1094 (1093)	88 ν_sS=O	bound SO_4^{2-}	1039[*] (1039[*])
964 (707)	77 σ_tH−O−H								
947 (947)	74 νC=S + 19 νFe−N	898 (898)	79 νC=S + 17 νFe−N	954 (951)	41 νC=S + 10 νFe−N + 33 σ_tH−O−H	902 (902)	76 νC=S + 17 νFe−N	NCS	750 (750)
				946	29 νC=S + 47 σ_tH−O−H				
832 (830)	82 ν_sS−O	868 (868)	82 νS−O	851 (849)	76 νS−O	883 (882)	79 νS−O	bound SO_4^{2-}	
805 (802)	66 νS−O + 10 γO−S=2O	833 (832)	79 νS−O	805 (800)	77 νS−O	829 (829)	83 νS−O	bound SO_4^{2-}	

ANNEX 1. continued

Calculated								Approximate description	Experimental
SO_4^{2-} ligand is beside the NCS^- ligand				SO_4^{2-} ligand is on the opposite of the NCS^- ligand					
explicitly solvated		explicitly-implicitly solvated		explicitly solvated		explicitly-implicitly solvated			
Wavenumber H_2O (D_2O), cm^{-1}	Band assignments in H_2O, PED %	Wavenumber H_2O (D_2O), cm^{-1}	Band assignments in H_2O, PED %	Wavenumber H_2O (D_2O), cm^{-1}	Band assignments in H_2O, PED %	Wavenumber H_2O (D_2O), cm^{-1}	Band assignments in H_2O, PED %		Wavenumber H_2O (D_2O), cm^{-1}
647	51 σ_tH−O−H			646 (699)	22 σ_wH−O−H + 43 σ_tH−O−H	633 (605)	10 σ_{sci}O−S−O + 63 σ_tH−O−H		
641 (641)	52 σ_wO−S=O + 12 γO=S−2O			639 (635)	45 σ_wO−S=O + 18 σ_tH−O−H + 10 σ_{sci}O=S=O				
621 (465)	23 σ_wH−O−H + 43 σ_tH−O−H	624 (455)	90 σ_tH−O−H	629 (461)	38 σ_wH−O−H + 22 σ_tH−O−H + 15 γO=S−2O	623 (459)	90 σ_tH−O−H	bound H_2O	608[*]
607 (455, 413)	30 σ_wH−O−H + 35 σ_tH−O−H	611 (438)	72 σ_tH−O−H	609 (449)	12 σ_wH−O−H + 70 σ_tH−O−H	616 (448)	81 σ_tH−O−H		

Calculated								Approximate description	Experimental
SO_4^{2-} ligand is beside the NCS⁻ ligand				SO_4^{2-} ligand is on the opposite of the NCS⁻ ligand					
explicitly solvated		explicitly-implicitly solvated		explicitly solvated		explicitly-implicitly solvated			
Wavenumber H_2O (D_2O), cm⁻¹	Band assignments in H_2O, PED %	Wavenumber H_2O (D_2O), cm⁻¹	Band assignments in H_2O, PED %	Wavenumber H_2O (D_2O), cm⁻¹	Band assignments in H_2O, PED %	Wavenumber H_2O (D_2O), cm⁻¹	Band assignments in H_2O, PED %		Wavenumber H_2O (D_2O), cm⁻¹
		606 (606)	57 σ_{sci}O−S−O + 16 σ_tH−O−H + 14 σ_{sci}O=S=O						
558 (559)	14 νFe−O(SO₄) + 38 γO−S=2O	588	91 σ_tH−O−H	558 (560)	20 ν_{as}S−O + 53 γO−S=2O	596	51 σ_{sci}O−S−O + 14 σ_tH−O−H + 13 σ_{sci}O=S=O		
544	51 σ_wH−O−H	549 (549)	71 γO−S=2O	547 (544)	49 σ_wH−O−H + 25 γO=S−2O	552 (553)	71 γO−S=2O		
529 (532)	23 σ_{sci}O=S=O + 44 γO=S−2O	525 (525)	88 γO=S−2O	536	36 σ_wH−O−H + 19 γO=S−2O	525 (532)	79 γO=S−2O		

ANNEX 1. continued

Calculated								Approximate description	Experimental
SO_4^{2-} ligand is beside the NCS^- ligand				SO_4^{2-} ligand is on the opposite of the NCS^- ligand					
explicitly solvated		explicitly-implicitly solvated		explicitly solvated		explicitly-implicitly solvated			
Wavenumber H_2O (D_2O), cm^{-1}	Band assignments in H_2O, PED %	Wavenumber H_2O (D_2O), cm^{-1}	Band assignments in H_2O, PED %	Wavenumber H_2O (D_2O), cm^{-1}	Band assignments in H_2O, PED %	Wavenumber H_2O (D_2O), cm^{-1}	Band assignments in H_2O, PED %		Wavenumber H_2O (D_2O), cm^{-1}
509	53 σ_wH−O−H + 10 σ_{sci}O=S=O			503 (512)	18 νFe−O(SO$_4$) + 11 σ_{sci}O−S=O + 32 σ_{sci}O=S=O + 12 γO=S−2O				
507 (514)	10 σ_tH−O−H + 23 σ_{sci}O=S=O	484 (484)	18 νFe−O + 15 σ_{sci}O−S−O + 61 σ_{sci}O=S=O	498 (418)	11 σ_{sci}O=S=O + 51 σ_wH−O−H	481 (483)	16 νFe−O(SO$_4$) + 16 σ_{sci}O−S−O + 59 σ_{sci}O=S=O		
478 (486)	90 σN=C=S	470 (472)	93 σN=C=S	487 (493)	85 σN=C=S	474 (476)	92 σN=C=S	NCS	422[*]
475 (482)	88 σN=C=S	468 (470)	89 σN=C=S	482 (486)	85 σN=C=S	470 (467)	96 σN=C=S	NCS	
444 (385, 332)	33 σ_wH−O−H + 33 σ_tH−O−H	449 (349)	84 σ_wH−O−H	420 (391)	75 σ_tH−O−H + 12 σ_{sci}O−S=O	454 (348)	83 σ_wH−O−H	bound H_2O	

Calculated								Approximate description	Experimental
SO_4^{2-} ligand is beside the NCS^- ligand				SO_4^{2-} ligand is on the opposite of the NCS^- ligand					
explicitly solvated		explicitly-implicitly solvated		explicitly solvated		explicitly-implicitly solvated			
Wavenumber H_2O (D_2O), cm^{-1}	Band assignments in H_2O, PED %	Wavenumber H_2O (D_2O), cm^{-1}	Band assignments in H_2O, PED %	Wavenumber H_2O (D_2O), cm^{-1}	Band assignments in H_2O, PED %	Wavenumber H_2O (D_2O), cm^{-1}	Band assignments in H_2O, PED %		Wavenumber H_2O (D_2O), cm^{-1}
		397 (298)	82 σ_w(H−O−H)						
						405 (307)	71 σ_wH−O−H		
374 (372)	71 σ_{sci}O=S−O	362 (361)	90 σ_{sci}O=S−O	372 (372)	64 σ_{sci}O−S=O	362 (365)	88 σ_{sci}O=S−O	bound SO_4^{2-}	
366 (356)	35 νFe−N + 23 σ_{sci}S−O−Fe	352 (337)	58 ν_sFe−O(H_2O) + 12 σ_wH−O−H	371 (362)	40 νFe−N + 13 σ_{sci}S−OFe	334 (324)	10 νFe−N + 71 ν_sFe−O(H_2O)		
325	60 νFe−O(H_2O) + 10 σS−O−Fe	325	31 ν_sFe−O(H_2O) + 46 σ_wH−O−H	320 (315)	57 νFe−O(H_2O) + 13 γO−S=2O	323 (317)	79 ν_{as}Fe−O(H_2O)		
307 (303)	20 νFe−O(SO_4) + 29 νFe−O(H_2O) + 14 γO−S=2O	320 (316)	23 νFe−N + 38 νFe−O(H_2O)	310 (300)	89 ν_{as}Fe−O(H_2O)	306 (300)	25 νFe−N + 18 νFe−O(H_2O) + 16 σ_{sci}S−O−Fe		

ANNEX 1. continued

Calculated								Approximate description	Experimental
SO_4^{2-} ligand is beside the NCS⁻ ligand				SO_4^{2-} ligand is on the opposite of the NCS⁻ ligand					
explicitly solvated		explicitly-implicitly solvated		explicitly solvated		explicitly-implicitly solvated			
Wavenumber H_2O (D_2O), cm⁻¹	Band assignments in H_2O, PED %	Wavenumber H_2O (D_2O), cm⁻¹	Band assignments in H_2O, PED %	Wavenumber H_2O (D_2O), cm⁻¹	Band assignments in H_2O, PED %	Wavenumber H_2O (D_2O), cm⁻¹	Band assignments in H_2O, PED %		Wavenumber H_2O (D_2O), cm⁻¹
289 (315)	10 νFe−N + 41 ν_sFe−O(H_2O) + 20 σS−O−Fe	298 (291)	64 ν_{as}Fe−O(H_2O) + 10 σ_{sci}S−O−Fe	289 (278)	11 νFe−N + 10 νFe−O(SO$_4$) + 51 ν_sFe−O(H_2O)	285 (277)	78 νFe−O(H_2O)		
281	46 σ_tH−O−H	276(272)	29 νFe−N + 27 νFe−O(SO$_4$)						
258	62 σ_tH−O−H	241(248)	21 σ_tH−O−H	250(241)	16 νFe−O(SO$_4$) + 49 ν_{as}Fe−O(H_2O)				
240 (239)	18 νFe−O(SO$_4$) + 44 νFe−O(H_2O) + 10 γO−S=2O			246	12 σ(SO$_4$) O−Fe−O(H_2O) + 54 σ_tH−O−H	236 (232)	11 νFe−N + 33 νFeO(SO$_4$)		

Calculated								Approximate description	Experimental
SO_4^{2-} ligand is beside the NCS^- ligand				SO_4^{2-} ligand is on the opposite of the NCS^- ligand					
explicitly solvated		explicitly-implicitly solvated		explicitly solvated		explicitly-implicitly solvated			
Wavenumber H_2O (D_2O), cm^{-1}	Band assignments in H_2O, PED %	Wavenumber H_2O (D_2O), cm^{-1}	Band assignments in H_2O, PED %	Wavenumber H_2O (D_2O), cm^{-1}	Band assignments in H_2O, PED %	Wavenumber H_2O (D_2O), cm^{-1}	Band assignments in H_2O, PED %		Wavenumber H_2O (D_2O), cm^{-1}
233 (230)	46 ν_{as}Fe−O(H_2O) + 21 σ_{sci}(SO$_4$)O−Fe−O(H_2O)	238	11 νFe−N + 39 ν_{as}Fe−O(H_2O)	230	10 σ(SO$_4$)O−Fe−O(H_2O) + 35 σS−O−Fe + 16 νFe−O(SO$_4$)				
223 (222)	13 νFe−O(H_2O) + 41 σ_tH−O−H	226	42 σ_{sci}S−O−Fe + 10 σ_tH−O−H	224	10 σS−O−Fe + 42 σ(SO$_4$)O−Fe−O(H_2O)	211	20 τH−O−Fe−O(H_2O)		
		201	23 γN−Fe−2O(SO$_4$) + 31 σ_tH−O−H			202 (201)	12 νFe−N + 38 σ_{sci}S−O−Fe + 11 τH−O−Fe−O(H_2O)		

[*]assignment according to Raman spectra subtraction procedure

ANNEX 2. Calculated and experimental vibrational assignments of $[Fe(NCS)]^{2+}$ complex in the different hypothetical cases by PBE1PBE method. Theoretical assignments are based on detailed PED analysis. Abbreviations: ν – stretching; ν_{as} – asymmetric stretching; ν_s – symmetric stretching; σ – deformation; σ_{sci} – scissoring deformation; σ_t – twisting deformation; σ_w – wagging deformation; γ – out-of-plane deformation

Calculated								Approximate description	Experimental
SO_4^{2-} ligand is beside the NCS^- ligand				SO_4^{2-} ligand is on the opposite of the NCS^- ligand					
explicitly solvated		explicitly-implicitly solvated		explicitly solvated		explicitly-implicitly solvated			
Wavenumber H_2O (D_2O), cm^{-1}	Band assignments in H_2O, PED %	Wavenumber H_2O (D_2O), cm^{-1}	Band assignments in H_2O, PED %	Wavenumber H_2O (D_2O), cm^{-1}	Band assignments in H_2O, PED %	Wavenumber H_2O (D_2O), cm^{-1}	Band assignments in H_2O, PED %		Wavenumber H_2O (D_2O), cm^{-1}
3941 (2891)	100 ν_{as}O−H	3608 (2646)	99 νO−H	3930 (2880)	99 ν_{as}O−H	3606 (2646)	98 ν_{as}O−H	bound H_2O	
3910 (2863)	100 νO−H	3607 (2646)	100 νO−H	3926 (2876)	99 ν_{as}O−H	3600 (2641)	98 ν_{as}O−H	bound H_2O	
3910 (2847)	94 ν_sO−H	3604 (2642)	99 ν_{as}O−H	3899 (2839)	100 νO−H	3592 (2634)	100 ν_{as}O−H	bound H_2O	
3817 (2751)	100 ν_sO−H	3549 (2560)	100 ν_sO−H	3799 (2739)	99 ν_sO−H	3545 (2556)	75 ν_sO−H	bound H_2O	
3769 (2720)	100 ν_sO−H	3540 (2551)	94 νO−H	3789 (2732)	99 ν_sO−H	3535 (2548)	91 νO−H	bound H_2O	
3116 (2273)	99 νO−H	3539 (2551)	96 νO−H	3193 (2326)	98 νO−H	3530 (2544)	92 ν_sO−H	bound H_2O	
2109 (2109)	87 νN=C + 11 νC=S	2100 (2100)	91 νN=C	2101 (2101)	87 νN=C + 12 νC=S	2095 (2095)	91 νN=C	NCS	2067 (2061)
1660 (1208)	71 σ_{sci}H−O−H	1556 (1141)	77 σ_{sci}H−O−H	1666 (1213)	88 σ_{sci}H−O−H	1558 (1141)	87 σ_{sci}H−O−H	bound H_2O	
1632 (1193)	88 σ_{sci}H−O−H	1554 (1140)	93 σ_{sci}H−O−H	1632 (1196)	81 σ_{sci}H−O−H	1552 (1138)	88 σ_{sci}H−O−H	bound H_2O	
1605 (1178)	90 σ_{sci}H−O−H	1549 (1139)	92 σ_{sci}H−O−H	1619 (1187)	88 σ_{sci}H−O−H	1551 (1135)	89 σ_{sci}H−O−H	bound H_2O	
1350 (1349)	94 ν_{as}S=O	1234 (1234)	99 ν_{as}S=O	1338 (1337)	93 ν_{as}S=O	1236 (1236)	98 ν_{as}S=O	bound SO_4^{2-}	1139 (1139)

Calculated								Approximate description	Experimental
SO_4^{2-} ligand is beside the NCS^- ligand				SO_4^{2-} ligand is on the opposite of the NCS^- ligand					
explicitly solvated		explicitly-implicitly solvated		explicitly solvated		explicitly-implicitly solvated			
Wavenumber H_2O (D_2O), cm^{-1}	Band assignments in H_2O, PED %	Wavenumber H_2O (D_2O), cm^{-1}	Band assignments in H_2O, PED %	Wavenumber H_2O (D_2O), cm^{-1}	Band assignments in H_2O, PED %	Wavenumber H_2O (D_2O), cm^{-1}	Band assignments in H_2O, PED %		Wavenumber H_2O (D_2O), cm^{-1}
1123 (1118)	84 ν_sS=O	1138 (1134)	89 ν_sS=O	1133 (1128)	83 ν_sS=O	1140 (1144)	87 ν_sS=O	bound SO_4^{2-}	1039[*] (1039[*])
1015 (774)	76 σ_tH−O−H			994 (731)	86 σ_tH−O−H				
975 (975)	74 νC=S + 19 νFe−N	923 (923)	78 νC=S + 16 νFe−N	978 (979)	68 νC=S + 17 νFe−N	927 (926)	41 νC=S + 40 νS−O	NCS	750 (750)
878 (877)	74 νS−O	910 (910)	83 νS−O	894 (893)	76 νS−O	920 (920)	39 νC=S + 44 νS−O	bound SO_4^{2-}	
857 (855)	68 νS−O	875 (874)	80 νS−O	857 (853)	80 νS−O	876 (875)	88 νS−O	bound SO_4^{2-}	
663	12 σ_wO−S=O + 41 σ_tH−O−H	639 (476)	77 σ_tH−O−H	668 (475)	31 σ_wH−O−H + 30 σ_tH−O−H	651 (482)	14 σ_wO−S−O + 72 σ_tH−O−H		
658 (658)	47 σ_wO−S=O + 11 γO=S−2O	633 (473)	81 σ_tH−O−H	657 (653)	42 σ_wO−S=O + 20 σ_tH−O−H	638 (468)	88 σ_tH−O−H	bound H_2O	608[*]
640 (468)	40 σ_wH−O−H + 34 σ_tH−O−H	626 (470)	28 σ_{sci}O−S−O + 52 σ_tH−O−H	650 (475)	49 σ_wH−O−H + 18 γO=S−2O	629 (458)	79 σ_tH−O−H		

ANNEX 2. continued

Calculated								Approximate description	Experimental
SO_4^{2-} ligand is beside the NCS⁻ ligand				SO_4^{2-} ligand is on the opposite of the NCS⁻ ligand					
explicitly solvated		explicitly-implicitly solvated		explicitly solvated		explicitly-implicitly solvated			
Wavenumber H₂O (D₂O), cm⁻¹	Band assignments in H₂O, PED %	Wavenumber H₂O (D₂O), cm⁻¹	Band assignments in H₂O, PED %	Wavenumber H₂O (D₂O), cm⁻¹	Band assignments in H₂O, PED %	Wavenumber H₂O (D₂O), cm⁻¹	Band assignments in H₂O, PED %		Wavenumber H₂O (D₂O), cm⁻¹
629 (427)	14 σ_wH−O−H + 64 σ_tH−O−H	618 (460)	32 σ_{sci}O−S−O + 49 σ_tH−O−H	626 (462)	72 σ_tH−O−H	614 (625)	48 σ_wO−S−O + 19 σ_tH−O−H + 10 σ_{sci}O=S=O		
578 (580)	16 νFe−O(SO$_4$) + 41 γO−S=2O	568 (568)	72 γO−S=2O	578 (580)	56 γO−S=2O	571 (571)	16 νFe−O(SO$_4$) + 69 γO−S=2O		
562	52 σ_wH−O−H			562 (430)	44 σ_wH−O−H + 26 γO=S−2O				
545 (548)	25 σ_{sci}O=S=O + 42 γO=S−2O	538 (539)	82 γO=S−2O	552 (405)	41 σ_wH−O−H + 14 γO=S−2O	539 (546)	79 γO=S−2O		

Calculated								Approximate description	Experimental
SO_4^{2-} ligand is beside the NCS^- ligand				SO_4^{2-} ligand is on the opposite of the NCS^- ligand					
explicitly solvated		explicitly-implicitly solvated		explicitly solvated		explicitly-implicitly solvated			
Wavenumber H_2O (D_2O), cm^{-1}	Band assignments in H_2O, PED %	Wavenumber H_2O (D_2O), cm^{-1}	Band assignments in H_2O, PED %	Wavenumber H_2O (D_2O), cm^{-1}	Band assignments in H_2O, PED %	Wavenumber H_2O (D_2O), cm^{-1}	Band assignments in H_2O, PED %		Wavenumber H_2O (D_2O), cm^{-1}
521 (529)	17 σ_{sci}O–S=O + 33 σ_{sci}O=S=O + 11 σ_{sci}S–O–Fe 15 γO=S–2O			517	15 νFe–O(SO$_4$) + 12 σ_{sci}O–S=O + 25 σ_{sci}O=S=O + 16 γO=S–2O				
520 (396)	44 σ_wH–O–H + 28 σ_tH–O–H	498 (499)	16 νFe–O(SO$_4$) + 14 σ_tO–S–O + 62 σ_{sci}O=S=O	515 (316)	49 σ_wH–O–H + 19 σ_{sci}O=S=O	496 (499)	15 σ_tO–S=O + 11 σ_{sci}S–O–Fe + 61 σ_{sci}O=S=O		
486 (495)	100 σN=C=S	475 (480)	91 σN=C=S	494 (497)	85 σN=C=S	479 (482)	95 σN=C=S	NCS	422[*]
483 (490)	93 σN=C=S	474 (473)	91 σN=C=S	489 (491)	90 σN=C=S	475 (474)	95 σN=C=S	NCS	

ANNEX 2. continued

	Calculated								Approximate description	Experimental
	SO_4^{2-} ligand is beside the NCS^- ligand				SO_4^{2-} ligand is on the opposite of the NCS^- ligand					
	explicitly solvated		explicitly-implicitly solvated		explicitly solvated		explicitly-implicitly solvated			
	Wavenumber H_2O (D_2O), cm^{-1}	Band assignments in H_2O, PED %	Wavenumber H_2O (D_2O), cm^{-1}	Band assignments in H_2O, PED %	Wavenumber H_2O (D_2O), cm^{-1}	Band assignments in H_2O, PED %	Wavenumber H_2O (D_2O), cm^{-1}	Band assignments in H_2O, PED %		Wavenumber H_2O (D_2O), cm^{-1}
	463 (345)	31 σ_wH−O−H + 35 σ_tH−O−H	457 (356)	79 σ_wH−O−H	439 (462)	76 σ_tH−O−H + 11 σ_{sci}O−S=O	462 (355)	77 σ_wH−O−H	bound H_2O	
			451 (351)	83 σ_wH−O−H			447 (350)	81 σ_wH−O−H		
			409 (309)	85 σ_wH−O−H			420 (318)	81 σ_wH−O−H		
	387 (385)	71 σ_{sci}O=S−O	368 (368)	90 σ_{sci}O=S−O	385 (385)	68 σ_{sci}O−S=O	374 (377)	89 σ_{sci}O−S=O	bound SO_4^{2-}	
	375 (365)	33 νFe−N + 24 σ_{sci}S−O−Fe	357 (345)	84 ν_sFe−O(H$_2$O)	381	42 νFe−N + 12 νFe−O(SO$_4$) + 10 σ_{sci}S−O−Fe + 11 σ_{sci}O=S=O	350 (338)	76 ν_sFe−O(H$_2$O)		

Calculated								Approximate description	Experimental
SO_4^{2-} ligand is beside the NCS^- ligand				SO_4^{2-} ligand is on the opposite of the NCS^- ligand					
explicitly solvated		explicitly-implicitly solvated		explicitly solvated		explicitly-implicitly solvated			
Wavenumber H_2O (D_2O), cm^{-1}	Band assignments in H_2O, PED %	Wavenumber H_2O (D_2O), cm^{-1}	Band assignments in H_2O, PED %	Wavenumber H_2O (D_2O), cm^{-1}	Band assignments in H_2O, PED %	Wavenumber H_2O (D_2O), cm^{-1}	Band assignments in H_2O, PED %		Wavenumber H_2O (D_2O), cm^{-1}
320 (316)	17 νFe−O(SO$_4$) + 43 νFe−O(H$_2$O) + 13 γO−S=2O)	316	74 σ_{as}Fe−O(H$_2$O) + 10 σ_{sci}S−O−Fe	329	74 ν_{as}Fe−O(H$_2$O)	314	27 νFe−N + 31 σ_{sci}S−O−Fe + 11 σ_{sci}O=S=O		
301 (291)	14 νFe−N + 27 ν_sFe−O(H$_2$O) + 21 σ_{sci}S−O−Fe	281 (277)	27 νFe−N + 34 νFe−O(SO$_4$)	302	58 ν_sFe−O(H$_2$O)	300	80 νFe−O(H$_2$O)		
288	52 σ_tH−O−H	253	60 σ_tH−O−H	264 (255)	17 νFe−O(SO$_4$) + 56 νFe−O(H$_2$O)	250	53 νFe−O(SO$_4$)		
259	67 σ_tH−O−H	246 (234)	23 νFe−N + 13 νFe−O(SO$_4$) + 36 ν_{as}Fe−O(H$_2$O)	251	19 σ_{sci}(SO$_4$)O−Fe−O(H$_2$O) + 45 σ_tH−O−H	208	12 νFe−N + 15 σ_{sci}S−O−Fe + 32 σ_tH−O−H		

ANNEX 2. continued

Calculated								Approximate description	Experimental
SO_4^{2-} ligand is beside the NCS^- ligand				SO_4^{2-} ligand is on the opposite of the NCS^- ligand					
explicitly solvated		explicitly-implicitly solvated		explicitly solvated		explicitly-implicitly solvated			
Wavenumber H_2O (D_2O), cm^{-1}	Band assignments in H_2O, PED %	Wavenumber H_2O (D_2O), cm^{-1}	Band assignments in H_2O, PED %	Wavenumber H_2O (D_2O), cm^{-1}	Band assignments in H_2O, PED %	Wavenumber H_2O (D_2O), cm^{-1}	Band assignments in H_2O, PED %		Wavenumber H_2O (D_2O), cm^{-1}
253 (250)	16 νFe−O(SO$_4$) + 56 ν_{as}Fe−O(H$_2$O)	241	55 σ_{sci}S−O−Fe	243	16 νFe−O(SO$_4$) + 38 σ_{sci}S−O−Fe	203 (203)	18 νFe−N + 24 σ_{sci}S−O−Fe		
245	17 νFe−O(SO$_4$) + 27 νFe−O(H$_2$O) + 14 σ_{sci}H−O−H			231	40 σ_{sci}(SO$_4$)O−Fe−O(H$_2$O) + 11 νFe−N				
229	50 σ_tH−O−H								

*assignment according to Raman spectra subtraction procedure